

University of Nottingham
UK | CHINA | MALAYSIA

Coupling Bionic Model Design and Parameter Optimization of Grey Cast Iron Truck Drum Brake

Dahui Yu

Thesis submitted to University of Nottingham for the degree of Doctor of Philosophy

April 2023

Acknowledgement

First of all, I would like to show my all respect to my supervisor, Prof. Yuying Yan. I would like to appreciate his support and kind help for my PhD study during last four years. Without his comments and help, this thesis would not be finished. Prof. Yuying Yan is such a good supervisor, a great teacher, and an unbelievable mentor who has had a huge impact on my life. I believe that last four years of learning with Prof. Yan is just the beginning. Professor's attitude towards life is worth continuing and always looking up to.

Next, I would like to appreciate to Dr. Mark Alston, thank you for your advice and support in Annual Review. Appreciate to Dr. Wei Gong, Dr. Yiyi Chen, Dr. Kuo Huang, Dr. Xin Wang, and Dr. Shuai Zhang, I will never forget your kindly help and encouragement always. Besides, thanks to my colleagues and technicians in Fluids and Thermal Engineering Research Group.

Last but not least, my dear family Kemin Yu, Barbara Yang, Tony Qin, Xuebai Cao, Sylvia Qin, and my beloved wife Baoxin Du, my boy Barry Yu, I cannot imagine if I can do this without your support and love.

Farewell to this wonderful journey on campus but being a student forever.

Abstract

With the growth of road transport scale, transport vehicles have more load, faster speed, increasing transport efficiency, overcoming harsh road environments and other changing trends, the safety of life and property face unprecedented challenges. The brake system is the security of transport vehicles, in which the drum brake is an important part of the truck braking system, in the truck braking by thermal fatigue and wear role to produce thermal fatigue cracks, resulting in drum brake failure, serious life-threatening, drum brakes and the material used in grey cast iron problems are increasingly prominent. Therefore, to improve the service life of the drum brake, improving the drum brake's grey cast iron material resistance to thermal fatigue and wear performance has practical significance and significant application value.

The failure of grey cast iron truck drum brakes is a complex problem caused by multiple factors that cannot be solved by changing a single factor alone. Observations and studies of the surface characteristics of living organisms in nature have revealed that in order to adapt to nature, organisms have evolved a body surface structure with excellent functionality due to the combined effect of multiple coupled factors such as structure, material and morphology. In this paper, based on the principle of coupling bionics, the coupling bionic unit is prepared on the surface of grey cast iron by laser fusion, and the unit coupling element forms a "soft-hard" structure with the base material coupling element, the relationship between laser energy and drum brake wall

thickness is investigated, the laser parameters for processing grey cast iron truck drum brakes are optimized, and the effect of different tissue grey cast iron base material coupling elements on the drum brake is analyzed. The influence of the coupling elements of different grey cast iron base materials on the laser coupling bionic treatment was analyzed, the degree of improvement of the coupling bionic units on the thermal fatigue and wear performance of grey cast iron with different structures was summarized, the influence of the morphological coupling element characteristics on the thermal fatigue and wear performance of grey cast iron drum brakes was investigated, a combined coupling bionic model for the failure characteristics of grey cast iron truck drum brakes was designed, and a number of coupling bionic grey cast iron drum brakes were trialled for bench testing.

Keywords:

Drum brakes, grey cast iron, laser, coupling bionic, thermal fatigue and wear resistance

List of Publications during PhD Study

1. D.H. Yu, Y.Y. Yan, Effects of angle formation between melted zone and friction direction on thermal fatigue and wear resistance of truck drum brake, Proceedings of the Institution of Mechanical Engineers Part D-Journal of Automobile Engineering, 235 (2021) 1297-1307.
2. D.H. Yu, Y.Y. Yan, Effects of Pearlite on Thermal Fatigue and Wear Resistance of Gray Cast Iron Treated by Laser, Journal of Materials Engineering and Performance, 31 (2022) 3962-3974.
3. D. Yu, Y. Yan, Effects of bionic models with simultaneous thermal fatigue and wear resistance, Advances in Heat Transfer and Thermal Engineering: Proceedings of 16th UK Heat Transfer Conference (UKHTC2019), Springer, 2021, pp. 903-907.

Table of Contents

Acknowledgement I

Abstract II

List of Publications during PhD Study IV

Chapter 1: Introduction 1

1.1 Aims and objectives of my PhD research 1

1.2 Research status of grey cast iron drum brake 4

1.2.1 Research status of the drum brake 4

1.2.2 Research status of thermal fatigue of grey cast iron for drum brake 8

1.3 The theory of coupling bionic fatigue and wear resistance and the applications 18

1.3.1 Coupling bionics 18

1.3.2 Coupling bionic of fatigue and wear resistance 19

1.3.3 The applications of coupling bionic fatigue and wear resistance 20

1.4 The bionic prototype of fatigue and wear resistance 26

1.4.1 Shell nacreous layers 27

1.4.2 Plant leaves 28

1.4.3 Dragonfly wings 29

1.5 Laser coupling bionic processing technology 30

1.6 The main purpose and significance of the thesis 35

Chapter 2: Experimental Study 38

2.1 Experimental materials 38

2.2 Preparation of samples 40

2.3 Microanalysis and performance testing 43

2.3.1 Observation of microstructure 43

2.3.2 SEM and EDS 44

2.3.3 Microhardness 44

2.3.4 Phase analysis 44

2.3.5 Thermal fatigue test 45

2.3.6 Wear test 47

2.3.7 Bench test 48

2.3.9 Ansys finite element analysis 50

Chapter 3: Parameter Optimization of Structural Coupling Element Unit of Grey Cast Iron Truck Drum Brake 52

3.1 Introduction 52

3.2 The relationship between laser energy and sample thickness 54

3.2.1 Results of different thickness samples processed by the same laser energy 54

3.2.2 Temperature field simulation of samples with different thickness processed by the same laser energy 57

3.2.3 Transfer law of laser energy in samples with different thickness 65

3.3 Parameter optimization of structural coupling unit of grey cast truck drum brake prepared by laser 67

3.3.1 Design and result analysis of orthogonal test 68

3.3.2 Relationship between laser processing energy and sample thickness .. 71

3.4 Laser fabrication of structural coupling units 72

3.5 Chapter summary 75

Chapter 4: Influence and Analysis of Base Metal Coupling Element on Thermal Fatigue and Wear Resistance of Bionic Grey Cast Iron Truck Drum Brake 78

4.1 Introduction 78

4.2 Influence and analysis of graphite type on thermal fatigue and wear resistance of coupling bionic samples 79

4.2.1 Different graphite types of grey cast iron 80

4.2.2 Microstructure analysis of different graphite samples 81

4.2.3 Effects of graphite type on microthermal fatigue crack 83

4.2.4 Influence of graphite type on macroscopic thermal fatigue crack 88

4.2.5 Effect of graphite type on wear property 94

4.3 Effects of carbon content on thermal fatigue and wear resistance of coupling bionic samples 97

4.3.1 Base metal structure with different carbon content 98

4.3.2 Analysis of microstructure of sample units with different carbon content 100

4.3.3 Effect of different carbon content on thermal fatigue resistance 102

4.4 Effects of pearlite content and interlamellar spacing on thermal fatigue and wear resistance of coupling bionic samples 116

4.4.1 Base metal structure with different pearlite content and interlamellar spacing 117

4.4.2 Effect and analysis of different pearlite content on thermal fatigue

resistance of samples 123

4.4.3 Influence and analysis of different pearlite interlamellar spacing on thermal fatigue resistance of samples 126

4.4.4 Effect of different pearlite content and interlamellar spacing on wear performance 129

4.5 Chapter summary 131

Chapter 5: Influence of Morphological Coupling Characteristic Quantity on Thermal Fatigue and Wear Resistance of Grey Cast Iron Truck Drum Brake and Design of Coupling Bionic Model 135

5.1 Introduction 135

5.2 The Influence and Analysis of Morphological Coupling Characteristic Quantity on Thermal Fatigue and Wear Resistance of Samples 136

5.2.1 Influence and analysis of morphological coupling element distribution spacing characteristic quantity 137

5.2.2 The influence and analysis of morphological coupling element distribution angle characteristic quantity 149

5.3 Double Combination Coupling Bionic Model Design 157

5.3.1 Influence and analysis of characteristic quantities with different distribution spacing 158

5.3.2 The influence and analysis of characteristic quantities with different distribution angles 165

5.4 Chapter Summary 171

Chapter 6 Study on Bench Test 174

6.1 Introduction 174

6.2 Trial Manufacture of Bionic Drum Brake 174

6.3 Drum Brake Bench Test Results and Analysis 176

6.4 Trial-manufacture and test of multi-combination coupling bionic drum brake 181

6.5 Chapter summary 185

Chapter 7 Conclusion 187

7.1 Summary and Conclusions 187

7.2 Suggestions for future work 191

Reference 193

Chapter 1: Introduction

1.1 Aims and objectives of my PhD research

Since the rapid development of the world economy, the development of highway transportation has laid the foundation of economic development[1, 2]. Vehicle braking system plays an important role in highway transportation[3, 4]. With the development of heavy vehicles in highway transportation towards the heavy loads and high speed, the quality and performance of vehicle brakes are more and more demanding. With reliable performance, large braking torque and simple structure, the drum brake is commonly used in large and medium-sized passenger cars and trucks. When the vehicle is running, the drum brake rotates with the wheel[5]. During braking, the brake wheel cylinder pushes the brake shoe to squeeze the inner surface of the drum brake. The powerful friction force produces a torque to prevent the wheel from rotating to achieve the effect of braking[6-8]. In the braking process, due to the huge load and friction effect, the temperature of the inner surface of the drum brake rises sharply, emergency braking and other extreme conditions of the highest temperature up to 800~900℃, as the wheel continues to rotate in the air cooling and metal itself under good thermal conductivity, the temperature rapidly decreases, so alternating hot and cold action, high load, strong friction service state, thermal fatigue cracks occur on the inner surface of the drum brake[9-11], when the thermal fatigue crack expands to a certain extent, the drum brake breaks and fails[12]. When the thermal fatigue

crack appears, it will not only affect the braking performance of the drum brake but also cause hidden danger to the safety of life and property[13, 14]. The main mode of transportation in mountainous areas still relies on road transportation. When running in mountainous areas and other areas with complex environments, frequent braking and improper cooling of the drum brake with cold water accelerate the failure of the drum brake. Therefore, how to improve the thermal fatigue and wear resistance of the drum brake and improve the service life of the drum brake is a practical problem to be solved urgently.

In 2016, there were more than 4000 fatalities in crashes caused by heavy trucks in the USA which was the highest since 2007, and heavy truck fatalities increased in that year by more than 8% compared to 2015, which was higher than the overall increase of 5.6% in the fatalities. The FACT (Fatal accident Complaint Team) indicated that brake problems caused more than 32% of truck accidents[15-17]. In addition, the sales volume of China's medium and heavy trucks will be about 1.4 million in 2021[18]. As a wearing part, drum brakes need to be replaced in time, and the annual consumption is expected to reach more than 35 million. Meanwhile, the material waste caused by drum brake failure is worth billions of pounds, and the extra maintenance and labour costs are countless. In addition, most drum brakes on the market at present the price of 20~50 pounds per piece, while the price of imported drum brakes is 80 to hundreds of pounds, the main reason is that the Chinese drum brakes grey cast iron material thermal fatigue and wear performance is poor, short service life, lack of market competitiveness; On the other hand, drum brakes are

labor-intensive products. For example, the production cost in Europe is higher than that in China. To sum up, the research on improving the service life of drum brakes not only concerns the safety of life and property but also can bring significant economic benefits.

Based on the coupling bionic theory, inspired by the fatigue resistance and wear resistance of natural biological surface structures, similar bionic structures are manufactured on the surface of materials, which have been proved to improve their performance and increase the service life of materials. However, the current research in this field remains at the stage of influencing the fatigue and wear resistance of grey cast iron materials, while the special service environment of drum brakes leads to their special non-uniform regional failure characteristics, as shown in Fig.1.1. At present, the research results of laser coupling bionic processing in the laboratory cannot be directly applied to the drum brake, nor can it reflect the characteristics of biological adaptation in the coupling bionic thought, so it cannot give play to the advantages of laser coupling bionic processing technology[19]. The purpose of this study is to improve the service life of grey cast iron truck drum brakes to transplant the laser coupling bionic processing technology from the laboratory sample to the actual production of truck drum brakes, from the theoretical basis to the practical application. By exploring the relationship between laser processing parameters and samples with different wall thicknesses, the most suitable laser parameters for processing drum brakes are found. By studying the effects of different graphite types, different carbon content, different pearlite quantity and sheet spacing on the thermal

fatigue and wear resistance of coupling bionic grey cast iron, the influence rule of base metal coupling element on the bionic surface was obtained, which provided data support and reference for industrial production. According to the failure characteristics of grey cast iron drum brake in actual working conditions, a combined coupling bionic model is designed to improve the thermal fatigue and wear resistance of the drum brake and prolong its service life. This study provides experimental basis and theoretical basis for the practical application of laser coupling bionic processing technology, and is of great significance for the future design and production of the bionic drum brake, and for the promotion of drum brake manufacturing industry.

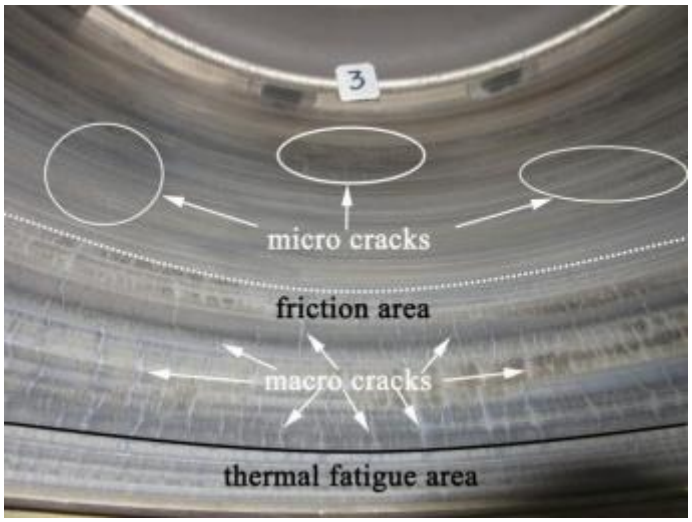


Fig.1.1 Schematic diagram of regional failure characteristics of drum brake

1.2 Research status of grey cast iron drum brake

1.2.1 Research status of the drum brake

For a long time, the main material of drum brakes is grey cast iron, which has good casting performance, high hardness, excellent shock absorption wear resistance, and material preparation cost is low[20, 21]. Early use of 150 grey cast iron, although the

thermal conductivity is good, the strength and hardness are low, cracking and wear is very serious, cannot resist the wear process of intense friction, the common drum brake grey cast iron is mainly 200 and 250, the service life has increased, but the thermal fatigue and wear situation is still serious. In recent years, the improvement of thermal fatigue resistance and wear resistance of drum brake mainly focuses on the research of materials, which is mainly reflected in the following aspects:

(1) The service time of the drum brake can be improved by modifying and strengthening the existing materials of the drum brake. For example, the pretreatment process can improve the nucleation condition of graphite precipitation in grey cast iron, reduce the fluctuation range of mechanical properties parameters effectively, and control the primary austenite to strengthen grey cast iron [22, 23]. Alloying elements such as chromium and copper are added to alloyed cast iron. After alloying, the pearlite volume of cast iron is increased and refined, to improve the hardness and strength of the drum brake and enhance the wear resistance[24]. The composition of grey cast iron used for the drum brake was designed and optimized according to its required properties, and it was found that the main factors affecting the mechanical properties of castings were chemical composition and alloying elements. By adjusting the carbon content and alloying at the same time, grey cast iron base material with higher strength and hardness could be obtained, to improve the service life of the drum brake[25]. In addition, the addition of trace elements can accelerate the formation of pearlite, so grey cast iron can obtain higher hardness and strength. The alloy cast iron of different countries in the world is different, for example, the alloy

cast iron of copper, chromium and tin elements is used in Germany[26]. Selin, Holmgren et al. carried out the alloying design of cast iron and studied the influence of the additional amount of chromium, silicon, copper and other elements on tensile strength and hardness by orthogonal test and obtained alloy cast iron with excellent structure and properties [27]. Wu Lijun et al. found that after the solidification of grey cast iron, the amount of cementite changes, which is determined by the cooling rate and its own chemical composition, resulting in the change of pearlite content at the same time. Silicon, manganese, chromium and other elements will reduce the amount of pearlite, while titanium, vanadium and other elements will increase the content of pearlite [28, 29].

(2) The graphite in grey cast iron is studied to improve the performance of the drum brake. The properties of grey iron can be determined by the different types and points of graphite, such as type A graphite with uniform distribution, type B graphite with chrysanthemum shape, type C graphite precipitated from the liquid iron containing hyper eutectic components, type D supercooled graphite formed in the dendrite gap of primary austenite, and low carbon content and subcooling degree. For the type E supercooled stone ink precipitated between secondary dendrites, different graphite types lead to different properties of grey cast iron, so optimizing the graphite type of grey cast iron is one of the ways to improve the properties of grey cast iron [30-33]. In addition, it has been found that graphite can play a certain role in buffering grey cast iron when it is shaken, which is due to the different densities of graphite and other tissues. When the vibration is transmitted in the medium, graphite can reduce the

vibration energy, so grey cast iron has good shock absorption [34, 35]. The increase of carbon content in grey cast iron leads to the increase of graphite content, and thus the thermal conductivity becomes stronger [36, 37]. Graphite is a soft phase in grey cast iron, and due to its flake or flake shape, it is easy to fall off during dry friction and become a lubricant in the friction process, which can effectively reduce wear loss [38, 39].

(3) Research on the replacement of drum brake materials, that is, grey cast iron is the main material used for drum brakes at present. Try different types of brake materials for other vehicles instead of grey cast iron. At present, the brake disc of high-speed trains is mainly made of vermicular graphite cast iron, which has low manufacturing cost and extremely cost-effective compared with other brake disc materials with stable performance [40]. A new generation of potential brake disc material, aluminium matrix composite material, is formed by adding silicon carbide or alumina particles as reinforcement phase on the basis of aluminium alloy base material, which has the characteristics of lightweight, high strength and hardness, good wear resistance and high thermal conductivity [41, 42].The brake disc made of aluminium matrix composite material also has the following problems. When the brake disc cracks, due to the low plasticity of the material, the crack is easy to expand and extend, thus affecting the service life of the brake disc, and the price is relatively high and the cost performance is low. At present, the application of aluminium matrix composite brake discs is still in its infancy, and there are few studies on there wear resistance. In addition, carbon-carbon fiber composite brake disc can work at a high temperature of

thousands of degrees Celsius, with a low coefficient of thermal expansion and high specific heat performance. Compared with other materials, carbon-carbon fiber composite brake disc has obvious advantages. However, this material is more prone to wear in rainy and snowy weather conditions, and the use risk is increased [43, 44]. Later, in order to improve the performance of this material, the researchers changed the sealing structure of the brake disc and added the cooling system. However, there are still some problems such as matching with adjacent components, the large influence of friction coefficient and high price, which hinder the development of carbon-carbon fiber composite materials in the brake system.

1.2.2 Research status of thermal fatigue of grey cast iron for drum brake

The main reason leading to the failure of grey cast iron drum brake is that under the combined action of thermal fatigue and wear, thermal fatigue cracks start and extend to the top, resulting in drum brake rupture [21, 45-48]. The essence of thermal fatigue is that thermal strain causes thermal stress, and then thermal stress leads to plastic strain fatigue. Wear and tear is a phenomenon of wear and tear caused by mechanical forces or accompanied by chemical reactions. For drum brakes, due to the heavy load and complex road conditions in service, they are subjected to high strength during braking, and a lot of heat will be generated in the friction process [49]. In order to solve the problems of thermal fatigue and wear of grey cast iron, scholars have done a lot of research work.

Firstly, as for thermal fatigue, the first research paper on thermal stress appeared in

1884 [50]. The factors affecting thermal fatigue can be divided into external factors and internal factors, among which the external factors are mainly the thermal cycle temperature and the number of thermal cycles of grey cast iron. Under the condition of other conditions being the same, the higher the temperature difference and the more the number of thermal cycles, the greater the accumulated thermal stress on the material surface, and the easier to produce thermal fatigue cracks; At the same time, surface oxidation and other factors will also affect the initiation and expansion of thermal fatigue. Abdel proposed that thermal fatigue is related to the working environment of materials, for example, oxygen reacts with elements on the surface of materials at high temperature, leading to the reduction of alloying elements and thus the reduction of the strength of materials surface [51-53]. When cracks appear on the surface of the material, oxidation reaction will also occur in the crack in the process of thermal cycling, and the oxide will gradually deposit in the crack, forming additional stress at the tip of the crack to aggravate the expansion of thermal fatigue crack. Therefore, some researchers believe that improving the oxidation resistance of cast iron is to improve the thermal fatigue resistance, but the experimental results of steel and aluminum alloy are contrary. With the progress of thermal cycle, the oxide appearing on the surface will lead to the closure of cracks, but improve its thermal fatigue resistance [54, 55].

Internal factors include the thermal conductivity of grey cast iron, thermal physical properties that change with temperatures, such as elastic modulus and strength, etc. Better thermal conductivity will make the heat of the workpiece more balanced, thus

reducing thermal stress [56, 57]. Low elastic modulus means that the slope of stress-strain curve is low, which is conducive to reducing the change in workpiece size caused by thermal stress, which in turn can reduce the influence on material properties. Generally, in order to improve the thermal fatigue resistance of materials, it is considered that improving the strength and toughness is one of the methods. However, as the toughness of general materials decreases when the strength increases, the strength of materials with good toughness is lower [58-60]. Some scholars have found that the influence of material strength and toughness on thermal fatigue occurs at different stages. Strength plays a major role in the initiation of cracks in thermal fatigue, and toughness mainly affects the propagation of cracks in thermal fatigue. Therefore, a good combination of strength and toughness can ensure that materials have good thermal fatigue resistance [61, 62]. If the strength can be kept high at different temperatures, the cracking of the material under thermal stress can also be reduced. In addition, the thermal fatigue properties of grey cast iron are greatly affected by the structure, among which graphite and pearlite are the main influences. The effect of graphite on the thermal fatigue property of grey cast iron is complicated because it contains both favorable and unfavorable factors. According to relevant studies, graphite in grey cast iron divides the matrix, which is easy to cause stress concentration, and thermal conductivity has a decisive effect on thermal fatigue property. The above factors are all based on thermal conductivity to determine the thermal fatigue property of grey cast iron [63]. Due to the large differences in different properties between graphite and pearlite phases in grey cast iron, graphite

can be regarded as a defect in the base metal [64, 65], belonging to the part with easy stress concentration, which is easy to induce the initiation of thermal fatigue cracks [66, 67]. The grain size in the base metal also has a certain influence on thermal fatigue. According to the Hl-Patch [68, 69] formula, grain refinement in the material leads to an increase in the yield strength of the base metal and an improvement in its toughness. Some Japanese researchers believe that thermal fatigue is caused by the generation of holes and continuous slip zones and the development of substructure. Grain refinement leads to the increase of grain boundaries of base metal, thus preventing the generation of slip and hole alleles, and thus improving the thermal fatigue resistance of materials [70, 71]. Some studies have also shown that the smallest stress concentration caused by graphite is spherical graphite, and it is believed that the fatigue performance of spherical graphite cast iron is better [72, 73]. Some studies have found that the graphite form has a limited influence on the strength of vermicular cast iron at high temperature, and the thermal conductivity has a greater impact on the fatigue property, so the fatigue property of vermicular cast iron is better [74].

The research on the thermal fatigue resistance of grey cast iron mainly focuses on graphite, matrix structure and alloying elements of grey cast iron. The relevant results show that although carbon content has a major impact on the thermal fatigue resistance of grey cast iron, it is complicated. With the increase of carbon content, the thermal fatigue resistance is improved, but when the carbon content reaches the limit value of 3.69%, the thermal fatigue resistance gradually decreases, and the thermal

fatigue crack propagation rate gradually accelerates when the carbon content continues to increase [75, 76]. The main reason is that when the carbon content increases, the thermal conductivity of cast iron is enhanced, the amount and size of graphite are increased at the same time, and the cleavage effect on the base metal is also stronger, which has an impact on the oxidation resistance and elastic modulus and other characteristics of the material, so the thermal fatigue resistance is decreased [77, 78]. Rukadikar defined the morphology of graphite in four different ways: graphite to carbon equivalent ratio, graphite type, graphite size and graphite thickness to length ratio [79], and found that the smaller the ratio of stone to ink to carbon equivalent, the worse the thermal fatigue resistance of grey cast iron, and the larger the graphite thickness to length ratio, the worse the thermal fatigue resistance of grey cast iron. The reason is that the graphite cleavage on the base material reduces the strength of the base material, the graphite tip stress concentration is easy to crack initiation, in addition, the oxidation reaction is easy to occur around the flake graphite, and the oxygen element will penetrate into the matrix along the graphite, so that the thermal fatigue resistance of the material is reduced. The coarse graphite can passivate the thermal fatigue crack and slow down the crack propagation rate to a certain extent [80, 81]. Mohamed et al. found that flake graphite grey iron had the worst thermal fatigue resistance, while ductile iron had the best performance [82]. His views are also shared by Chavez [83], Pan [84] et al. found that the thermal fatigue resistance of cast iron with different graphite forms was different. The strength of vermicular cast iron at high temperature was inferior to that of ductile cast iron, and the thermal

conductivity of vermicular cast iron was inferior to that of flake graphite cast iron, so the performance of vermicular cast iron was the worst.

The thermal fatigue resistance of cast iron varies with different matrix structure, and most studies have proved that pearlite cast iron has good thermal fatigue crack initiation and propagation ability. With high pearlite strength, large stress will cause plastic deformation of materials, and the crack propagation rate is low in the pearlite matrix [85]. Wu [86] found that the degree of refinement of pearlite determines its thermal fatigue resistance, and more refined pearlite has stronger thermal fatigue resistance. However, when the temperature reaches 500 to 600℃, the pearlite structure becomes unstable and decomposing into graphite and ferrite, so it is not suitable for high temperature working environment. Compared with pearlite, ferritic can maintain stability at the highest temperature of 700℃, at the same time has good oxidation resistance and toughness, the disadvantage is low strength, so the thermal fatigue resistance of pearlite cast iron is generally stronger than that of ferritic cast iron. Sui et al. [40] studied the thermal fatigue resistance of vermicular cast iron matrix and found that when the upper limit of thermal cycling temperature exceeds the transition temperature of perlite structure, the thermal fatigue resistance of vermicular cast iron gradually decreases with the increase of perlite volume. When the cycling temperature is below the transition temperature, the perlite structure is relatively stable. It can effectively prevent the initiation and propagation of thermal fatigue cracks, and the thermal fatigue resistance of vermicular cast iron increases with the increase of pearlite volume. Jakubus et al. [87] found that carbide is a bridge

and channel for thermal fatigue crack propagation on the surface of white cast iron, and the more carbide, the worse the thermal fatigue resistance of cast iron is. The fracture type observed for thermal fatigue is cleavage fracture.

Alloying elements play a role in improving the thermal fatigue resistance of cast iron, enhancing the matrix microstructure properties [88, 89], promoting the increase of pearlite volume, the reduction of the spacing of pearlite sheets, and the acceleration of graphitization. In addition, they have an impact on the oxidation resistance and thermal conductivity of materials. The results show that chromium and molybdenum have the greatest influence on thermal fatigue. Chromium can make the matrix structure more stable by increasing the transformation temperature of cast iron, which can reduce the stress and strain during the transformation process. In addition, chromium can also improve the oxidation resistance of the material by forming a dense oxide film on the surface of the material. It can effectively reduce the possibility of thermal fatigue crack initiation and propagation in the process of thermal cycling [90, 91]. Molybdenum is one of the alloying elements that can improve the thermal fatigue resistance of cast iron [92, 93] because it can improve the tensile and yield strength and has a general effect on the thermal conductivity of materials.

Castings are affected differently in different working environments. In the thermal cycle, the service life of the workpiece is greatly affected by the environment due to the drastic changes in the temperature of the surface of the castings, so thermal fatigue cracks become easy to produce. Therefore, the treatment of the surface of the castings

has become an effective way. At present, surface treatment methods of grey cast iron include carburizing [94], carbonitriding [95], metal injection and gas deposition [96, 97], and laser treatment [98], which have been successfully applied in hot working molds [99].

1.2.3 Research status of wear of grey cast iron for drum brake

The wear failure mechanism of grey cast iron drum brake is mainly abrasive wear, and adhesive wear may exist with the difference of friction pair materials. Wear can be classified into sliding wear and rolling wear according to the characteristics of dynamic process. According to statistics, more than 80% of parts damage is related to wear and tear. The failure of drum brake is precisely due to the conversion of mechanical energy into heat energy caused by friction during braking, which produces thermal fatigue and oxidation reaction on the surface of the drum brake, affecting its friction and wear performance [100].

Abrasive wear is a common wear form, which refers to the phenomenon of material loss caused by hard abrasive particles squeezing or sliding on the dual surface under a certain load. Furrow action is equivalent to cutting action on the microscopic scale, which is the main wear mechanism of abrasive wear. Adhesive wear refers to a kind of wear in which the local adhesion occurs between the contact surfaces when two solids slide relative, and the sliding makes the shear fracture of the bonding site, resulting in the loss of the contact surface materials. Fatigue wear refers to cracks caused by plastic deformation on the surface of materials under cyclic stress, and

surface spalling occurs after a certain number of cycles. For example, failure of transmission gear or rolling bearing is mostly caused by fatigue wear [101]. However, the causes of thermal fatigue wear are more complex. On the one hand, the structure of the base material changes due to thermal cycling, and on the other hand, there is the effect of wear. Zhou Hong and other researchers conducted a number of studies on this issue and found that the strength and hardness of the base metal decreased with the thermal cycling, which was equivalent to the heat treatment of the material, resulting in more serious wear of the castings. After laser bionic treatment, the thermal fatigue and wear properties were enhanced [48, 102, 103].

The graphite and base metal hardness have a decisive effect on the wear property of grey cast iron. In oil sliding wear, it is because of the presence of graphite that grey cast iron has good wear resistance. The reason is that graphite can be used as a solid lubricant distributed on the friction interface in the friction state, and the graphite will form microscopic cavities in the original position after separation. These areas of original graphite are considered to be able to play the effect of oil storage and play a strong role in lubricating the friction of the boundary. However, under dry wear conditions, the void left after graphite separation increases the contact area between the base material and the air, which intensifies oxidation and reduces the oxidation resistance of the base material. Kinetic energy is transformed into internal energy in the friction process, which accelerates the oxidation of the base material. The subsequent shedding of oxide film not only aggravates the wear of the base material but also aggravates the wear after the shedding of oxide particles into abrasive

particles. The results show that when the hardness of the base material increases, the wear resistance will be improved.

In addition, the research direction of drum brake wear performance includes the traditional steel-iron system and the composite material system. The traditional steel-iron system is to improve the existing drum brake materials by improving the base material itself without changing the quality and other parameters of the drum brake. For example, as early as the 1980s, Japan prepared forged steel and cast steel heat-resistant layer on the surface of cast iron to meet the demand of Shinkansen speed increase [104]. Forging steel can improve the fracture toughness of zero parts. For some parts requiring better wear performance, researchers turn to other materials for research, such as the research and development of carbon/carbon fiber composites in European and American countries [105-109], and the research of aluminum matrix composites [110, 111]. Carbon/carbon fiber composites are characterized by strong crack resistance [112-114] and light material weight [115, 116]. By adding ceramic particles to aluminum alloy, the stability of aluminum alloy materials can be strengthened [117, 118], which can not only retain the lightweight characteristics of aluminum alloy, but also improve the elasticity, tensile strength and wear resistance of aluminum alloy [119]. There are also performance sports cars using composite materials in braking systems, but due to the high cost [120], not universal applicability, and the use of new technology is always accompanied by potential risks and instability, ceramic enhanced brake parts have occasionally been recalled.

To sum up, the preferred material of drum brake is still grey cast iron. The function of

brake parts such as drum brake is to convert the kinetic energy of vehicle into internal energy release. Wear and tear cannot be avoided, because a certain coefficient of friction needs to be guaranteed to ensure the safety of vehicle. Therefore, it is not feasible to reduce wear by adding lubricating oil and other methods. At the same time, as an important safety guarantee, brake parts need to be replaced in time. Considering economy and braking comprehensively, most factories use 200 or 250 grade grey cast iron drum brakes in actual production.

1.3 The theory of coupling bionic fatigue and wear resistance and the applications

1.3.1 Coupling bionics

Since ancient times, human beings have sought and learned from the nature of the survival rules and habits of objects, to imitate and learn the characteristics of organisms. In order to adapt to the environment, organisms in nature have undergone a long process of evolution and elimination [121], which provides us with endless tips and inspiration [121]. Since bionics was proposed by Dr. Steele in 1960 [122], relevant researchers have continued to conduct in-depth studies. Academician Ren Luquan et al., Jilin University [123-125] found that organisms in nature can adapt to the environment, which is not determined by a single element, but the result of multiple factors interacting, influencing and interdependent. Is the result of synergistic realization of several factors. Based on the above findings, coupling bionics is proposed.

Coupling bionics points out that a biological system with complete functions is composed of a variety of coupling elements, namely, factors that affect certain characteristics and functions of organisms, such as morphological coupling elements, structural coupling elements and material coupling elements. Some coupling elements exist objectively, but only appear in specific environments or conditions. For example, earthworms in soil are not easy to stick to soil on their body surface [126]. The reason why earthworms can have this characteristic is that there are micropores on the body surface that can secrete lubricant, and at the same time, there are various decouples involved, such as non-smooth structure and surface electroosmosis. By diastole and contraction of the body surface, some decouples can control the function of viscosity reduction and easy detachment [127].

A complete biological system requires the synergistic and efficient cooperation of several different coupling elements to achieve the maximum effect with the least energy consumption. Among them, different coupling elements are different in form, composition and structure. High efficiency means that the effect between each coupling element after coordination should be much higher than the mechanical addition of each coupling element. Based on coupling bionics theory, many researchers have achieved good results in viscosity reduction [128], noise reduction [129] and drag reduction [130, 131].

1.3.2 Coupling bionic of fatigue and wear resistance

Coupling bionics points out that the functions of organisms are not determined by a

single factor but are realized through the synergistic action of two or more kinds of coupling elements. Therefore, a technical system can be constructed by referring to a certain structure of organisms and their special work, and the constructed system can have similar functions by using the similarity relationship between the characteristics of organisms. For example, non-smooth hard scales on the surface of lizards and scorpions and flexible connective tissues under the skin can resist desert erosion with the cooperation of two coupling elements [19]. In addition, shell has good wear resistance, which is determined by the special structure and material coupling of shell surface [132, 133]. The common point of the above organisms is that they have ten similar body surface characteristics, and all of them are soft and hard phase structures. The hard units have different distribution according to the different materials and structures of the soft units, which makes them have excellent fatigue and wear resistance. The hard element can play a certain supporting role, is the main stress point in the wear process, and can effectively prevent fatigue cracks. Therefore, coupling bionic anti-fatigue and wear is a theory of improving the anti-fatigue and wear performance of materials by dealing with the material failure caused by thermal fatigue and wear that may exist on the surface of materials using the bionics idea.

1.3.3 The applications of coupling bionic fatigue and wear resistance

In recent years, there have been many applications of coupling bionic thought to improve the thermal fatigue and wear resistance of materials. For example, Wang [134] obtained an alternate soft and hard structure on the surface of vermicellar

graphite cast iron by inlaid casting method, and conducted relevant research on the thermal fatigue resistance of coupling bionic brake disc. It is found that the bionic surface of vermicular cast iron brake disc with different metals can effectively improve its thermal fatigue resistance. Huaqiang Lin et al. use the pulse method on the surface of alloy steel and carbon steel intermittent heating, that is, the electrode on the surface to achieve non-uniform heating, near the electrode point can be rapidly heated to melt the material phase change, then quenching makes the material hardening and strengthening, no electrode contact base metal is not heating and cooling process, so the organization does not change, In this way, an interphase structure of soft and hard is prepared on the surface of the material, and the research shows that the wear resistance of the steel is improved, as well as the resistance to crack initiation and propagation [135-137]. Ribeiro et al. [138, 139] carried out coupling bionic treatment on the abrasion-resistant roll, and welded the high chromium cast iron to the surface of the grinding roll with good toughness and strength but poor wear resistance by different welding methods. One of them was to process pits of different diameters on the surface of the grinding roll, and then surfacing the high chromium cast iron into these pits to obtain a hard phase with good wear resistance. Through this method, toughness and wear resistance can be taken into account on the same material surface, greatly improving the wear resistance of the grinding roll. Another method is to treat the used grinding roll. First, the surface of the grinding roll is flattened by a lathe, and then the material with good toughness is surfacing on the grinding roll surface to form a skeleton. The size of the skeleton is

the same as that of the grinding roller, and the same effect can be obtained by surfacing high chromium cast iron in the middle of the skeleton to form an alternating structure of soft and hard.

At present, the realization of coupling bionic anti-fatigue and wear applications mainly relies on laser processing. Using a laser to melt or cladding on the surface of materials to prepare hard units and form a soft and hard structure with the base material to improve its anti-fatigue and wear performance, which can extend the service life of corresponding parts. In addition, according to the coupling principle of biology, different coupling factor combinations can obtain different functions, and different models can be obtained by changing the corresponding coupling element parameters to meet different needs. The research in this aspect is mainly through optimizing the coupling design of different coupling elements such as structure, form and material, and preparing coupling bionic models on the surface of materials. The effects of coupling bionic technology on fatigue and wear resistance of materials were obtained and the service life of materials was improved. The main research contents are as follows:

In terms of the structural coupling element, researchers have studied the interphase structure of the rigid phase and base metal soft phase, such as the bionic model of point, bar and net. Zhikai Chen et al. [140] studied the rolling fatigue of grey cast iron and found that coupling bionic treatment could improve rolling fatigue resistance of grey cast iron. Yuan Yuhuan [141] processed a combined bionic model such as point-strip mesh on the surface of aluminium alloy and found that the combined

model could improve the mechanical properties and wear resistance better than a single model. Haifeng Zhang [142, 143] adjusted laser parameters to prepare the coupling bionic unit of the same height as the base material and lower than the base material. Later, they conducted lubrication friction experiments on the guide rail of the machine tool respectively and found that the lower than the base material will increase the oil storage on the material surface, which can improve the wear resistance of the guide rail.

In the aspect of the morphological coupling element, the main research content is to study the characteristic quantity of coupling bionic elements, such as the element size, shape, distribution and other factors, according to the characteristics and functions of the target processing object and explore the influence law of different morphological elements on the fatigue and wear resistance of the object. When Sun Na et al. [144, 145] studied the wear resistance of vermicular cast iron, they found that the wear of the dot bionic model, strip bionic model and grid bionic model decreased by 39%, 50% and 77% respectively compared with the untreated samples. Zuobo Pang et al. [146] conducted a quantitative analysis of the relationship between the surface units of grey cast iron and the wear resistance of the base material and established the regression equation of the units and wear resistance, which means that the characteristic parameters of the units can be designed according to the demand of the target object on wear resistance, which is the basis for the design of coupling bionic model. At the same time, the influence of the shape of the coupled bionic unit on the wear resistance of grey cast iron under dry reciprocating sliding was studied [147],

and the results showed that the grid unit had the best wear resistance. Zhikai Chen also conducted related studies on morphological coupling and found that different shaped elements have different elevations on fatigue wear resistance of grey cast iron [148]. When the material surface pressure is constant, different-shaped units bear different pressures, which means that the matrix bears different pressures. Therefore, the improvement degree of fatigue wear resistance of the base metal is different, and it is found that the improvement degree of grid unit is relatively the highest. Wanshi Yang et al. [149]carried out-coupling bionic treatment on train track steel and studied the influence of different forms of units on rolling contact fatigue and wear resistance of track steel. Since the track is under huge positive pressure, it can bear more pressure than the base metal element, so the unit can improve the anti-fatigue performance of track steel. Among them, the sample with the hard-core form has better fatigue resistance. Chao Meng et al. [150]found that U-shaped units have more advantages in blocking fatigue cracks than V-shaped or flat units. It takes more time and energy for fatigue cracks to pass through U-shaped units, so the fatigue resistance is stronger.

In terms of material coupling element, material coupling element not only refers to the coupling of different materials in a broad sense but also includes materials with the same composition but different organization. After laser melting treatment on the surface of materials, the element part and the base material part are regarded as two different materials. The monomer and the base material prepared on the surface of the material by laser cladding technology are also two kinds of materials with different

compositions. Peng Zhang et al. [151]used laser cladding on the surface of photospheric graphite cast iron to strengthen the units, which greatly improved the wear resistance of the units compared with the melting units. Zhengjun Jing et al. [152] studied the influence of laser cladding WC elements on the wear resistance of grey cast iron after thermal fatigue and found that the decomposition ability of carbide of cladding elements was weakened in the thermal fatigue process, and the strength hardness was increased, so the wear resistance was improved. In order to improve the wear resistance of low-carbon alloy steel, Qi Sui et al. [153] studied secondary laser carburizing to prepare individual units of different shapes. As a result, the carbon content in the unit was increased, the hardness was significantly improved, and the corresponding wear resistance was improved. In addition, there are other technologies related to unit processing through water medium laser. In water medium laser processing, a thin film is prepared on the surface of the material to be processed. The laser beam penetrates the water film to melt the material. Some researchers have also used laser cladding technology to simultaneously clad carbon and chromium onto the surface of grey cast iron to obtain higher hardness in the laser cladding area and better wear resistance in the event of wear [154].

As for the bionic model feature quantity, the main research scope is the distribution characteristics and arrangement mode of the unit. Su Wei et al. [155, 156]studied the influence of the distribution angle of units prepared by laser on the wear resistance of steel dry sliding wear, as well as the relationship between the spacing of units and wear resistance. They found that the wear resistance is the best when the distribution

angle and friction direction of units are 45°, and the smaller the spacing of units, the better the wear resistance. But the units cannot be connected during processing. Other researchers studied the relationship between bionic element direction and fatigue wear of grey cast iron and found that along the direction of rolling contact line, the longer the length of contact element, the better the fatigue wear resistance performance. The reason is that the pressure on the contact line is certain, and the longer the length of contact element means the greater the pressure on the unit. The lower the pressure on the base metal. In addition, the effect of bionic unit distribution density on the wear resistance of 7075 aluminium alloy showed the same results as the Su Wei study [156].

1.4 The bionic prototype of fatigue and wear resistance

Any biomimetic research has its reference biological prototype in nature, but it is almost impossible to resist biological prototype in nature with temperature extremity of 700℃ caused by friction. According to similarity science [157], human can solve scientific and technological problems related to similarity in related fields by looking for similarity in nature. For this study, it is to use the special structure and function of some organisms as the principle, design and build similar technology systems, and effectively apply the bionic idea. As the main failure mode of grey cast iron drum brake is thermal fatigue crack caused by brake friction, it is necessary to find biological prototype that can resist crack initiation and expansion and wear in nature, and then imitate its structure, form and material coupling elements. In this study,

shells, leaves and dragonfly wings were selected as biological prototypes for coupled bionic thermal fatigue and wear resistance research.

1.4.1 Shell nacreous layers

Shells have existed on the earth for hundreds of millions of years. Due to the harsh living environment, they are not only eroded by seawater in the ocean, but also affected by surface wear and temperature changes caused by sand. Under various tests, shells are still common creatures, mainly due to the special organizational structure of shell surface [158, 159], which has high strength and toughness. Giving it the ability to survive in the ocean. Fig.1.2 is a schematic diagram of the shell nacreous layer. It can be seen from the diagram that hexagonal inscription tablets constitute the basic structural unit of the shell nacreous layer, forming the aragonite layer, which is connected with the organic matrix layer to form the nacreous layer [160, 161].

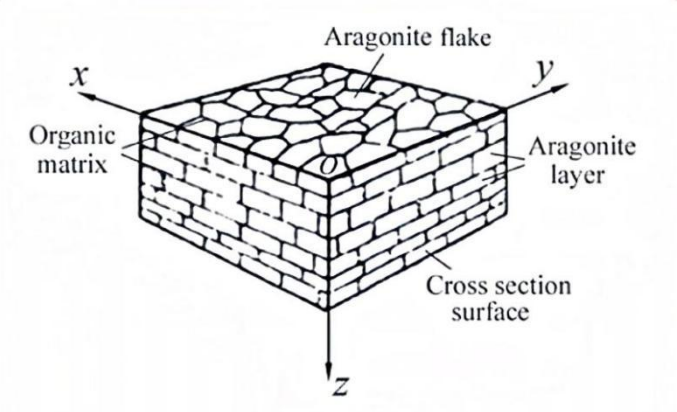


Fig.1.2 Sketch of structure of nacreous layers [162]

KAMAT et al. [163]studied the fracture behavior of shell nacreous layer and found that cracks did not pass through directly when growing to arachite layer, but

frequently deviated at the interface between organic layer and inorganic layer, as shown in Fig.1.3. As for the fracture behavior of nacre, some scholars have studied and observed the crack deflection phenomenon, which is the main toughening mechanism of nacre. There are two main reasons: the first is that the path increases after the crack deflection and absorbs energy in the process of propagation; the second is that the crack deflections from the direction of stress favorable state to the direction of stress unfavorable. However, the current stress state will cause the crack growth rate to slow down [164]. Therefore, shell nacre has a good crack arresting effect, and it has become a natural biological prototype for coupling bionic anti-fatigue crack research.

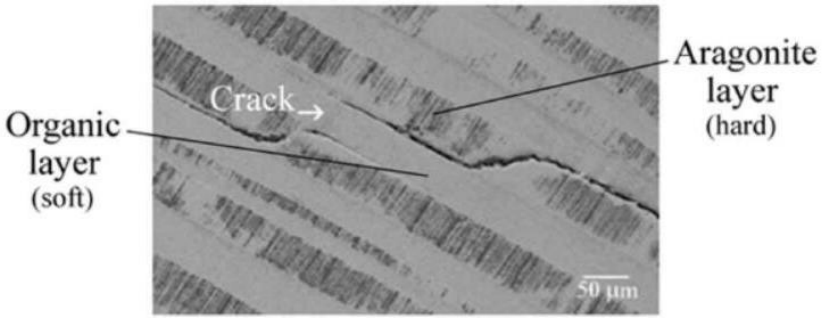


Fig.1.3 Sketch of crack deflection in nacreous layer

1.4.2 Plant leaves

After observation of plant leaves, it was found that although leaves were mostly exposed to the natural environment, damaged by storms, temperature difference between day and night, and the change of four seasons, most of them remained intact due to the special structure of leaves. It has been found that plant leaves are mostly composed of veins and mesophyls between veins. Mesophyls are composed of spongy

tissues and palisade tissues, which are soft in texture and easy to be deformed and damaged by external forces. The distribution of leaf veins shows certain rules, and they are composed of vascular bundles and some mechanical tissues, with good tensile performance and strength, ensuring the overall strength and toughness of the leaves [165, 166]. It is precisely because of the above special structure of the blade, when cracks appear in the mesophyll part, the cracks will expand in a straight line in the mesophyll region. Due to the obstruction of the blade veins, the cracks will be diverted at the connection of the mesophyll blade veins [167, 168], as shown in Fig.1.4. The continuous extension of cracks along the original path will lead to the tear of positive leaves, but because of the action of the vein, the path becomes longer, and the life of the leaves is extended. The coordination between the parts of a plant's leaves is the result of billions of years of evolution.

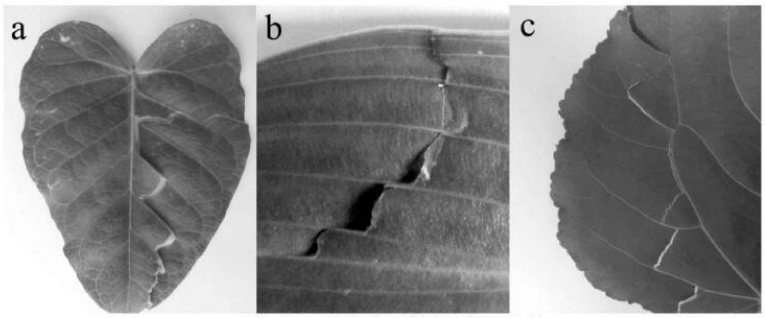


Fig.1.4 The crack in leaves

1.4.3 Dragonfly wings

Organisms with wings in nature all need to face bad weather conditions and complex living environment. Dragonfly wings vibrate 20 to 40 times per second during flight, and the speed can reach 70 kilometers per hour. In such a high-speed flight, the

surface of the wings will generate strong power, and the friction with the atmosphere will also generate the same strong alternating stress. The initiation and propagation of cracks is inevitable. The research on dragonfly wing cracks found that the cracks expanded in a straight line in the wing membrane region and deflected in the wing veins until the whole wing broke, as shown in Fig.1.5 [137, 169, 170]. Because the cracks on the surface of the wing mainly spread in a straight line, the deflection of the cracks due to the relationship between the wing veins extends the life of the dragonfly wing to a certain extent. It is precisely because of the coupling between the structure, material and shape of the wing membrane and the veins of the wings of dragonfly that the wings not only have a relatively light weight, but also can resist the complex environment with the optimal combination.

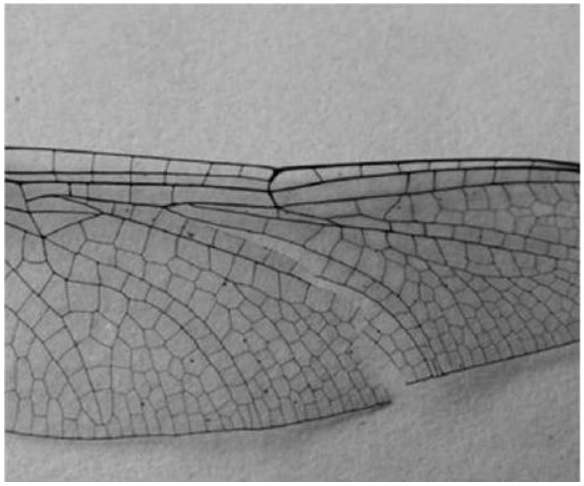


Fig.1.5 Deflection of dragonfly wing crack

1.5 Laser coupling bionic processing technology

In the 1960s, laser was invented and attracted attention from various fields. Special functions such as high directivity, high brightness and high coherence enabled laser to

play a role in many fields and realize things that could not be realized in the past. Therefore, it became one of the most important scientific inventions of the 20th century. In particular, it has achieved technological breakthroughs in the processing industry [171, 172], which has the following characteristics:

1. Laser processing is a non-contact processing method without extra mechanical force, and the energy, moving speed and direction of the laser beam are controllable and adjustable, with good controllability.

2. Laser beam high energy, so it can process high melting point and high hardness of materials, and metal and non-metal materials can be processed.

3. Laser can be local processing, processing area according to the change of laser spot changes, processing speed is fast, the heat affected area is very small, the thermal deformation of the processed material is small.

4. The use of laser processing is stable and reliable, high production efficiency, laser cutting and laser marking technology has been put into use in automated factories.

The characteristics of laser processing mean that laser has great advantages for metal surface processing. In recent years, laser processing has been widely applied in metal surface, such as surface modification and welding [173]. Especially in surface modification, automatic processing can be realized by cooperating with robots, and laser hardening can be realized on material surface. Laser cladding and laser melting, etc.

Laser quenching refers to the method of using laser to heat the surface of the base material above the phase change temperature and below the melting temperature to

harden the surface of the material [174]. The advantage of using laser is that the heat affected zone is very small, only the phase change occurs in the laser irradiation zone, and the operation is simple, and the process is mature. However, the laser energy during laser quenching is relatively small, and the absorption of laser energy on the surface of the material is poor, so it is necessary to pretreat the material. The main difficulty at present lies in the problem of pre-treatment of the material. Wu Xiaoyu et al. [175, 176]studied the microstructure of stainless steel after laser quenching, and the results showed that the microstructure changed into fine and uniform strip tempered martensite after laser processing, and the strength and hardness increased.

Laser cladding technology [177, 178] adds metal or non-metal powder to the surface of the material through spraying or precoating technology, which melts after being irradiated by laser with high energy, to change the composition of the material surface and thus the structure of the base material, and obtain oxidation resistance, wear resistance and other properties [179]. The advantage of laser cladding technology is that the strengthening layer can be closely combined with the base material [180, 181], and the corresponding alloy elements can be selected for cladding according to the requirements of the parts. However, the disadvantage is that the laser energy output in the cladding process is limited, and the alloy elements of cladding are limited, which cannot improve the performance of the material surface on a large scale. Moreover, the thermal physical properties of the reinforced layer, such as thermal conductivity and specific heat, are different from those of the base material. When the service environment of parts changes, the internal stress between the reinforced layer and the

matrix will be generated due to the temperature difference, which becomes the potential threat of fatigue cracks. Laser cladding ceramics [182-184] can be mechanically mixed with the base material after the ceramic material is melted to form a cladding layer composed of ceramic materials. In this way, the surface properties of the material are determined by the cladding ceramic material, and the properties of the cladding layer can be changed by changing the thickness of the cladding layer, material composition and laser parameters [185, 186]. In addition, the cladding materials are generally coated with iron powder, nickel powder and other powders, which can make the compatibility between ceramic materials and base materials better [187, 188]. After laser cladding, the wear resistance and corrosion resistance of the material surface are improved. It is an additive manufacturing method that can be used to repair the surface of parts, with obvious advantages. However, the disadvantage is that the research and design of cladding powder are less, cladding technology is restricted to a certain extent, the thermal physical properties of cladding layer and base material are different, in service state is easy to produce internal stress due to temperature difference, resulting in cracks, additional measures are needed for pretreatment or slow cooling treatment, which is also a factor restricting cladding technology. In addition, there are still technical difficulties in the use of laser cladding on a large area of cladding, cladding layer is difficult to ensure uniformity and stability, and parts with higher quality requirements need to retain processing allowance.

Laser melting technology [189-191] is a technology that uses high energy density

laser beam to irradiate the surface of materials and form a molten pool with a certain depth in the irradiation area. After cooling, a refined structure is formed in the melting area to obtain higher hardness and strength, so as to enhance the fatigue and wear resistance of materials. It is the method adopted in this research topic. Laser melting has a rapid strengthening process, which conforms to the theory of rapid melting [192, 193]. The main advantage is that, unlike laser cladding, no other alloy elements are required, and regions with controllable size and high hardness can be obtained in the melting process. The bonding between the melting region and the base material matrix is good. However, this technology also has some shortcomings, such as surface roughness increased after laser melting processing, according to the different needs of the base material to adjust the laser parameters, otherwise it is easy to appear pores and cracks and other defects.

At present, most of the research on the use of laser surface modification is based on the whole surface of the material [194-197], meaning that the surface of the matrix surface is uniform, the surface of each area of the composition, hardness and strength is basically the same, can affect the processing area of the factors that the difference of processing technology, a process corresponds to performance. However, the operational coupling bionics idea is inspired by organisms in nature. On the surface of the target material, different processing models are designed according to the requirements and different areas. It has the advantage of two parts of materials or organizations at the same time, which makes up for the deficiency of two kinds of materials or organizations. It can improve the wear resistance while maintaining good

strength and toughness, improve the anti-fatigue and wear performance of parts and prolong the service life. Laser coupling bionic processing technology only needs a single process, according to the requirements of the laser parameters or processing model characteristics can be designed, the process is simple and save the processing cost. Relevant researchers have carried out a lot of research on laser coupling bionic processing technology [198], proving that the surface of materials can be processed with high energy density, good directivity, small heat-affected zone and other characteristics, which are similar to that of the base material. The structural characteristics similar to the surface of biological materials in nature can significantly improve the fatigue and wear resistance of materials. The perfect combination of bionics and laser processing technology.

1.6 The main purpose and significance of the thesis

Drum brake is one of the important parts of vehicle braking system, which is the guarantee of life and property safety in transportation industry. At present, the drum brake is mainly made of grey cast iron. During the braking process, due to the large friction torque, the working surface of the drum brake heats up rapidly. Then, due to the air cooling in the process of moving and the good thermal conductivity of the metal itself, the surface temperature drops rapidly. Therefore, improving the thermal fatigue and wear resistance of drum brake is not only helpful to promote the research of properties of grey cast iron, but also has practical significance to protect life and property safety.

In this study, the laser coupling bionic processing method is mainly adopted. The structure coupling unit is prepared on the surface of grey cast iron used as drum brake material. The laser parameters are selected according to the thickness of the processed object, and the relationship between the laser parameters and the thickness of the sample is obtained. The unit is processed on the surface of grey cast iron with different matrix, the influence of base metal coupling unit on coupling bionic treatment is explored, and the influence of morphological coupling element characteristic quantity on the thermal fatigue resistance and wear performance of grey cast iron is analyzed. The coupling imitation model is designed according to the failure characteristics of the drum brake, aiming at improving the thermal fatigue resistance and wear performance of grey cast iron drum brake and improving its service life. It provides data support for the application of laser coupling bionic processing grey cast iron in the industrial field and provides theoretical basis for the application of coupled bionic drum brake in practical production. The main research contents of this study are as follows:

1. In order to prepare high-quality structural coupling element units on the drum brake face of grey cast iron trucks, the results of processing samples of different thickness with the same laser parameters were studied. Finite element simulation software was used to analyze the temperature distribution in the laser melting region, and the influence rule of thickness on laser coupling bionic processing was studied.
2. The laser parameters used in the processing of drum brake are optimized, and the

orthogonal test scheme is designed to optimize the optimal parameter combination. The structure coupling element is studied.

3. Analyze the influence of base material coupling element on the thermal fatigue and wear resistance of grey cast iron and compare the influence of base material couplings on the thermal fatigue and wear resistance of grey cast iron with coupling bionic surface.
4. According to the failure characteristics of the drum brake of grey cast iron, the morphological coupling element characteristic quantity of the coupling bionic unit is designed, and the thermal fatigue and wear resistance of the coupling bionic grey cast iron with different morphological coupling element characteristic quantity is evaluated after the test. Based on the coupling bionic theory, the best morphological characteristic quantity suitable for the drum brake is selected and combined. A combined coupling bionic model specially used for machining drum brake surface was designed and compared with the untreated drum brake, and the mechanism was analyzed.
5. Trial production of several combined coupling bionic drum brakes, design and carry out bench test, and evaluate and analyze the bench test result.

Chapter 2: Experimental Study

2.1 Experimental materials

The sample base materials in the third chapter, the fifth chapter, the pearlite part of the sample base in the fourth chapter, as well as the drum brake used in the sixth chapter, were all taken from a batch of grey cast iron truck drum brakes produced by Guangdong Fuwa Heavy Industry Manufacturing Co., LTD. The samples in this thesis are cut from the drum brakes. The grey cast iron grade in this thesis is 200. The chemical composition of the grey cast iron used in the drum brake is shown in Table 2.1. The microstructure of the grey cast iron is shown in Fig.2.1, which shows that the grey cast iron is composed of graphite, pearlite, ferrite, and a small amount of phosphorus eutectic.

Table 2.1 Composition of the grey cast iron (wt. %)

Composition	C	Si	Mn	P	S	Cu	Cr	Fe
Content	3.450	1.770	0.820	0.060	0.059	0.500	0.270	Bal.

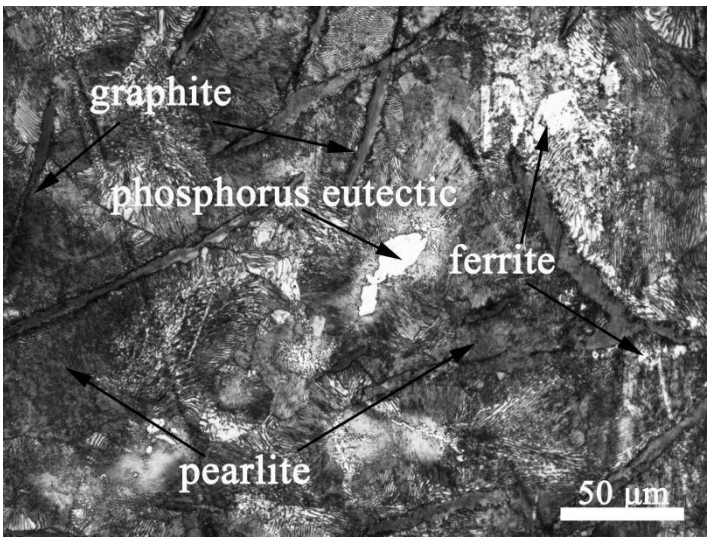


Fig.2.1 Microstructure of grey cast iron

In the fourth chapter, the research of graphite type and carbon content on the thermal fatigue and wear resistance of coupling bionic sample part, the base material is from self-made grey cast iron, and the chemical composition is shown in Table 2.2 and Table 2.3. The casting process of the materials studied in the two parts is different. A and C in Table 2.2 are cast by wet sand mold; samples B and E are cast by resin self-hardening sand mold with a relatively thin mold wall; sample D is cast by metal mold. The sample base material in Table 2.3 is cast by wet sand mold. Cast iron and scrap steel are selected as the charge, and grey cast iron is prepared by adjusting the carbon content. The casting equipment is a 5kg medium-frequency induction electric furnace of Nanling Casting Laboratory of Jilin University. The casting temperature range is controlled from 1290 to 1300 degrees Celsius, and the temperature of molten iron is about 1450 degrees Celsius.

Table 2.2 Compositions of different graphite types samples

Composition (wt. %)						
Samples	C	Si	Mn	P	S	Fe
A	3.18	1.65	0.92	0.02	0.01	Bal.
B	3.42	1.62	0.89	0.02	0.01	Bal.
C	3.56	2.10	0.02	0.01	0.01	Bal.
D	3.26	2.46	0.51	0.04	0.01	Bal.
E	2.68	1.67	0.89	0.02	0.01	Bal.

Table 2.3 Compositions of different carbon content samples

Composition (wt. %)						
Sample	C	Si	Mn	P	S	Fe
a	2.88	1.15	0.11	0.01	0.01	Bal.
b	3.08	1.58	0.91	0.02	001	Bal.
c	3.27	1.61	0.88	0.02	0.01	Bal.
d	3.44	1.60	0.90	0.02	0.01	Bal.

2.2 Preparation of samples

The samples in the thesis are divided into two categories: blank samples and bionic samples. Bionic samples refer to the samples with coupling bionic units processed by laser on the surface, while blank samples refer to the unprocessed samples, as shown in Fig. 2.2 and Fig. 2.3. The size of the sample in the thesis is 40×20×6 mm^3, cut by CNC DK7732 EDM wire cutting machine. A small hole is drilled on the back of the

sample using a hand drill with a 1mm bit for hanging the sample on the hanging plate of the thermal fatigue testing machine. 80 mesh, 150 mesh, 360 mesh, 800 mesh, and 1000 mesh sandpapers are used for grinding samples until the surface is not visible to the naked eye the cutting trace and effect observation of sample scratches, then the sample is cloth fixed on the polishing machine surface polishing. The purpose is to remove all the scratches, finally using anhydrous ethanol solvent for cleaning the whole sample. The bionic sample is a sample containing a coupling bionic unit processed by laser, which is combined into a model according to certain characteristic quantities, and the coupling bionic model is processed on the surface. The coupling bionic unit is shown in Fig. 2.4. The unit is the area of rapid cooling after laser irradiation on the material surface. After the laser is used to process the unit on the sample surface, the sample surface is subdivided into three areas, namely, melted zone, transformed zone and base zone. By changing the distance and angle of the coupling bionic units, the units are arranged in a certain shape to obtain different coupling bionic models. Fig. 2.5 shows the laser machining system and the drum brake being processed. The system consists of a laser, water cooling system, numerical control system and rotating table. The laser in the thesis is Nd:YAG laser, which is JHM-1GY-300B type pulsed laser machine produced by Wuhan Chutian Laser Equipment Co., LTD. The maximum output power is 800W and the wavelength is 1.06μm. Samples when needed is obtained by the selected laser parameter control manipulator model of manipulator control the X and Y axis movement speed, adjust the position of the Z axis to control the laser from the focal spot size, ensure all the

machined surface in the required position, preparation of the coupling bionic unit size, shape and structure. When processing the drum brake, it is necessary to cooperate with the rotating table (ZY Show Industry Machinery Turntable). The manipulation moves according to the path planned and set by the servo control system in advance, and the corresponding coupling bionic model surface is obtained.

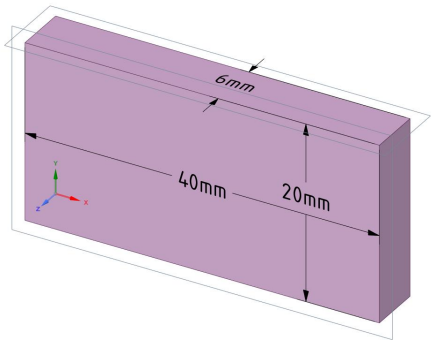


Fig.2.2 Schematic of the blank sample

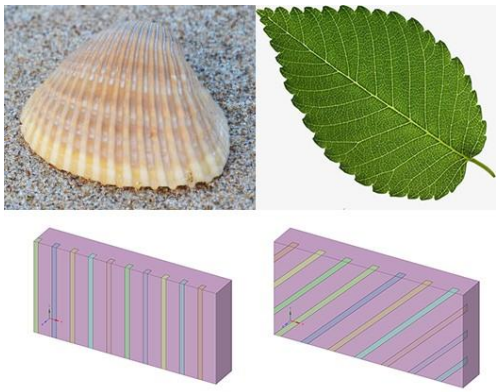


Fig.2.3 Schematic of the bionic samples

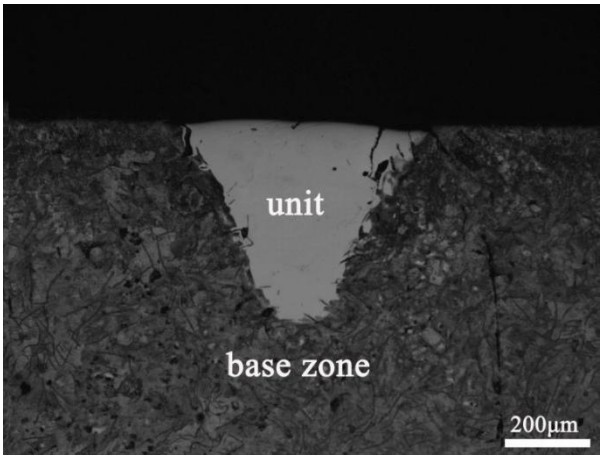


Fig.2.4 Coupling bionic unit



Fig.2.5 Laser processing system

2.3 Microanalysis and performance testing

2.3.1 Observation of microstructure

In Chapter 3 and Chapter 4, the microstructure and unit of the samples need to be observed. The electric discharge wire-cutting machine is used to cut along the vertical direction of laser processing. The cross-section is polished with sandpapers of 80 mesh, 150 mesh, 360 mesh, 800 mesh, 1000 mesh, and 1500 mesh until there is no cutting trace. The cotton cloth was then polished with diamond polishing paste until there were no scratches. The cross-section was corroded with a 4% nitrate alcohol solution for about 30 seconds, and then the sample was rinsed with absolute ethanol

and placed in a desiccant for preservation. The optical microscope Zeiss Axio Imager A2m was used to observe the cross-section morphology of the units, grey cast iron graphite type, graphite content, pearlite content and spacing.

2.3.2 SEM and EDS

Optical microscopy uses visible light as the light source, so the resolution is limited. Scanning electron microscopy (SEM) is needed to observe some specific areas, such as the transformed zone of unit and the extremely fine interlamellar spacing of the pearlite. The samples were corroded with 20% H_2SO_4 ethanol solution for 40 minutes, and the other samples were corroded with 4% nitric acid alcohol solution. The device is a Zeiss EV018 scanning electron microscope. To analyze the elemental composition of areas such as cracks and graphite pits, the British energy spectrometer called Link-ISIS fitted to a scanning electron microscope was used.

2.3.3 Microhardness

The microhardness in this study is measured by the American Buehler 5104 automatic Vickers hardness tester, including the hardness of the different base metals, different pearlite content and spacing of the hardness and the hardness of the unit and the base metal. The load used is 0.2 kg and the pressure holding time is 10 seconds. Each sample was measured 5 times, and each hardness value was averaged 5 times.

2.3.4 Phase analysis

The phase composition of the different materials and the unit is determined by XRD (X-ray Diffraction) using a Nissan Rigaku D/Max 2500 (X-ray Diffraction) apparatus. The samples to be tested needs to be cut into $10mm^3$ cubes. The voltage of the firing tube is set to be 40 kV, the current is 40 mA, and the scanning step is 1 degree per minute. The experimental results were analyzed and calibrated by Jade 5 software.

2.3.5 Thermal fatigue test

In the thermal fatigue test, a self-restrained resistance furnace heating thermal fatigue machine was used, as shown in Fig. 2.6. The thermal fatigue machine is composed of a motor, a limiter and a lead screw. The motor is responsible for providing power, and the limiter is used to fix the heating and cooling position of the sample. At the same time, the limiter and the time control part constitute the automatic heating and cooling cycle. The samples were suspended on hanging plates in the furnace to ensure consistent heating and cooling conditions for all samples. The heat source comes from the K-type thermocouple in the furnace, and the other end relates to the temperature control meter to control and measure the temperature. The thermal fatigue machine is water-cooled, and the flow cold water circulation is placed under the resistance furnace. The cooling and heating temperatures are 25 ± 5 ° C and 700 ± 5 ° C, the cooling time is 5 seconds, the heating time is 180 seconds, and the reciprocating time is recorded as a thermal fatigue cycle, and the counter is used to automatically count until the preset number of the automatic stop.

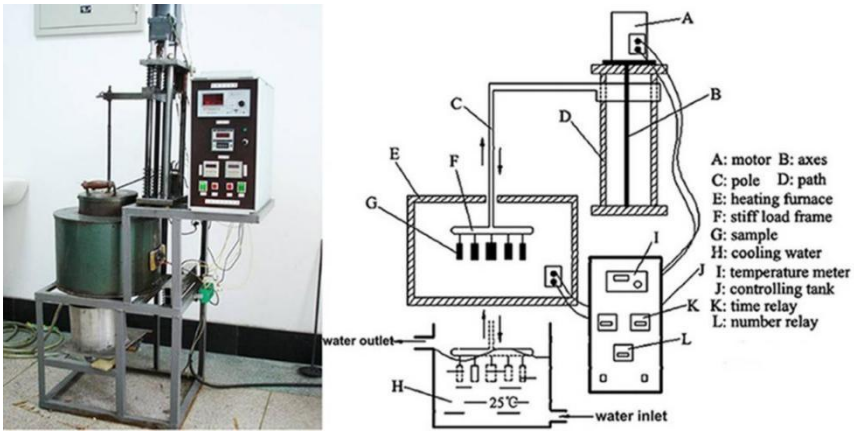


Fig.2.6 Thermal fatigue testing machine

All the samples have been polished before the thermal fatigue test, and there is no mechanical trace on the surface, which ensures that the initiation and propagation of thermal fatigue cracks are only related to the material itself. The thermal fatigue test part of this article deals with the fourth chapter and the fifth chapter, the fourth chapter is the study of the base metal thermal fatigue and wear resistance of bionic coupling grey cast iron. Compared with the coupling bionic model design in Chapter 5, the thermal fatigue test in Chapter 4 is more likely to show comparative results under the same experimental conditions. Therefore, in order to improve the experimental efficiency, the number of cracks and the length of the main crack (the longest crack) were counted in the thermal fatigue test in Chapter 4 after every 50 thermal cycles, and the sample was taken out for statistics after every 200 thermal cycles in Chapter 5. The AXTL-2400 optical continuous zoom microscope was used to observe statistical cracks, cracks above 1 mm were included in the statistics. The thermal fatigue resistance is evaluated according to the number of thermal fatigue cracks and the length of the main crack.

2.3.6 Wear test

The drum brake has obvious directionality during braking. In order to match the actual working conditions, the wear test in this study is carried out on the self-made reciprocating wear test machine, as shown in Fig. 2.7. The testing machine is composed of a servo motor, link drive, controller, counter and wear test area. The servo motor and the connecting rod drive work together to achieve the reciprocating motion, and the controller is used to set the speed and time. The friction pair is a special ceramic friction pair for the brake disc. The load is 60N, the speed is 700R /min, the wear time is 10 hours, and the friction state is dry sliding friction without lubrication. The samples that need to be worn out should be soaked in an absolute ethanol solution, cleaned in the ultrasonic cleaner for 15 minutes, and then blown dry. The FA2004 electronic balance was used to weigh the sample before and after the experiment, and the accuracy was 0.001 grams. The difference between the front and the back was the result of the wear experiment, and each data needed to be measured 5 times to take the average value. The wear morphology was detected by the American VEECO NT9100 optical profiler and 3D laser confocal (LEXT-OLS 3000 Olympus), and the wear loss weight was used as the basis to determine the wear resistance.

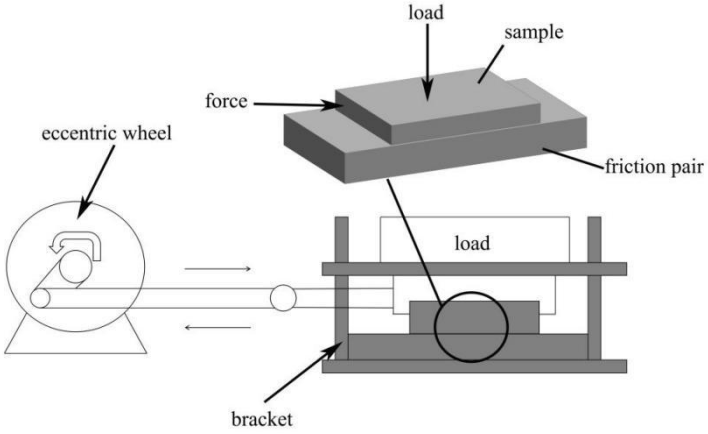


Fig.2.7 Schematic of wear testing machine

2.3.7 Bench test

The drum brake bench test can test the performance of the drum brake under a harsh experimental environment. In this study, three drum brakes with coupling bionic surfaces were prepared, plus a blank control drum brake. A total of four drum brakes were tested on the bench. The drum brake is produced by Guangdong Fuhua Company in the same batch. Fig. 2.8 is the schematic of the outside of the drum brake and the braking surface (laser machining surface). The drum brake has a height of 226.5 mm, and a circumference of 1417 mm. Fig. 2.9 shows the preparation work before the experiment. First, the drum brake is fixed to the bench test bench, while the brake pads are mounted and fixed, and then the two are connected and ready to start the experiment. The experimental condition is to start braking immediately after the drum brake is accelerated from static to 96km/h until the drum brake stops, which is recorded as a cycle. After 200 cycles, the drum brake was removed from the test bench every ten times, and the penetration reagent and imaging reagent as shown in

Fig. 2.10 were sprayed on the braking surface to observe the crack morphology and count the number of cracks. After cleaning the braking surface with a cleaning agent, the test was continued until the main crack broke through the top and it was finished. The friction coefficient is directly read out by the bench test bench, and the friction coefficient of all the drum brakes in the bench test process is averaged and recorded.



Fig.2.8 Grey cast iron drum brake and working surface

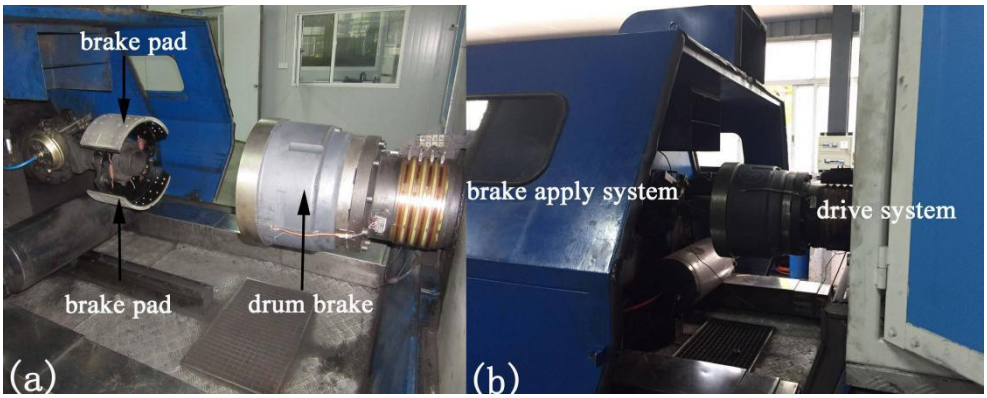


Fig.2.9 Bench testing machine



Fig.2.10 Crack detection reagent

2.3.9 Ansys finite element analysis

In Chapter 3 and Chapter 5, the relationship between the temperature gradient in the laser melted zone and the samples with different thicknesses, as well as the surface stress distribution of the coupling bionic model were simulated by Ansys simulation software. Firstly, the 3D geometric models of different samples were drawn according to the actual situation, and then the physical parameters of the base metal and unit were defined. After dividing the mesh, boundary conditions were set, the corresponding temperature field or stress field cloud image was obtained. See Chapters 3 and 5 for details. Fig. 2.11 shows the schematic diagram of the mesh division of temperature distribution in the simulation of the laser single-point machining sample, and Fig. 2.12 shows the schematic diagram of the mesh division of equivalent stress distribution in the simulation of the coupling bionic model. By simulating the instantaneous heat transfer on the laser-machined sample surface, the relationship between the same laser parameters and the sample thickness can be found with the help of the temperature distribution image, which provides support for how to process the same quality of the coupling bionic unit on the sample surface of

different thickness. In addition to the weight loss, surface roughness and wear morphology, the wear mechanism can also be analyzed by comparing the equivalent stress distribution of different coupling bionic models.

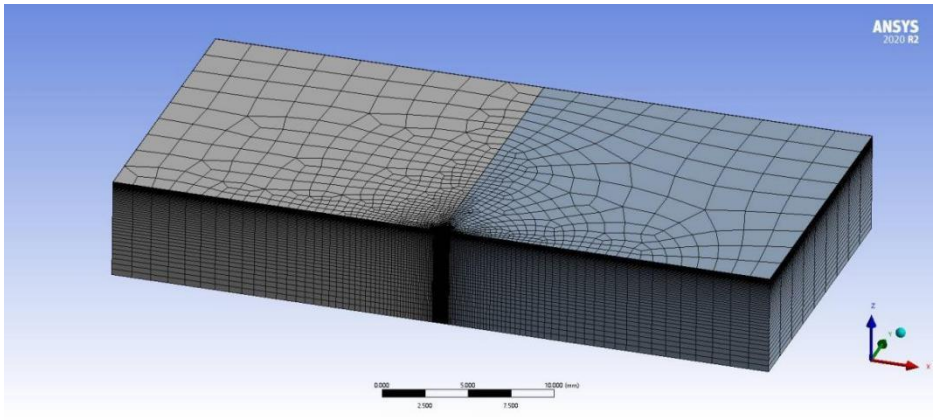


Fig.2.11 The meshing method of models for temperature

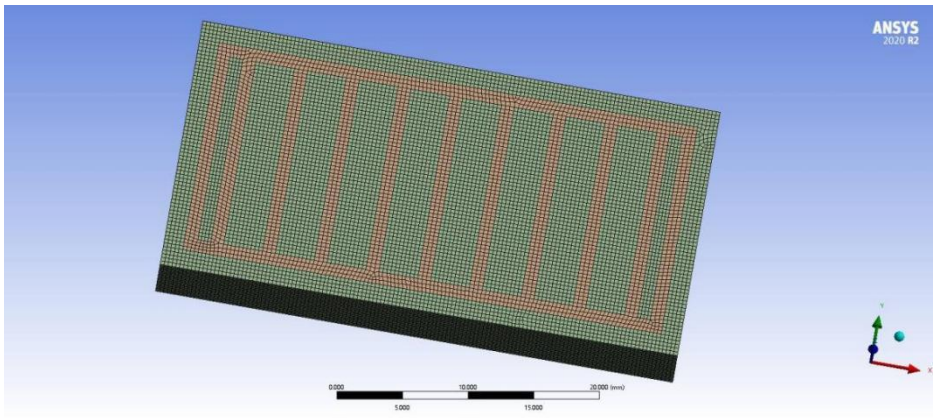


Fig.2.12 The meshing method of models for equivalent stress

Chapter 3: Parameter Optimization of Structural Coupling Element Unit of Grey Cast Iron Truck Drum Brake

3.1 Introduction

In recent years, excellent progress has been made in the research of laser machining of material surfaces, and the use of laser melting technology has created many cost-effective manufacturing processes [199-201]. Laser coupling bionic treatment has been proven to be able to effectively improve the surface properties of materials, but the current research on laser coupling bionic treatment is derived from the laboratory, after the surface of a certain material sample is processed. The research object of this thesis is the truck drum brake. Considering that the base material is the same, but the wall thickness difference between the sample and the drum brake is large, it is obviously unreasonable to transplant the relevant research results directly to the drum brake. Therefore, it is necessary to verify the results and analyze the mechanism of the same laser parameters processed on samples with different thicknesses. Secondly, the influence law of sample thickness on laser energy was found, and then the laser processing parameters suitable for the drum brake working face were optimized to find the structural coupling unit with similar characteristic values to the laboratory sample to ensure that it has similar thermal fatigue resistance and wear resistance. Finally, the relationship between the samples with different thicknesses and laser energy is found, which provides a reference for the practical application of laser coupling bionic machining in the future.

In this study, to improve the thermal fatigue and wear resistance of grey cast iron truck drum brake, the coupling bionic unit is prepared on the working surface of the drum brake by using laser melting technology. After the laser scanning on the surface of the material, the irradiated area quickly melts, forming a certain volume of melting area. After the laser spot leaves, due to the heat conduction of the metal, the melting area quickly cools and solidifies, and the cooling rate is relatively high, making the grey cast iron base metal undergo structural transformation. The transformed area is the coupling bionic unit in this research. The bionic structure of "hard and soft phases" is formed by the coupling element of the unit and the matrix. Laser processing parameters (current, pulse width, frequency, scanning speed, defocus) play a decisive role in determining the depth, width, porosity, and crack of the unit [202-204], and different laser parameters have different effects on the characteristic values of the unit [11]. The characteristic value of the unit of this research has certain requirements, such as a large deep wide than in truck drum brake can not only ensure unit surface occupies a certain area, but also because of a certain depth increases of thermal fatigue crack, surface abrasion, prolong its service life, reduce the number of pores can avoid in the unit internal crack initiation, and so on. Therefore, choosing appropriate laser processing parameters for grey cast iron truck drum brakes is the guarantee of obtaining high-quality unit, and is an important prerequisite to effectively improve the thermal fatigue and wear resistance of drum brakes.

To sum up, the main research contents of this chapter are as follows :(1) Determining the machining results of the same laser parameters on the surface of samples with

different thicknesses and analyzing the mechanism; (2) The laser processing parameters of drum brake were optimized by orthogonal test, and the characteristic values of structural coupling elements were determined. Then, the relationship between the thickness of the sample and the laser energy was found. (3) Select laser parameters for the sample and drum brake used in subsequent experiments to prepare high-quality structural coupling element units with the same eigenvalues.

3.2 The relationship between laser energy and sample thickness

3.2.1 Results of different thickness samples processed by the same laser energy

Laser bionic coupling treatment on the surface of grey cast iron related research in recent years has achieved fruitful results. However, this study aims to truck drum brake surface preparation of the unit to increase its service life, directly in the laboratory research of laser parameters used in processing the surface of the drum brake in theory is unable to get the same unit. This is due to the thin wall thickness of the sample used in the laboratory, but the wall thickness of the drum brake can reach 18mm. To verify this hypothesis, five samples with thicknesses of 6mm, 9mm, 12mm, 15mm and 18mm were prepared. To test this hypothesis, five samples with thicknesses of 6mm, 9mm, 12mm, 15mm and 18mm were prepared. Referring to the laser energy used in the relevant literature mentioned above, combined with the pulse laser parameter setting range used in this study, the same laser processing parameters (Current 135A, pulse width 6ms, frequency 4Hz, scanning speed 1.2mm/s, defocus

amount 9.8mm) were used to prepare the coupling bionic unit on the surface of samples with different thickness, and the section of the unit is shown in Fig. 3.1. It is found that the depth of the unit decreases gradually with the increase of the thickness of the sample, and there are pores and cracks in the section. Fig. 3.2 shows the surface ratio diagram of the samples with different thicknesses processed by the same laser parameters. It is observed that the width of the unit is basically the same, and there are a certain number of pores and cracks on the surface of all units. The reason for such pore defects is that the gas generated or involved in laser processing cannot escape completely during the rapid cooling and solidification process of the molten pool. The gas generated is from the reaction between carbon and oxygen in the molten pool, or the reactive pores formed after the reduction of metal oxides [205]. In addition, due to the good thermal conductivity of grey cast iron, the temperature gradient between the melting area and the matrix is too large during the cooling process, resulting in internal stress in the melting area, especially in the stress concentration areas such as pores and the surface of the unit, cracks are easy to occur. The laser parameters optimized in the laboratory to obtain high-quality units cannot be directly applied to the surface of the truck drum brake, so it is necessary to find out the relationship between samples with different thicknesses and laser energy. To prepare the same high-quality unit on the surface of the truck drum brake, it is necessary to study the different generation mechanisms of sample unit with different thicknesses and find the influence law of sample thickness on laser melting area, to optimize the high-quality unit suitable for processing on the working surface of the truck drum brake.

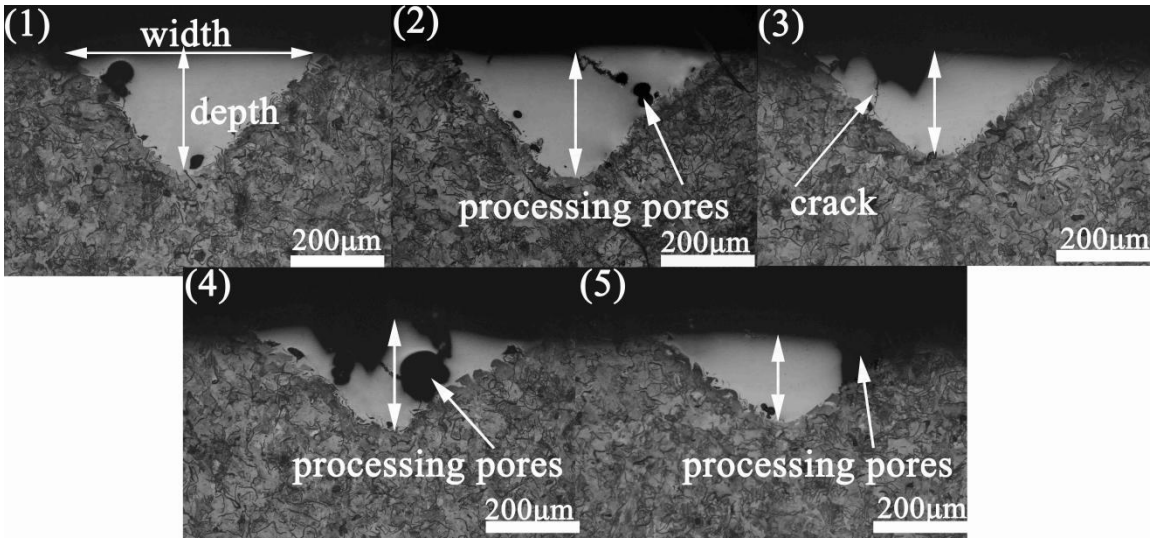


Fig.3.1 The cross-section comparison diagram of different thickness samples processed with the same laser parameters: (1), 6mm; (2), 9mm; (3), 12mm; (4), 15mm; (5), 18mm

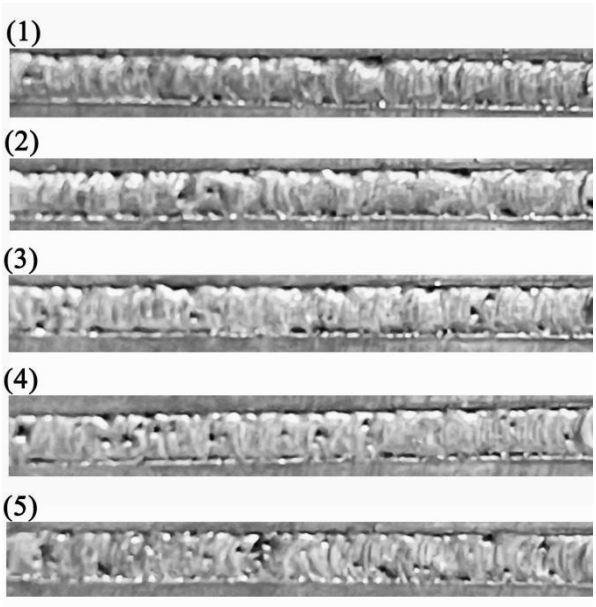


Fig.3.2 The surface comparison diagram of different thickness samples processed with the same laser parameters: (1), 6mm; (2), 9mm; (3), 12mm; (4), 15mm; (5), 18mm

3.2.2 Temperature field simulation of samples with different thickness processed by the same laser energy

In this chapter, to find out the relationship between the pulse laser with the same parameters and the samples with different thicknesses, Ansys finite element analysis software is used to simulate the temperature distribution in the unit region. The heat transfer equation of laser-processed grey cast iron is:

$$\rho c\frac{\partial T}{\partial t}=\frac{\partial}{\partial x}\left[k\frac{\partial T}{\partial x}\right]+\frac{\partial}{\partial y}\left[k\frac{\partial T}{\partial y}\right]+\frac{\partial}{\partial z}\left[k\frac{\partial T}{\partial z}\right]+\rho Q \quad (3.1)$$

$\frac{\partial T}{\partial x}$, $\frac{\partial T}{\partial y}$, $\frac{\partial T}{\partial z}$ are the temperature gradients in the x, y and z directions, k is the thermal conductivity of grey cast iron, C is the specific heat capacity of grey cast iron, ρ is the density of grey cast iron, T is the temperature, t is the time, Q is the intensity of internal heat source.

The five samples with different thicknesses in this chapter are 6mm, 9mm, 12mm, 15mm, and 18mm in the same order as above. First, when setting material properties, the thermal physical parameters of grey cast iron will change with the temperature variation. Table 3.1, Table 3.2 and Table 3.3 show the density, thermal conductivity, and specific heat capacity of grey cast iron at different temperatures. The meshing method of the model has been given in the previous chapter. The heat source is a semicircular area with a diameter of 1mm, and the room temperature is 22℃. The power density of the laser irradiation area is 142.6 W/mm^2 by calculating the laser parameters used above, and the heating time is set as 1 second. The convection heat transfer between the other surfaces and the air is achieved with a convection

coefficient of 0.00001 W/mm^2°C. The ambient temperature was 22°C at room temperature, and the temperature distribution of the cross-section was observed for 1 second. The 3D model and temperature field results of the sample are as follows.

Table 3.1 Density of grey cast iron at different temperatures

Temperature (C)	Density (kg m^-3)
25	7880
1500	7300
1600	7000

Table 3.2 The thermal conductivity of grey cast iron at different temperatures

Temperature (C)	Thermal Conductivity (W m^-1 C^-1)
25	80
200	63.6
400	50.2
769	30.9
800	29.7
1000	29.3
1500	13.4

Table 3.3 The specific heat of grey cast iron at different temperatures

Temperature (C)	Specific Heat (J kg^-1 C^-1)

25	447.688
200	518.816
400	606.68
769	1497.872
800	962.32
1000	619.232
1500	753.12

Fig.3.3-3.7 show the simulation results of samples with different thicknesses processed by the same laser parameters, which consists of three parts: the three-dimensional model of the sample, the temperature distribution of the cross-section of the unit, and the temperature distribution of the longitudinal path. For more direct comparison results, the lower limit of temperature in the red area in the legend is set as 1400℃, and the upper limit is not capped. This area is the laser melted zone by default. The temperature range of the orange area is 800℃-1400℃, which is the heat affected zone, that is, the transformed zone. Due to the depth of the cross section is one of the key factors to determine the unit quality, therefore chose to laser machining surface to the top, down in the direction of the unit cross section 3mm to draw a path, simulate the temperature gradient of this path at the same time, according to determine the length of the different regions of different thickness of the sample using the same laser processing parameters are studied.

Fig.3.3 is the schematic diagram of the simulation results of the sample with a

thickness of 6mm, that is, the sample used in the laboratory. It can be seen from the figure that the size of the sample is 40×20×6 mm^3, the red area is the melted zone, the orange area is the transformed zone, and the temperature decreases step by step. The maximum temperature of the whole cross-section if 2429.2℃, the longitudinal path length of the melted zone is 0.11328mm, and the total length of the melted zone plus the transformed zone is 0.42058mm. It can be seen from Fig.3.4 that the size of the sample is 40×20×9 mm^3, the highest temperature of the whole cross-section is 2382.9℃, the longitudinal path length of the melted zone is 0.10439mm, and the total length of the melted zone plus transformed zone is 0.4145mm. Fig.3.5 shows that the size of the sample is 40×20×12 mm^3, the maximum temperature of the whole cross-section if 2424.7℃, the longitudinal path length of the melted zone is 0.07903mm, and the total length of the melted zone plus transformed zone is 0.38609mm. It can be seen from Fig.3.6 that the size of the sample is 40×20×15 mm^3, the highest temperature of the whole cross-section is 2316.1℃, the longitudinal path length of the melted zone is 0.05613mm, and the total length of the melted zone plus transformed zone is 0.43712mm. Fig.3.7 shows that the size of the sample is 40×20×18 mm^3, the maximum temperature of the whole cross-section if 2295.8℃, the longitudinal path length of the melted zone is 0.05039mm, and the total length of the melted zone plus transformed zone is 0.36726mm. The results of longitudinal length are shown in Table 3.4.

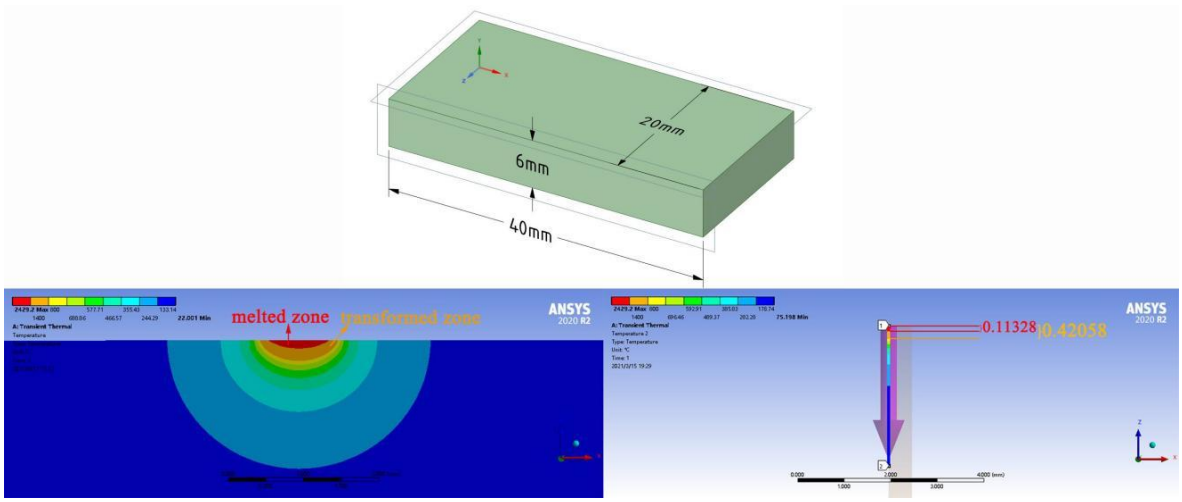


Fig.3.3 Temperature distribution diagram of heat source cross section of 6mm sample

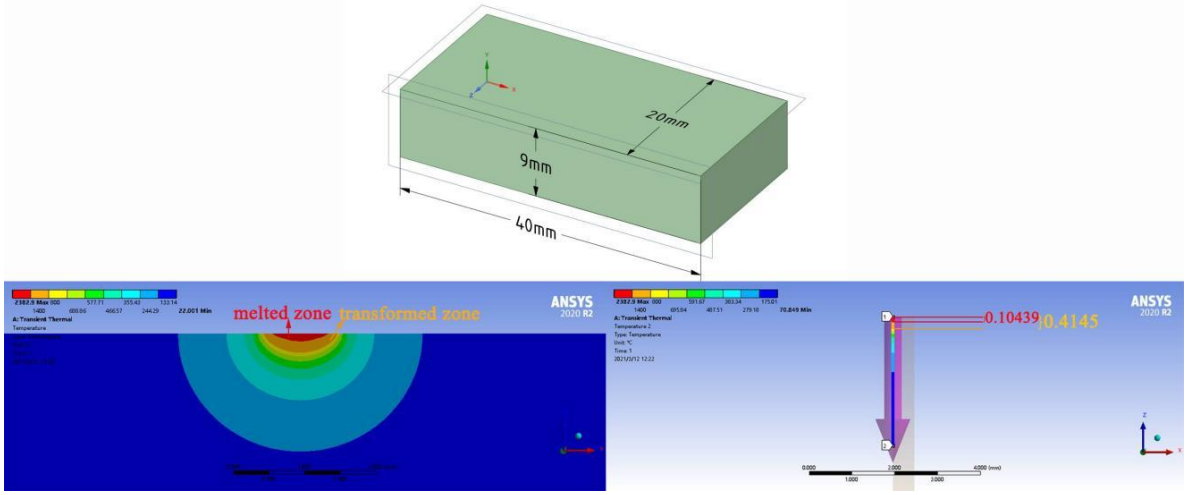


Fig.3.4 Temperature distribution diagram of heat source cross section of 9mm sample

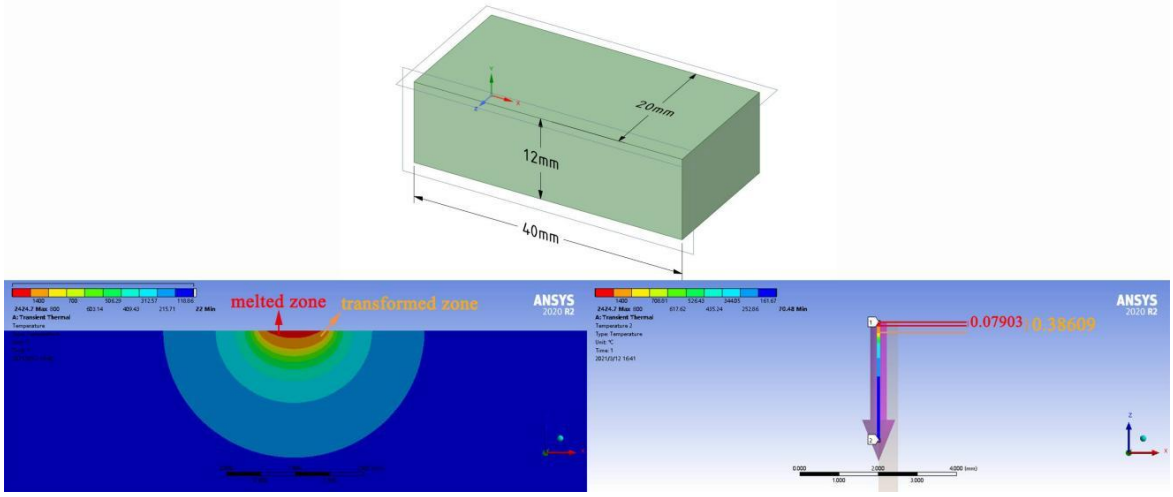


Fig.3.5 Temperature distribution diagram of heat source cross section of 12mm sample

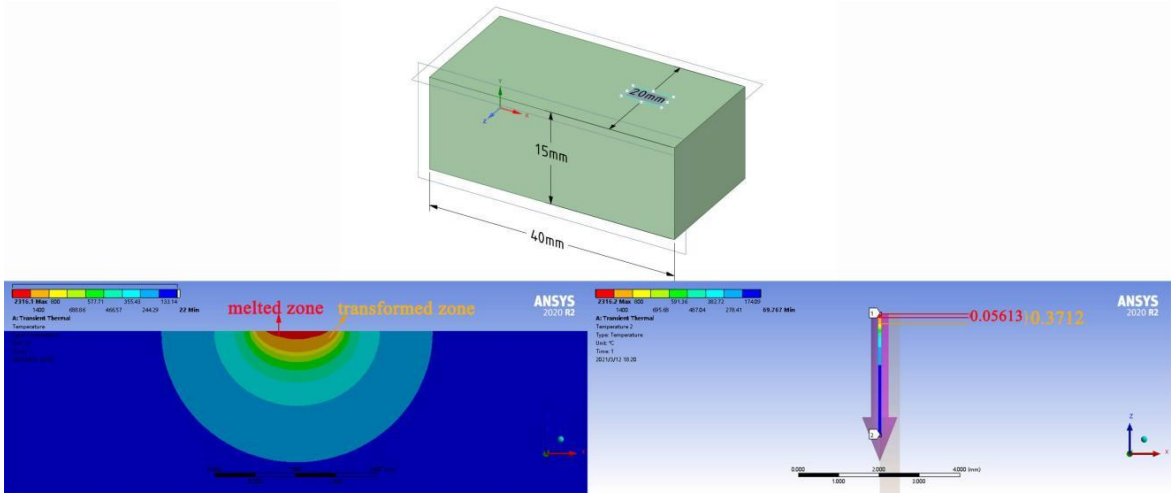


Fig.3.6 Temperature distribution diagram of heat source cross section of 15mm sample

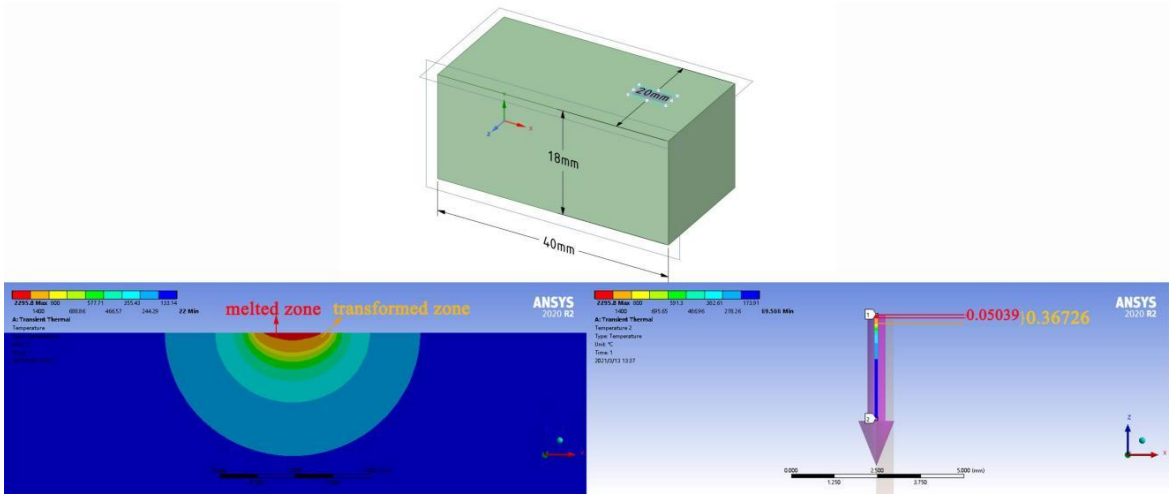


Fig.3.7 Temperature distribution diagram of heat source cross section of 18mm sample

Table 3.4 The longitudinal length of different thickness samples

Sample's Thickness(mm)	Melted Zone Longitudinal Length(mm)	Transformed Zone Longitudinal Length(mm)
6	0.11328	0.42058
9	0.10439	0.4145
12	0.07903	0.38609
15	0.05613	0.3712
18	0.05039	0.36726

According to the above simulation results, it can be concluded that the thicker the sample is, the shorter the longitudinal length of the laser melted zone is, and the shorter the total length of the melted zone plus transformed zone is. When the thickness of the sample is relatively thin, the laser heat absorbed on the surface can quickly spread to the interior and even to the lower surface. The heat diffusion rate to the air is much lower than that inside the metal, and the heat accumulates inside the sample. In the process of heat transfer, the bottom surface is equivalent to a thermal resistance layer [206, 207], which will reduce the heat dissipation and heat conduction rate. On the contrary, for thick samples, grey cast iron has good thermal conductivity, and the distance between the top heat source and the bottom is large, so the heat can diverge relatively quickly. Therefore, the thicker the sample is, the shorter the longitudinal length of the cross- section of the melted zone and transformed zone is.

In addition, the simulation results of temperature field can be explained by the different heat capacities of samples with different thickness along the heat transfer path. The larger the thickness of the sample wall, the larger the heat capacity. Since the heat transfer problem of laser melting belongs to the category of transient thermal analysis, the thermal impedance of the sample with different thicknesses in the longitudinal path (0-0.5mm) was calculated, as shown in Fig.3.8. The formula of thermal impedance: $Zth = \Delta T/Q$. It can be found in the figure that the thermal impedance of 6mm sample is the largest, and the thicker the sample is, the smaller the thermal impedance is. On the same path, the temperature difference of 18mm thickness sample is the largest. Therefore, when the same laser parameters are used to process samples of different thicknesses, the unit on the surface of the thicker sample has poor quality, precisely because of the large temperature gradient and fast cooling speed. As a result, the gas generated or involved in the laser treatment process is too late to completely overflow the molten pool, and the internal stress is too large to exceed the strength limit of the material, resulting in cracks.

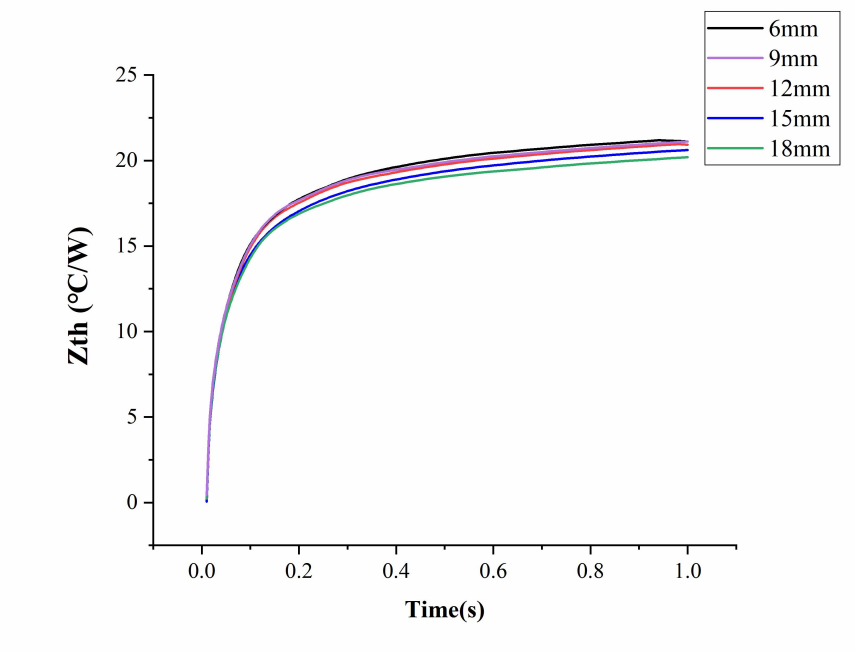


Fig.3.8 Thermal impedance of different thickness samples

3.2.3 Transfer law of laser energy in samples with different thickness

Cross section of the highest single point temperature can be as a reference but not according to this value for effective contrast, Fig.3.9 is the scatter diagram of the temperature distribution of five samples with different thicknesses in the longitudinal cross-section. By observing the scatter distribution, it can be seen that the temperature gradient of all samples decreases rapidly from the high temperature of more than 2000 degrees. This is because grey iron has good thermal conductivity and fast heat transfer speed, and the temperature of 18mm thick samples at each position are the lowest. The thicker the sample, the lower the temperature at each point. Because of this, there is a large gap between the unit processed on the surface of the sample and the drum brake using the same laser parameters. According to Fig.3.9, the following equation

can be fitted for the transfer law of the same laser energy in samples with different thicknesses:

$$y_1 = (905.7 \pm 12.7)x^2 + (-2436 \pm 25.5)x + (1664 \pm 10.6) \quad (3.2)$$

$$y_2 = (889.3 \pm 12.3)x^2 + (-2396 \pm 24.7)x + (1640 \pm 10.3) \quad (3.3)$$

$$y_3 = (893.5 \pm 14.3)x^2 + (-2369 \pm 28.7)x + (1581 \pm 12.4) \quad (3.4)$$

$$y_4 = (853.1 \pm 13.4)x^2 + (-2268 \pm 26.8)x + (1524 \pm 11.2) \quad (3.5)$$

$$y_5 = (844.2 \pm 13.2)x^2 + (-2246 \pm 26.6)x + (1511 \pm 11.1) \quad (3.6)$$

Where x value is the longitudinal length of the laser processing cross-section with the top as the origin, y is the temperature value of laser processing for 1 second, and the coefficient of determination R^2 value is 0.94,0.95,0.90,0.91,0.91, respectively.

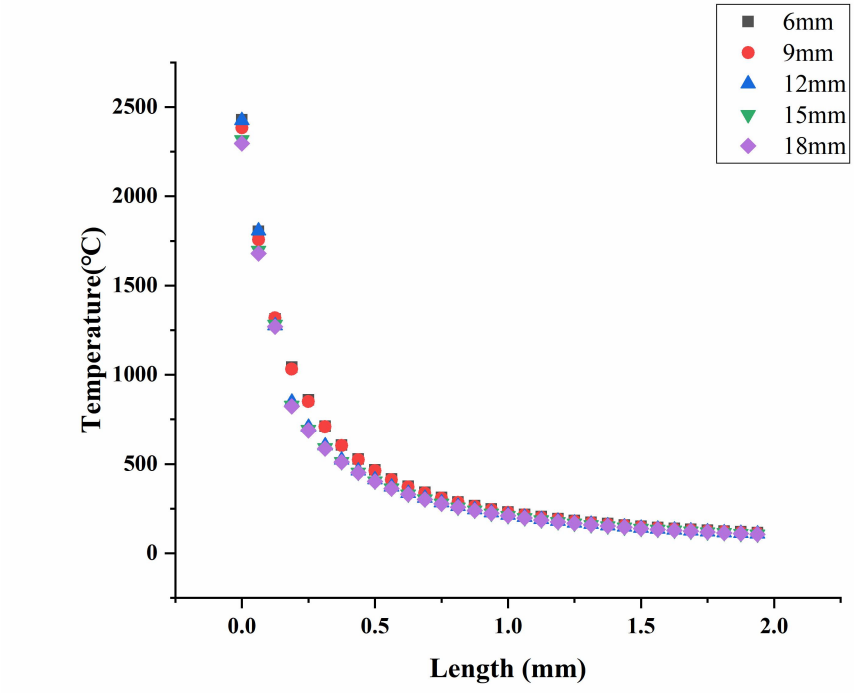


Fig.3.9 Longitudinal temperature distribution of cross sections of samples with different thicknesses

3.3 Parameter optimization of structural coupling unit of grey cast truck drum brake prepared by laser

The above research results confirm that the laser processing parameters used to fabricate high-quality units on the surface of laboratory samples cannot be directly transplanted to the drum brake. The research object of this study is the truck drum brake, so it is necessary to process high-quality units in the working face of a truck drum brake. There are a huge number of combinations of the five laser parameters within the range that can be set by the machine, and it is impossible and unreasonable to try every combination. Therefore, the scientific optimization method can not only reduce the workload reasonably but also effectively improve the experimental efficiency and accurately find the appropriate parameters. In the past 90 years, experimental design methods have been widely developed and applied, especially in the actual industrial production and design, which plays an important role, mainly reflected in reducing the experimental cost, greatly shortening the test cycle and reasonably increasing the yield [208]. In this research, to select the best combination of laser parameters and explore the influence of laser parameters on the preparation of coupling bionic unit, the orthogonal test method was used to determine the laser parameters of the coupling unit of the truck drum brake. In addition, because the laser equipment is different, the same laser parameters may not be able to process the same unit, so the simple adjustment of laser processing parameters cannot be applied to the actual production task. To provide help for the practical application of laser coupling

bionic treatment of truck drum brakes in the future, it is necessary to find out the relationship between laser processing energy and different thickness of the sample.

3.3.1 Design and result analysis of orthogonal test

Since the preparation of the unit is completely affected by the five laser parameters, it is unreasonable to try different combinations successively. For complex experiments with multiple factors and exploratory properties, orthogonal test design can obtain the best process parameters through relatively few tests. In this research, combining with the parameter range of the laser that can be set, and referring to the laser parameters used in the above, a three-factor and three-level orthogonal test scheme is designed. The unit is prepared by laser on the surface of the sample with 18mm thickness, and the results are observed and analyzed. For the safety of laboratory experiments, the laser scanning speed controlled by the manipulator was locked at 1.2mm/s, and the defocus was set at 9.8mm. Then the orthogonal test scheme is designed for the other three laser parameters. The orthogonal table and results are shown below.

The orthogonal scheme is shown in Table 3.5, and the results are shown in Table 3.6, Fig.3.10, and 3.11. The No. in the table corresponds one-to-one with the label in the figure. Combined with the table and figure, it can be seen that the cross sections of most units are U-shaped, and the depth-width ratio is increased compared with the units in the previous text, mainly because of the increase of current, pulse width and frequency, and the enhancement of laser energy. The number of pores and cracks in the unit is small, among which the number of pores and cracks in the No.6 unit is the

least, and the depth-width ratio reaches 0.722. The surface of the unit is smoother and has no obvious defects compared with other units. Therefore, the optimal laser processing parameters can be obtained as follows: current 140A, pulse width 8ms, frequency 4Hz, scanning speed 1.2mm/s, defocus 9.8mm.

Table 3.5 The orthogonal test design

No.	A current (A)	B pulse width (ms)	C frequency (Hz)
1	135	6	4
2	135	7	5
3	135	8	6
4	140	6	5
5	140	7	6
6	140	8	4
7	145	6	6
8	145	7	4
9	145	8	5

Table 3.6 The results of orthogonal test

No.	Depth-to width ratio	Number of surface pores	Number of surface cracks
1	0.392	9	2
2	0.723	6	6

3	0.684	7	7
4	0.554	8	7
5	0.671	4	5
6	0.722	2	1
7	0.635	6	2
8	0.630	3	5
9	0.634	4	2

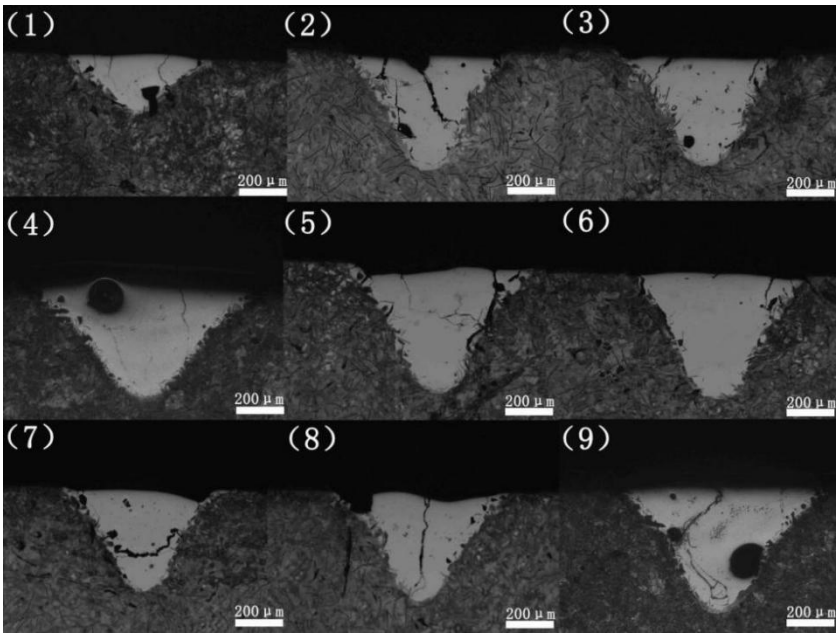


Fig.3.10 Cross section comparison of coupling bionic units in orthogonal test

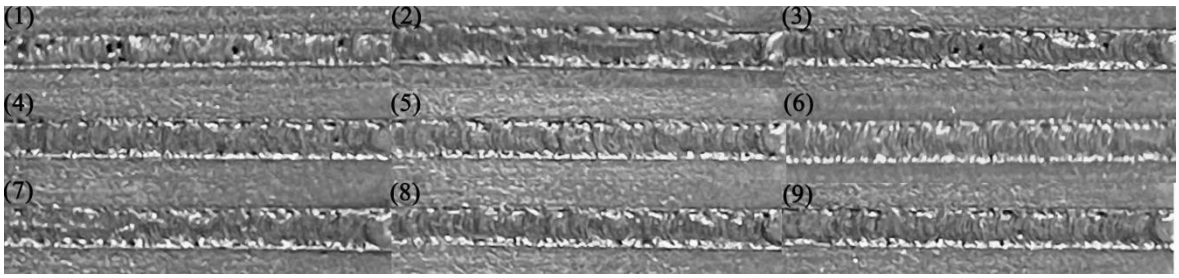


Fig.3.11 Surface comparison of coupling bionic units in orthogonal test

3.3.2 Relationship between laser processing energy and sample thickness

The laser parameters suitable for machining truck drum brakes are obtained by orthogonal test. However, there are many kinds of laser equipment on the market, so it is impossible to obtain the same quality units with different lasers with laser processing parameters as a reference. In order to make the research results from basic theoretical research to practical application, to provide an effective reference for actual production, this chapter embarks on the results in previous research, the finite element simulation (as shown in Fig3.12), by adjusting the laser power density makes the different thickness of the sample the melted zone and transformed zone in the longitudinal length of basically the same.

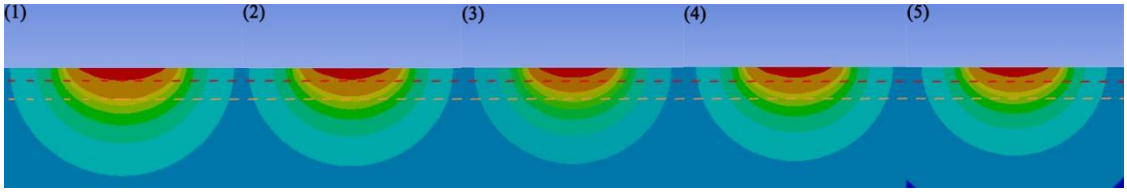


Fig.3.12 Simulation results of unit temperature field

In this way, it can not only avoid the restriction on the processing of the unit by determining the parameters but also make the actual processed unit basically guarantee the depth-width ratio and U-shape according to the law obtained from the orthogonal test above. Then, the number of pores and cracks can be controlled by adjusting the current and pulse width within a very small parameter range. Finally, high-quality units with the same surface as the samples used in the laboratory were

obtained. The following equation is fitted to the relationship between laser processing energy and samples with different thicknesses:

$$y = 138.6 \pm 0.46 + (0.667 \pm 0.037)x \quad (3.7)$$

Where x is the thickness of the sample, y is the corresponding laser power density, and the coefficient of determination R^2 of the equation is 0.99, showing a good degree of the fitting. The thickness of the sample is positively proportional to the laser processing energy. The thicker the sample is, the greater the laser energy required. The higher the energy is, the higher the surface temperature of the laser heat source. This is also in line with the conclusion of the numerical simulation above. The wall thickness of the drum brake in this research is 18mm. According to Equation 3.7, it can be calculated that the laser power density required for the drum brake in this study is 150.8W/mm^2.

3.4 Laser fabrication of structural coupling units

Through the optimal laser parameter combination designed by the orthogonal test scheme described above, that is, the current is 140A, pulse width is 8ms, frequency is 4Hz, scanning speed is 1.2mm/s, defocus is 9.8mm, high-quality coupling bionic unit can be prepared. Using Ansys to simulate for laser processing areas in the region can be divided into the melted zone and the transformed zone. Fig.3.13 is the schematic diagram of different areas of the unit. The left side is the picture taken by optical microscope. The white area in the picture is the unit, that is, the laser melted area. Electron microscopy (SEM) picture is on the right and fused visible area due to the

degree of supercooling is very big, the speed of the nucleation rate is greater than the crystal nucleus growth, thus obtained the microstructure of ultrafine, in the middle of the melted zone and substrate have a phase transition area, this area is in the process of laser processing temperature near the melting point of grey cast iron, around the melted zone is equivalent to the solid-state phase transformation, This region is therefore called the transformed zone, where the austenization process is very rapid and part of the graphite dissolves [209] .

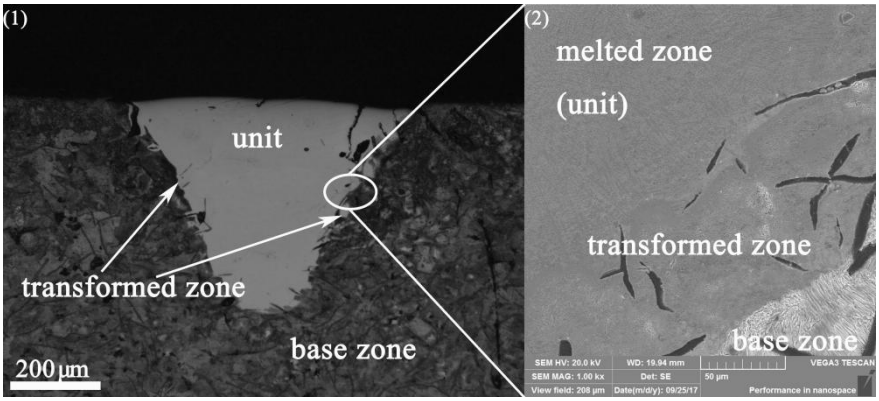


Fig.3.13 Microstructure of different regions of the unit

Then the phase analysis is carried out on the drum brake working surface and the processing area. The X-ray diffraction results are shown in Fig.3.14. According to the result of diffraction peak calibration, the matrix is mainly ferrite and graphite. After laser processing, the peak width corresponding to the proferrite become wider. Residual austenite and martensite were found after calibration. It is the appearance of a new phase that increases the microhardness of the unit. The half-peak width of the diffraction peak is 0.298° for the base and 0.441° for the unit, which proves that the grain size or sub-grain size is refined. In addition, the Hall-patch [68] can explain the

effect of grain size on the yield strength of materials:

$$\sigma_s = \sigma_i + kd^{-1/2} \quad (3.8)$$

The σ_s represents the yield limit of the material, σ_i is the lattice friction generated when moving a single dislocation, k is constant and depends on the type of material and the size of the grain, and d represents the average grain diameter. The Hall-patch relationship shows that the performance of the unit has been improved overall after grain refinement, and it becomes hard phase in the grey cast iron base metal.

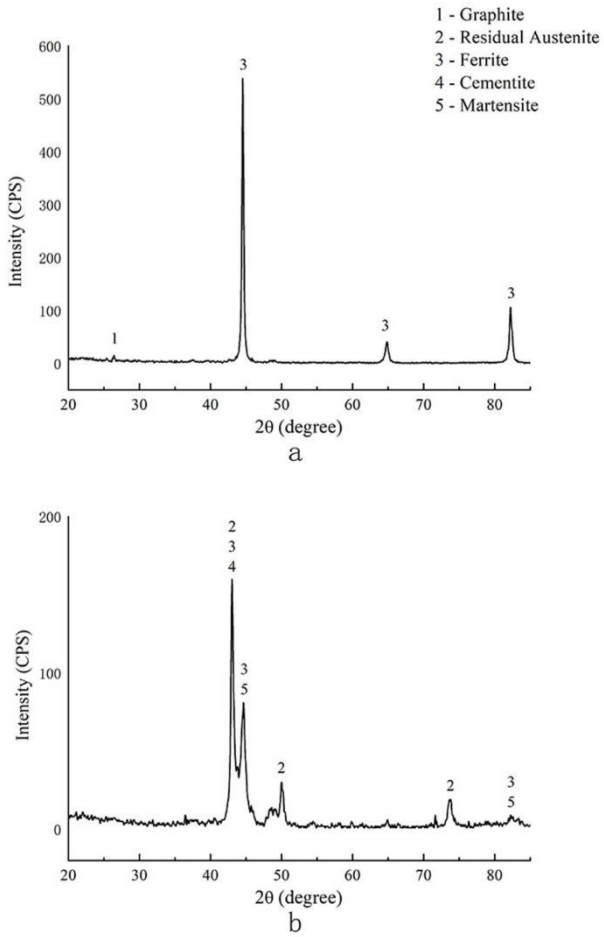


Fig.3.14 XRD analysis: a, blank sample; b, bionic sample

Fig.3.15 shows the microhardness distribution diagram of the base-unit-base of drum

brake grey cast iron. Nine points were selected along a length of 470μm from left to right in the direction of the cross-section, using a load pressure of 0.2 kg and a holding time of 10 seconds. The microhardness distribution of base-unit-base shows that the hardness values increase first, then stabilize, and finally decrease. The microhardness of the base is about 300HV, the microhardness of the transformed zone is 550HV-600HV, and the microhardness of the unit region is 660HV-720HV. The results of microhardness are corresponding to the above electron microscope pictures and XRD results, which prove that the unit has finer microstructures and higher microhardness values than the base.

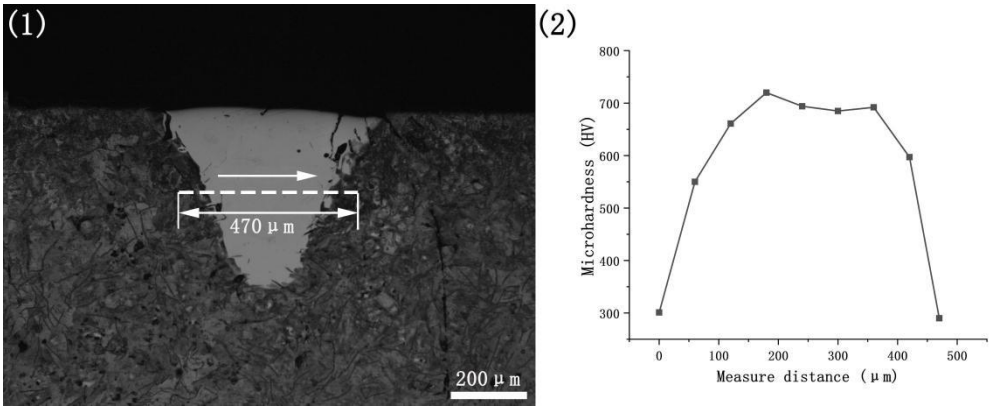


Fig.3.15 Hardness distribution diagram of base and unit

3.5 Chapter summary

The main work of this chapter is the optimization of the parameters of the structural coupling unit of the grey iron truck drum brake. Appropriate laser processing parameters are the premise of preparing the high-quality structural coupling unit. In order to select the laser processing parameters, this chapter has done the following

work and drawn the following conclusions:

(1) The same laser parameters were used to process the samples with different thickness. The thicker the samples were, the worse the quality of the coupling units was. Ansys numerical simulation software was used to simulate the temperature distribution of five samples with different thickness under the actual working conditions. It was found that the thicker the samples were, the shorter the longitudinal length of the laser melted zone and the transformed zone was. For the temperature at the same position in the cross section, the thicker the sample, the lower the temperature.

(2) By designing the orthogonal test scheme, the high-quality unit with the least number of pores and cracks and the ratio of depth to width of 0.722 is finally obtained, which is suitable for the truck drum brake working surface. The laser processing parameters are determined as 140A current, 8ms pulse width, 4Hz frequency, 1.2mm/s scanning speed and 9.8mm defocus.

(3) By increasing the laser power density, the same cross-section length of melted region and transformed region can be simulated for samples with different thickness, and the relation equation between laser processing energy and samples with different thickness is fitted, which provides a reference for the laser coupling bionic processing and production of truck drum brake.

(4) After laser irradiation, graphite is completely dissolved on the surface of grey cast iron drum brake. Due to the rapid cooling rate, the superfine structure composed of cementite, martensite and residual austenite is formed in the melted area. In the

transformed zone between the melted zone and the base zone, the graphite is not completely dissolved, and the temperature does not reach the melting point of grey cast iron. The microhardness of melted zone is 133% higher than that of the base, and the microhardness of transformed zone is 90% higher than that of the base.

Chapter 4: Influence and Analysis of Base Metal Coupling Element on Thermal Fatigue and Wear Resistance of Bionic Grey Cast Iron Truck Drum Brake

4.1 Introduction

By optimizing the laser processing parameters, a high-quality coupling bionic unit can be prepared on the surface of grey cast iron truck drum brake. However, the composition and organization of grey cast iron produced by different manufacturers and different batches on the market are different, which is due to the different chemical composition in the casting process or the difference in solidification mode, leading to the change in the performance and characteristics of grey cast iron. When the composition and structure of grey cast iron are different, the cooling rate of the melted area will be different due to the different base materials in the laser coupling bionic treatment, which means that the thermal fatigue resistance and wear resistance of the coupling bionic unit will be significantly affected. In order to compare the influence of the change of the base material itself on the thermal fatigue resistance and wear resistance of the coupling bionic drum brake, and to compare the differences between the coupling elements of different base materials, in this chapter, according to the characteristics of grey cast iron, combined with the current research hotspots on grey cast iron, different graphite types, different carbon content and different pearlite content and interlamellar spacing as the research object, design and preparation of different graphite types and different carbon content as auxiliary materials, samples

with different pearlite content and interlamellar spacing were obtained from the drum brake, using laser on the surface preparation, coupling bionic design will be processed into anti-crack ring+ 45° angle mesh model and study different base metal coupling element on the microstructure and mechanical properties of the unit the influence law of the contrast before and after different grey cast iron by bionic coupling laser processing the results of thermal fatigue and wear resistance, focused on analysis of grey cast iron graphite type, The different responses of carbon content, pearlite content and distance to thermal fatigue and wear resistance of grey cast iron before and after laser treatment provide theoretical support and reference for the selection of grey cast iron base metal in practical production and the practical application of laser coupling bionic technology.

4.2 Influence and analysis of graphite type on thermal fatigue and wear resistance of coupling bionic samples

Grey cast iron performance can play a significant impact on the number of graphite in grey cast iron, shape and distribution, and graphite itself will be due to different casting process and different chemical composition of the composition of different graphite types, so the first need to explore different graphite types of grey cast iron thermal fatigue and wear resistance. The application of laser coupling bionic technology has been proved to greatly improve the thermal fatigue and wear resistance of materials [168, 210, 211]. The influence of different graphite types of grey cast iron on the coupling bionic unit needs to be further studied. Finally, the

influence of different graphite types on the thermal fatigue and wear resistance of blank samples and coupling bionic samples is compared.

4.2.1 Different graphite types of grey cast iron

Fig.4.1 shows the SEM images of five types of graphite. According to the BSI EN ISO945-1:2008 standard document of metallography, the figure is in turn type A graphite, length grade 3, flake graphite, pearlite and a small amount of ferrite can be seen; Type B graphite, length grade 3, rosette distribution graphite; Type C graphite, length grade 2, thick sheet graphite; Type D graphite, after deep corrosion, is found to be composed of a large number of fibrous graphite clumps distributed in the dendrite gap, length grade 8; Type E graphite, small flake graphite, a small amount of ferrite and pearlite, length grade 4. The different graphite types can be formed because of the different casting methods used and the different carbon equivalents. Type A graphite and type C graphite are cast by wet sand method, due to the different carbon equivalent leads to the formation of different types of graphite, and because of the use of the cooling rate of very fast metal casting method, the supercooling degree of molten iron is great, so the formation of D-type graphite. Chemical composition is shown in Table 2.2 above.

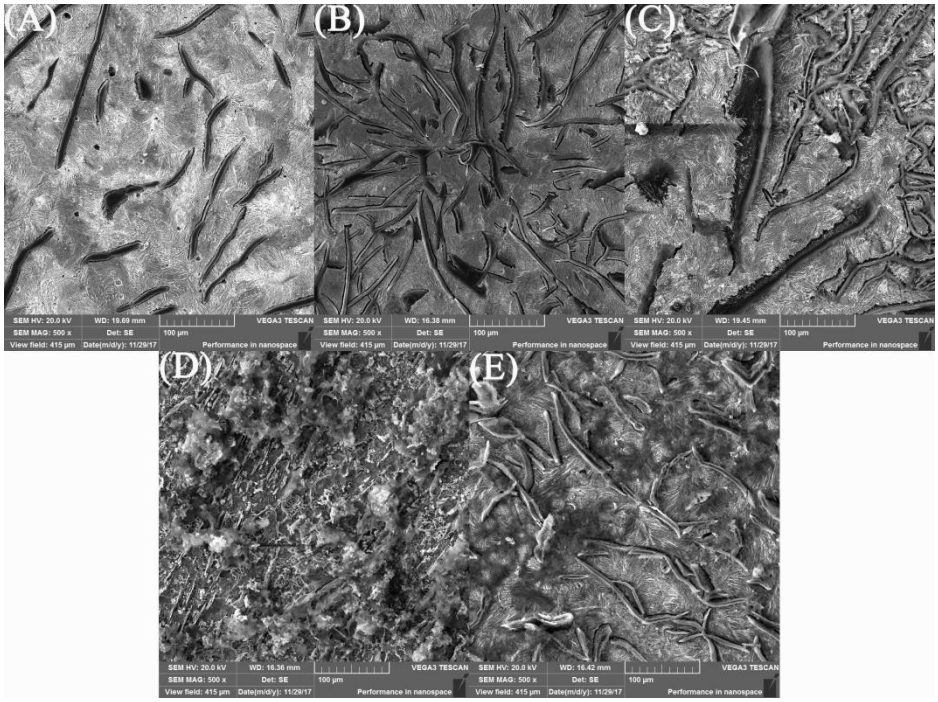


Fig.4.1 Different graphite types of grey cast iron: (A), type A graphite; (B), type B graphite; (C), type C graphite; (D), type D graphite; (E), type E graphite

4.2.2 Microstructure analysis of different graphite samples

The reason why the strength and hardness of the coupling bionic unit is much higher than that of the grey cast iron base metal is that the grey cast iron is rapidly cooled in the melted zone after laser irradiation, the graphite is completely dissolved, and the solid solution is strengthened after the solid solution in the melted zone. Fig.4.2 is a histogram of microhardness comparison between different graphite types of base and unit. According to the information given in the figure, the unit hardness of all the different graphite types is much greater than the microhardness of the base, which increases by 151%, 188%, 145%, 199% and 47% in turn, and the microhardness of D-type graphite increases the most. The properties of materials are more determined

by their own microstructure. For grey cast iron base metal, graphite, pearlite and ferrite are the main components.

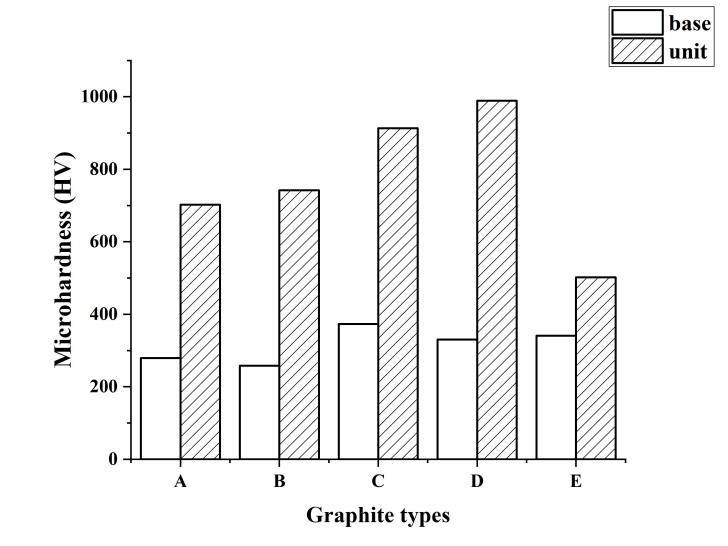


Fig.4.2 Microhardness of base and unit

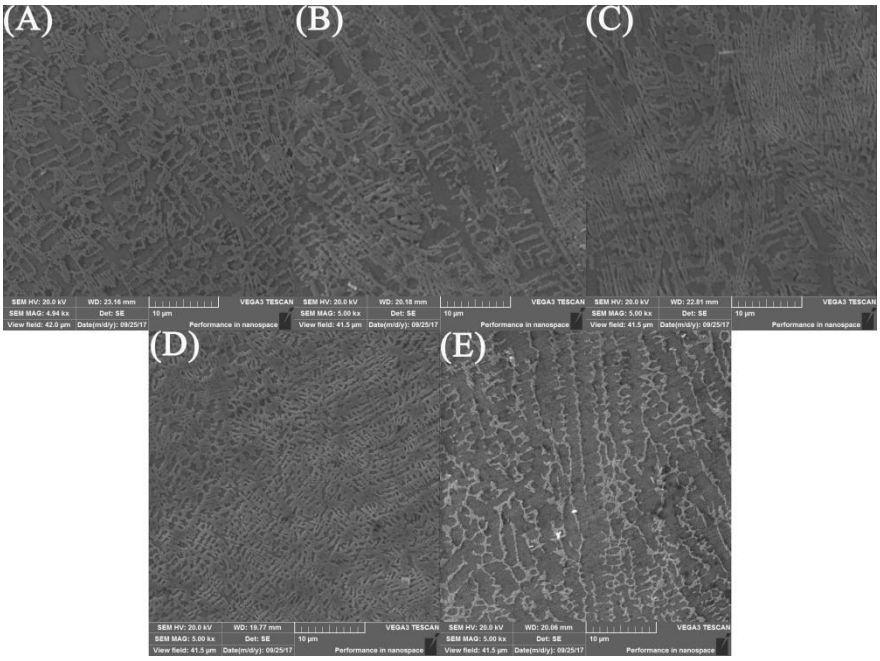


Fig.4.3 Microstructure of different graphite types units: (A), type A graphite; (B), type B graphite; (C), type C graphite; (D), type D graphite; (E), type E graphite

The thermal conductivity of grey cast iron is affected by the carbon content and graphite type. The coupling bionic unit prepared by laser processing is also affected by the carbon content and graphite type of grey cast iron, which determines the morphology and distribution of carbides in the unit. Fig.4.3 is the scanning electron microscope images of grey cast iron units of different graphite types prepared by laser. It can be seen from the figure that the dendrites of type A graphite and type D graphite unit are grid shaped, the dendrites of type A graphite unit are coarse-grained, and the dendrites of type D graphite unit are finer. The carbon content of type B graphite and type C graphite is higher, and the distribution of graphite is not uniform, so the distribution of dendrites of the unit is not uniform, and the morphology is needle-like. The carbon content of type E graphite is low, and the dendrite morphology of the unit is fishbone.

4.2.3 Effects of graphite type on microthermal fatigue crack

Thermal fatigue crack is the main cause of drum brake failure [212]. During braking, the temperature of the working surface of the drum brake rises sharply. Due to the good thermal conductivity of the cast iron itself and the air cooling and heat dissipation in the process of vehicle driving the temperature of the working surface of the drum brake drops rapidly. Under the action of thermal stress and thermal strain, the surface stress of grey cast iron is easy to concentrate at the defect, and the defect becomes the site of thermal fatigue crack nucleation [213]. Continuous thermal

expansion and contraction process, and through the accumulation of a certain number of thermal cycles, causing stress concentration at the tip of graphite, thermal fatigue crack initiation. EDS was used to analyze the elemental composition of the crack source, as shown in Fig.4.4. The cracks in the figure are initiated from two graphite tips after 20 cycles of thermal fatigue and spread along grain boundaries. When microcracks sprout on the surface of the sample, the contact area with the external environment becomes larger, and it is easier to oxidize. Therefore, a large number of oxides are easily generated in the microcracks to accelerate the crack propagation and extension. According to EDS analysis, the oxide of surface grey iron is mainly distributed in the thermal fatigue crack, which proves that the stress existing in the graphite tip and the joint action of oxidation corrosion accelerate the initiation and propagation of thermal fatigue crack.

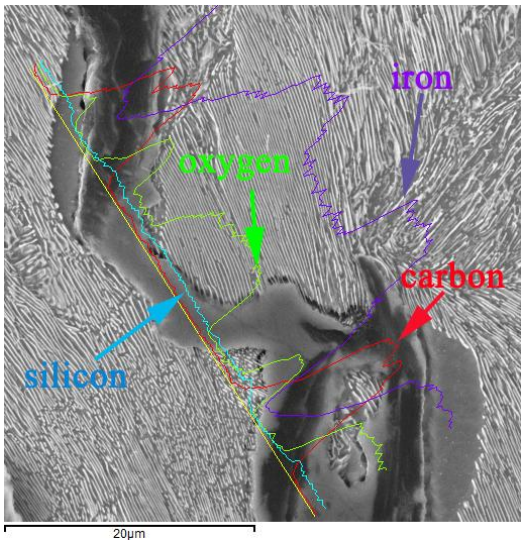


Fig.4.4 EDS analysis of crack source

Because the main position of thermal fatigue crack initiation is the tip of graphite, the

type, length and distribution of graphite in grey cast iron become the main factors affecting the internal stress concentration and thermal fatigue crack initiation. The size of the stress is proportional to the length of graphite, because the crack initiation in graphite, graphite itself is longer, the easier it is to produce cracks in the thermal cycle, but inversely proportional to the distance between two graphite, the smaller the spacing is, the easier it is to bridge, the smaller the stress required. Fig.4.5 shows the propagation modes of thermal fatigue cracks in grey cast iron with different graphite types, which are arranged in the order of graphite types A-E.

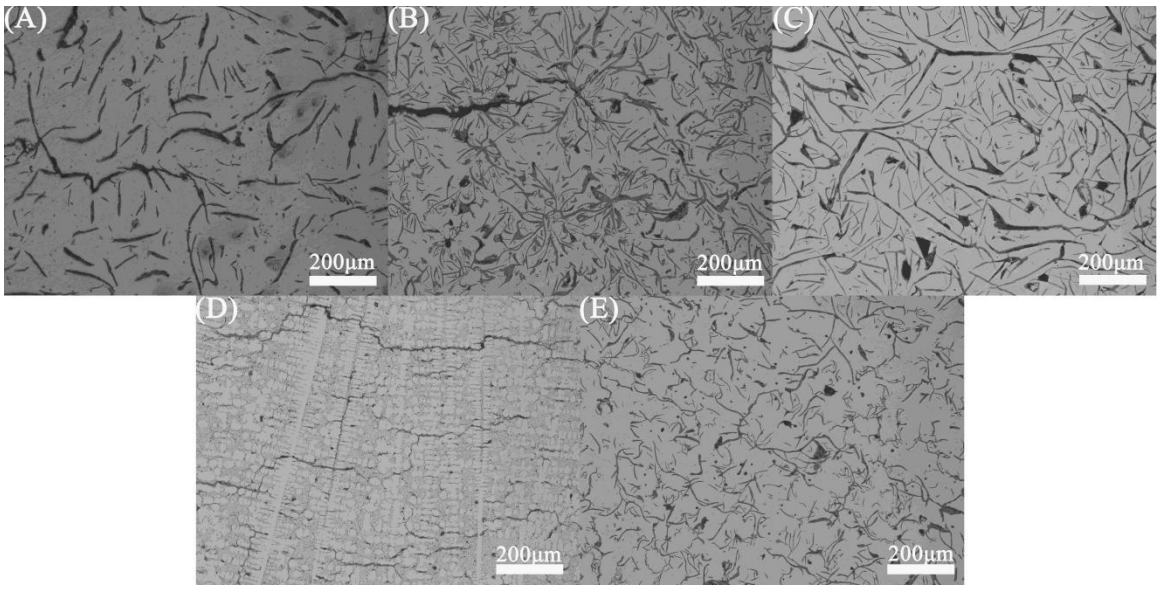


Fig.4.5 Microthermal fatigue cracks of different graphite: (A), type A graphite; (B), type B graphite; (C), type C graphite; (D), type D graphite; (E), type E graphite

The cracks shown in the figure were initiated after 20 cycles of thermal fatigue. It can be seen from the figure that the distance between two graphite of type A graphite is the largest among all samples, so the distribution of internal stress is the most uniform

after the thermal fatigue cycle. The bridging of microscopic cracks requires greater energy than other graphite samples, and the initiation and expansion of cracks are the least. Type B graphite is chrysanthemum-shaped distribution, the distribution of graphite is dense, and in all directions, the distance between graphite is relatively short, and the microscopic cracks are most easy to bridge each other with little energy, and the cracks after expansion are radial. Type C graphite is a thick sheet graphite structure, and the internal stress is the largest at the tip of type C graphite after thermal cycling. However, due to the relatively long distance between graphite, combined with Fig.4.6A, it can be seen that type C graphite has fewer cracks in the early stage of thermal fatigue test, and the sample breaks through the limitation of crack initiation after a certain thermal stress accumulates in the middle stage of test, and the number of cracks begins to grow rapidly. This is due to the higher carbon content of type C graphite, which means better thermal conductivity, thus causing the change in the growth rate of the number of cracks. The morphology of type D graphite is relatively the smallest, and the distance between graphite is relatively small, so for type D graphite after a thermal cycle, the microscopic crack only needs to extend a very short distance to bridge with other graphite. It can be seen from the figure that the crack extends along the dendrite gap to the other graphite. According to Fig.4.6A, it can be seen that the characteristics of type D graphite led to the largest number of cracks in the early stage of the thermal fatigue test, with the largest growth rate, and tends to be flat in the later stage of the test. The crack morphology of type E graphite is similar to that of type D graphite after 20 thermal cycles. This is because

the distribution characteristics of type E graphite are existing in the gap of secondary dendrite, which not only has a certain directivity but the distance between graphite is small, and the crack is easy to bridge.

It can be seen that the number of thermal fatigue cracks in grey cast iron is greatly affected by graphite type, and the number of cracks in grey cast iron with different graphite types is obviously different. According to Fig.4.6, except for type C graphite, the growth rate of the number of cracks is the fastest in the early stage of the thermal fatigue test. With the progress of the test, the degree of oxidation and decarbonization of grey cast iron is deeper, resulting in the lack of crack sources, so the growth rate of cracks slows down and gradually becomes stable. In terms of the growth rate of the number of cracks, the order of all different graphite types is type D graphite > type C graphite > type E graphite > type B graphite > type A graphite. Type A graphite has the strongest thermal fatigue resistance, while type C and D graphite have the worst thermal fatigue resistance.

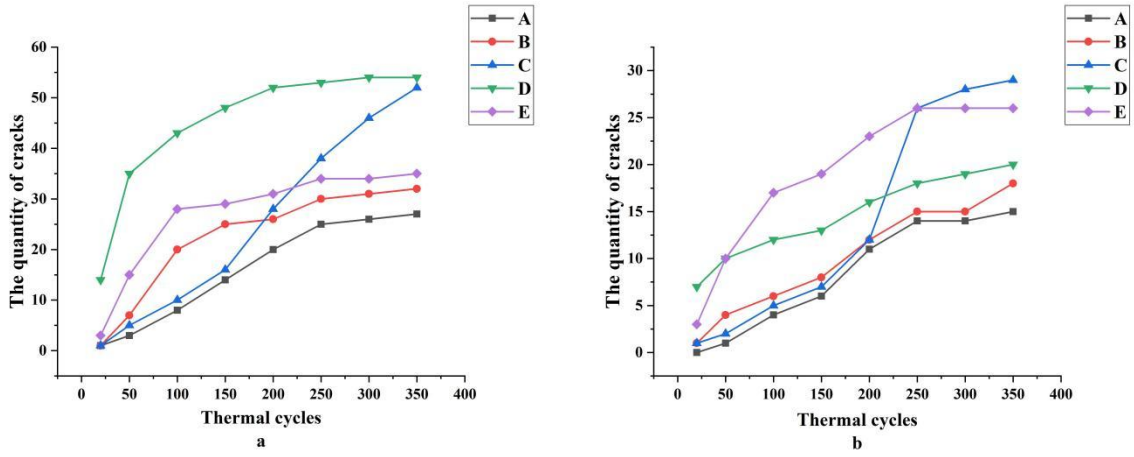


Fig.4.6 Quantity of thermal fatigue cracks of different graphite types: a, blank

samples; b, bionic samples

Fig.4.6b shows the number of thermal fatigue cracks of coupling bionic grey cast iron samples with different graphite types. Compared with 4.6A, it is found that the number of cracks of samples with coupling bionic surface in each stage of the thermal fatigue test is much smaller than that of unprocessed blank samples. Especially for type D graphite, after laser bionic treatment on the thermal fatigue resistance of the largest range of improvement, and the improvement of type C graphite is relatively minimal. The main reason is that type C graphite is thicker than other graphite types, and the length of the grade is 2; The length of type D graphite and graphite is relatively small, and the distance between the length of the level is only a magnitude 8, can more easily resist coupling bionic unit microcrack initiation, hinder the thermal fatigue crack extension, thus greatly improve the thermal fatigue resistance of the type D graphite, the thermal fatigue crack on the surface of a type C graphite inhibitory effect. In summary, it can be concluded that the smaller the graphite, the lower the length class, and the stronger the thermal fatigue resistance of the bionic samples without directionality.

4.2.4 Influence of graphite type on macroscopic thermal fatigue crack

When a certain number of thermal cycles is reached, the thermal fatigue crack will continue to expand along the transverse and longitudinal direction, and gradually become macroscopic cracks visible to the naked eye. At this time, the initiation stage

of the crack is declared to be over. At the same time, the thermal fatigue resistance of cast iron is gradually transformed into the properties of cast iron determined by the surface conditions of the material [214]. Fig. 4.7 shows the microstructure of base and unit when macroscopic cracks appear. As can be seen from the figure, when the number of thermal cycles accumulates to a certain number of times, part of the base material undergoes phase transformation, in which the pearlite content decreases significantly and is decomposed into graphite and ferrite, and the strength and hardness of the base material itself decreases rapidly. In the unit area, under the action of the hot medium, the surface of the material is oxidized seriously. As mentioned above, the surface is covered with oxides, and under the joint action of the two factors, the propagation speed of thermal fatigue crack is aggravated.

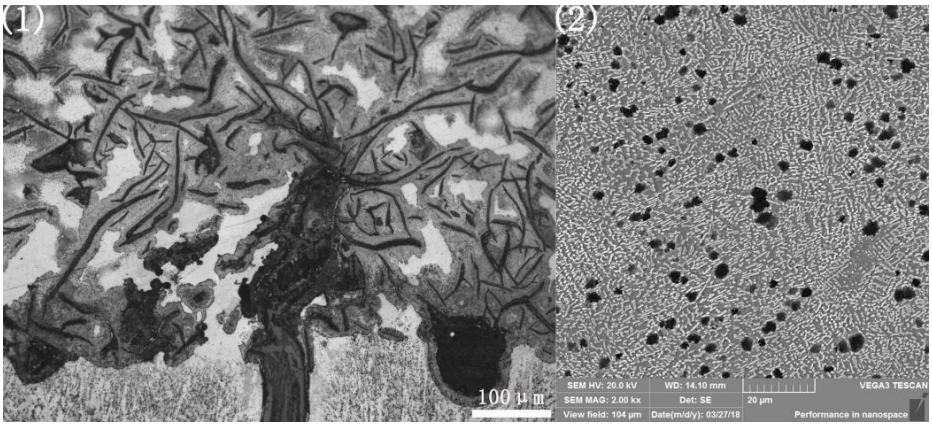


Fig.4.7 Microstructures of base and unit after 350 thermal fatigue cycles

Fig.4.8 shows a schematic diagram of macroscopic thermal fatigue crack with graphite as a bridge and continuous bridging expansion. It can be found from the picture that the growth direction of the crack is not fixed, and it will expand along

different directions at the same time. Moreover, a major thermal fatigue crack will form some small cracks connected with the surrounding graphite. Therefore, graphite has become the main factor affecting the thermal fatigue crack propagation mode, propagation speed and propagation direction. Combined with the above, it can be proved that different graphite types will directly lead to different thermal fatigue crack propagation.



Fig.4.8 Bridge propagation morphology of thermal fatigue crack

In order to compare and study the thermal fatigue resistance of blank grey cast iron samples with different graphite types and coupling bionic samples, 350 cycles of thermal fatigue tests were conducted on grey cast iron with different graphite types to observe the thermal fatigue crack morphology on the surface of the samples (see Fig.4.9). The graphite types in the figure are arranged from type A graphite to type E graphite. The upper part is the blank sample, and the lower part is the bionic sample. It can be seen from the figure that there are only a few cracks in type A graphite, and the surface of the sample is mostly holes in the position of the original graphite. Combined with Fig.4.10, it can be seen that both the blank sample and the bionic sample of type A graphite have the least results in terms of the number of thermal fatigue cracks and the length of the main crack. For type B graphite and blank sample

local radiated crack morphology, the main crack bridging degree is serious, the main feature of this is due to the B graphite petal shape, after 350 times thermal cycling, a large amount of graphite decarburization cause crack extension direction of the lost relatively fixed, therefore increase the crack width after passivation and continues to grow without direction. Type C graphite by pictures regardless of whether blank or bionic samples, surface crack amount and crack wider, more throughout the entire surface and connected to each other, combining with the Fig.4.10 shows the thermal fatigue cycle late type C of a large number of crack type graphite, especially bionic has improved significantly in the late test sample rate of growth, mainly because of type C graphite is huge, On the surface of the sample has a sharp cutting effect, resulting in the strength of type C graphite grey cast iron is low, thermal fatigue crack initiation with the help of the thick type C graphite rapidly expanded, and finally achieve the effect of thick cracks all over the surface of the sample in the figure. Type D graphite due to graphite growth in dendrite itself is very small and the clearance, so the same thermal fatigue crack growth in the dendrite clearance, but due to high strength of the dendrite can only extend along the dendrite clearance thermal fatigue crack, and crack is narrow, the same reference number of crack chart shows that although the blank sample of the largest number of cracks, but the bionic sample greatly reduced the number of cracks. The blank sample surface of type E graphite can be seen obvious wide-body thick crack, which is due to the directional nature of type E graphite, the crack is relatively easier to bridge, and is not limited to the surface of the sample, but also the thermal fatigue crack will expand to the inside. It

can be concluded that the crack growth rate of blank sample is type D graphite > type C graphite > type E graphite > type B graphite > type A graphite from large to small. In addition, Fig.4.11 shows the statistical graph of crack width of blank and bionic samples of different graphite types. According to the graph, the crack width of type D graphite is the smallest, which is 62.4 microns, while that of type E graphite is the widest, which is up to 246.2 microns.

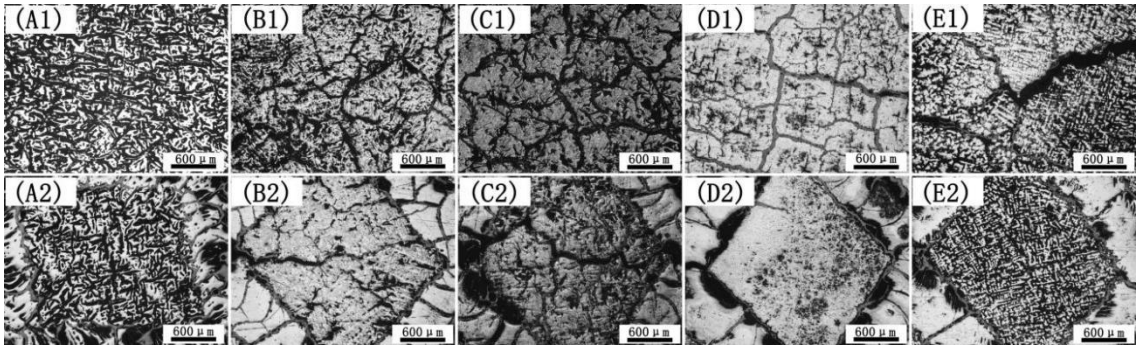


Fig.4.9 Crack morphology of blank samples and bionic samples with 350 thermal fatigue tests of different graphite types

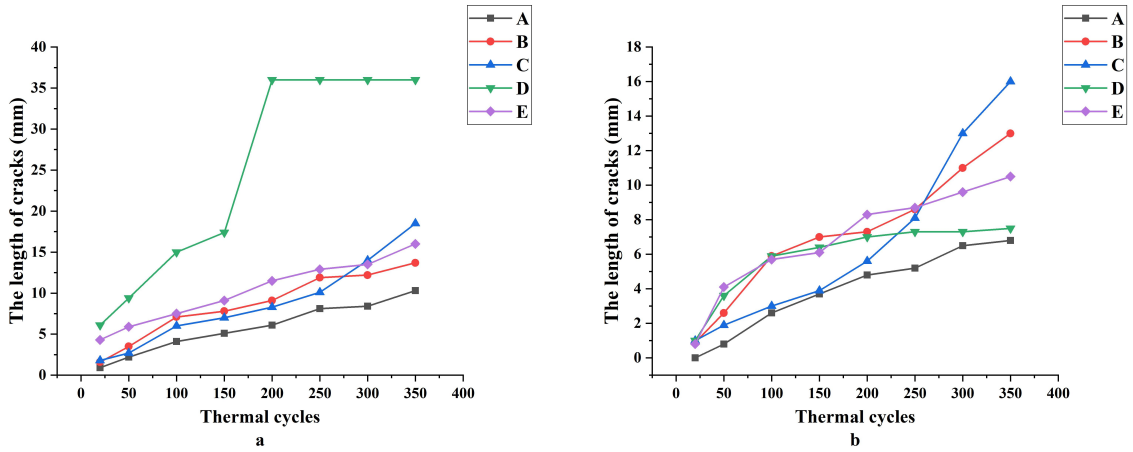


Fig.4.10 Crack lengths of different graphite types: a blank sample; b bionic sample

For part of the bionic samples subjected to Fig.4.9, the unit has played an important role in preventing the extension of thermal fatigue crack propagation, combined with Fig.4.10b bionic sample thermal fatigue crack length, the bionic thermal fatigue resistance of the whole sample is better than a blank sample, the thermal fatigue crack length is sharply reduced, this is because the unit has a refined microstructure has the high hardness at the same time. After the crack touches the unit, it is forced to turn. If the crack wants to run through the whole sample, it needs a longer path and longer time, or a longer number of thermal cycles, and accumulates more energy to break through the unit. Therefore, the bionic sample has better thermal fatigue resistance. The improvement of thermal fatigue resistance of different graphite grey cast iron by the unit mainly comes from the following aspects: First of all, the unit is similar to the surface of grey cast iron, which plays the role of a dam to a flood. When the thermal fatigue crack touches the unit, it changes its growth path or accumulates energy to break through. Either way, the time of crack penetration through the sample will be prolonged, which is equivalent to prolonging the life of grey cast iron. Secondly, there are some microcracks in the microstructure of the unit itself, which is the result of stress release during the rapid cooling process in the melted zone. In addition, with the progress of thermal cycle, martensite and carbide in the unit continue to decarbonize, and the hardness of the unit gradually decreases, and the resistance to crack decreases in the late stage of thermal fatigue. The unit effect to the promotion of type D graphite samples, the largest type A graphite samples due to its good thermal fatigue resistance, and, as mentioned above for the unit of type A and type D graphite microstructure in

grid dendrite structure, so the thermal properties of the two types of graphite grey cast iron is better than the other sample, thermal fatigue crack extension was more obstacles. The microstructure of the unit of type B graphite and type C graphite is plate-like dendrite. Compared with mesh-like dendrite, it is easier to crack in the thermal cycling process, so the thermal fatigue resistance is poor and the ability to hinder crack propagation is low. Especially for the coarse graphite type of type C graphite, the penetration ability of crack is very strong. The main crack length results of the bionic sample show that the hindrance effect of type C graphite is the worst. The hardness of the unit on the surface of the type E graphite sample is low, which is due to the low carbon content of the unit, so the thermal fatigue resistance is general.

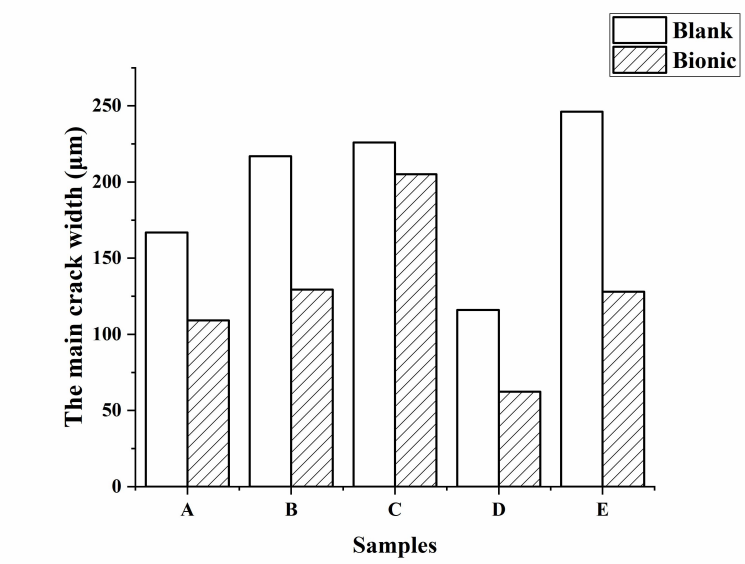


Fig.4.11 Crack widths of different graphite types after 350 thermal fatigue cycles

4.2.5 Effect of graphite type on wear property

The main failure mode of the drum brake is thermal fatigue crack running through the

top of the drum brake. The thermal fatigue crack is caused by the intense friction between the friction pair and the drum brake during braking, which leads to a sharp rise in the temperature of the contact surface. After cooling, the thermal fatigue crack is alternately formed on the grey cast iron surface. The length of fatigue crack and the thickness of wear are usually measured when the performance and service time of drum brake are tested, so it is necessary to conduct wear test on the sample to study the wear resistance of different graphite types of grey cast iron. Fig.4.12 shows the weight loss results of blank grey cast iron samples with different graphite types, bionic samples, blank samples after 150 times of thermal fatigue and bionic samples after 150 times of thermal fatigue. All samples of type C graphite samples of weight loss is minimal, although this is due to the type C graphite resistance to thermal fatigue crack is not high, but also precisely because of the thick graphite and relatively high carbon content makes type C graphite lubricant, in the process of wear and tear have played an important role in reducing grinding drag reduction, at the same time, the hardness of material itself is the highest, so weight loss minimum. The blank sample of type D graphite has the highest weight loss. According to the above study on the microstructure and hardness of type D graphite, it is found that the type D graphite is dominated by ferrite, and the hardness of the base material is low, so the wear resistance is poor.

After the coupling bionic treatment, the weight loss of different graphite samples decreased, which was closely related to the coupling bionic unit and the coupling bionic model. Unit itself high strength and high hardness compared to the nature of

the substrate material can support in the process of friction and the friction pair, the appropriate coupling bionic model by considering the rubbing direction, further consider the coefficient of friction, including the thermal fatigue wear after considering the influence of thermal fatigue crack, design a suitable model to enhance wear resistance of materials. Therefore, the wear resistance of the bionic sample is stronger than that of the blank sample. Among them, the wear resistance of type D graphite is the biggest improvement, the weight of grinding loss decreased by 67%, the reason is that the carbon content of type D graphite is higher, after laser processing in the unit melting area of the solution of carbon atoms is more, the hardness is relatively higher, so the more wear resistance in the wear process. Comparing the results of the test samples after 150 times thermal cycling wear, lose weight of the blank sample and bionic sample has increased by a above the grey cast iron after a certain heat cycle pearlite decomposition gradually, hardness of sample after surface decarburization will reduce gradually, the lubrication characteristics of graphite has also will gradually disappear, so after thermal fatigue sample weight loss will increase. However, after 150 cycles of thermal cycling, the weight loss of the bionic sample is still reduced a lot, which proves that the coupling bionic unit can improve the wear resistance of the material and the wear resistance after thermal cycling.

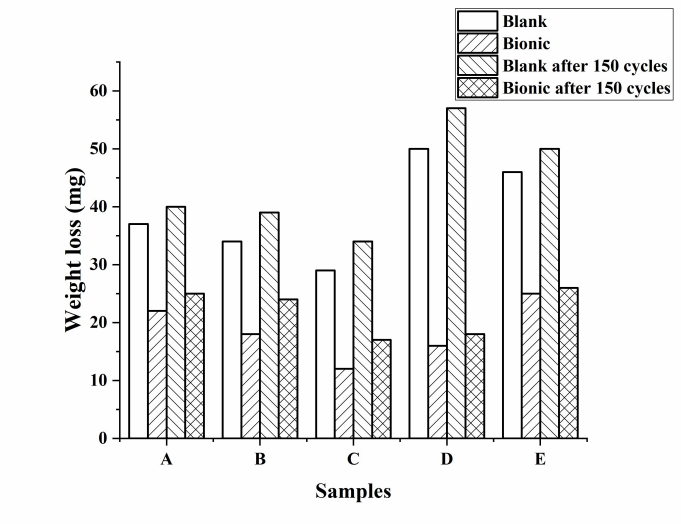


Fig.4.12 Weight loss by grinding of different graphite types

4.3 Effects of carbon content on thermal fatigue and wear resistance of coupling bionic samples

These different types of graphite grey cast iron are studied in thermal fatigue and wear resistance, and thermal fatigue and wear resistance of bionic coupling were investigated, the influence of the type C wear resistance of graphite samples is best, bionic coupling model of type D graphite grey cast iron wear resistance increase of maximum, the promotion of type D graphite thermal fatigue resistance is also the biggest. The application of laser coupling bionic technology is very meaningful and has a prospect in terms of the thermal fatigue and wear resistance of different graphite types to the base material. When considering specific products, such as truck drum brake, type C graphite and type E graphite grey cast iron themselves have poor thermal fatigue resistance, type D graphite itself is relatively small shape, thermal conductivity and shock absorption is insufficient, there are safety risks in the actual production, cannot be selected as the drum brake production material. But type A best

thermal fatigue resistance of graphite itself, the distribution of internal stress in the thermal cycle relatively most average, is the preferred as truck drum brake of grey cast iron material, but on the wear and tear shows type A graphite grey cast iron wear resistance, so need to type A graphite grey cast iron on friction performance research. In addition, the pearlitic grey cast iron base material has better thermal fatigue and wear resistance than the ferrite grey cast iron base material. At the same time, the performance of grey cast iron is closely related to the carbon content and hardness, but the melting loss will occur in the casting process, and the burning loss will lead to the reduction of carbon content and the change of performance. This chapter mainly studies the thermal fatigue and wear resistance of grey cast iron with different carbon content and samples with coupling bionic unit by preparing type A graphite grey cast iron and changing different carbon content to control the different amount and size of graphite.

4.3.1 Base metal structure with different carbon content

According to the chemical composition in Table 2.3, four kinds of grey cast iron with different carbon content were prepared, and the microstructure was shown in Fig.4.13. The carbon content of the four samples (a)-(d) in the figure is 2.86%, 3.05%, 3.28% and 3.46% respectively. The four kinds of grey cast iron with different carbon content are all type A graphite. It can be seen from the figure that with the increase of carbon content, the average length and quantity of graphite increase. By calculating the proportion of graphite in the figure, the proportion of graphite in the total area of the

four samples is 8.2%, 9.41%, 11.02%, 12.38%, indicating that when the carbon content increases, the graphite volume in the grey cast iron base also increases.

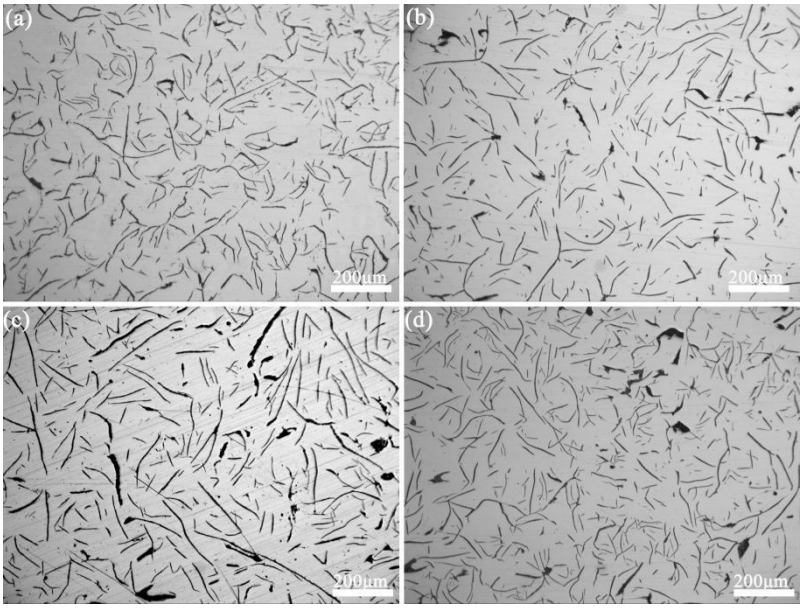


Fig.4.13 Graphite morphology with different carbon contents: (a), 2.86%; (b), 3.05%; (c), 3.28%; (d), 3.46%

By observing the base material area in Fig. 4.14, it can be seen that the base part of 2.86% sample with the least carbon content is very ferrite, while the rest part is pearlite and graphite. With the increase of carbon content, the content of ferrite becomes less and less, and the base of 3.46% sample with the most carbon content becomes grey cast iron base material dominated by pearlite. It can be seen that the higher the carbon content, the less ferrite content, and the more pearlite content, the higher the hardness of the base material.

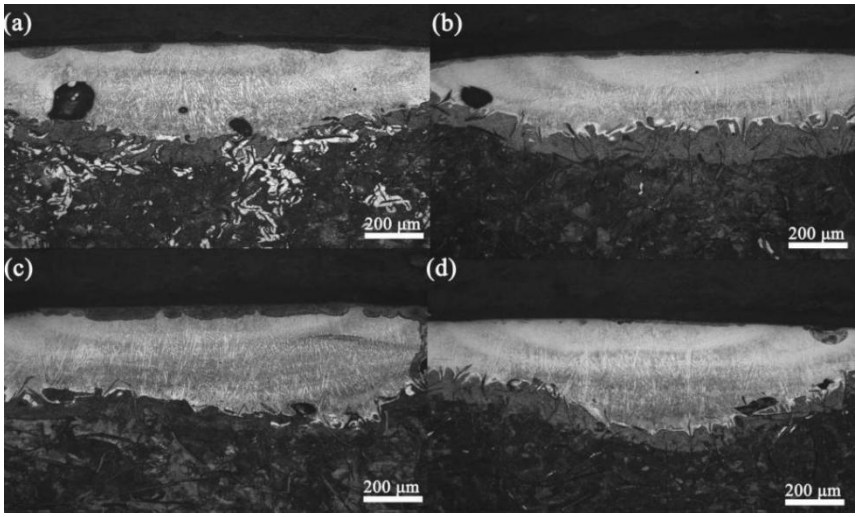


Fig.4.14 Morphologies of unit cross section of samples with different carbon contents: (a), 2.86%; (b), 3.05%; (c), 3.28%; (d), 3.46%

4.3.2 Analysis of microstructure of sample units with different carbon content

First of all, according to Fig.4.14 above, the white bright area is the coupling bionic unit, and the cross-section morphology of grey cast iron with different carbon content is shown in the figure. The graphite is completely dissolved in the melted area, and the hypoeutectic white structure formed in the melted area is dendrite shape during the rapid cooling process. Because the carbon content is less, the higher the ferrite with the increase of carbon content pearlite, the more the number and length of graphite increases at the same time, so the higher carbon content of sample has better thermal conductive performance, which explains using the same laser parameter processing unit, however, different morphology of the carbon content of the sample unit, better thermal conductivity of carbon content is higher of grey cast iron fused area further. The temperature of the laser heat source on the surface of the sample is

basically the same. With better thermal conductivity, the temperature will spread faster to the inside of the sample. In the process of rapid energy transfer, the temperature will be cooled to the freezing point at a position farther away from the heat source.

In order to observe the microstructural morphology of surface units of grey cast iron with different carbon content more clearly, SEM was used to observe the unit structures of four kinds of grey cast iron, which were 2.86%, 3.05%, 3.28% and 3.46% carbon content samples in turn, as shown in Fig.4.15. It can be seen from the figure that the microstructure composition of the samples with different carbon content is basically the same, which is composed of residual austenite, martensite and cementite, but the dendrite density and number are different. It can be found from the figure that with the increase of carbon content, the eutectic structure in the melted area is more and the carbides are denser and finer. This is because the increase of carbon content enhances the thermal conductivity of grey cast iron, the cooling and solidification speed in the melted area is extremely fast, and the increase of carbon content enhances the eutectic transition in the melted area.

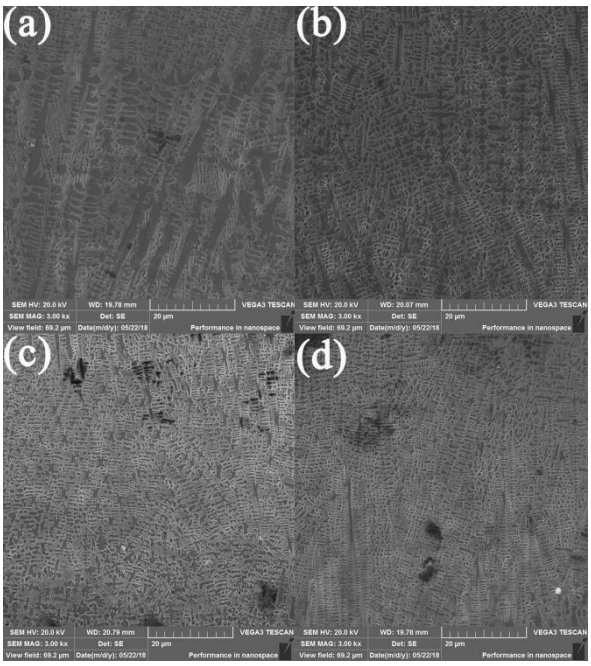


Fig.4.15 Morphology of unit of samples with different carbon contents: (a), 2.86%; (b), 3.05%; (c), 3.28%; (d), 3.46%

4.3.3 Effect of different carbon content on thermal fatigue resistance

With the accumulation of a certain number of thermal cycles, the microstructure of grey cast iron material and unit will change. Fig.4.16 shows the microstructure change before and after the conventional state and 300 thermal fatigue tests of grey cast iron base and unit area. In the thermal fatigue test, the thermal properties of grey cast iron change when the temperature of the sample increases, and the graphite and the base are in a non-uniform state, and the cyclic thermal cycle leads to the initiation of cracks between the graphite and the base. Graphite in the thermal cycle process continuously spread out, meanwhile the oxygen in the air along the phase interface into the grey cast iron substrate, thermal cycle continues to graphite and bast of the gap is more and more big, the oxygen constantly seeps into the interior of the substrate [40, 77, 215],

oxidation reaction with the graphite iron around, this is the reason of the graphite oxide generated around, this part of the oxide forms a loose structure around the graphite. Except graphite substrate with pearlite is given priority to, because the pearlite layer is composed of ferrite and cementite flake mechanical mixture, as a kind of metastable structures and cementite on thermal fatigue test was easy to decompose, lead to pearl experience as thermal cycle decomposition fragmentation, the content of pearlite gradually reduce, in a ferritic around the graphite. It can be seen from the figure that the microstructure of the unit is fine and tight without thermal fatigue test. However, with the progress of thermal fatigue test, the number of thermal cycles gradually increases, and holes appear on the surface of the unit due to thermal expansion and cold contraction.

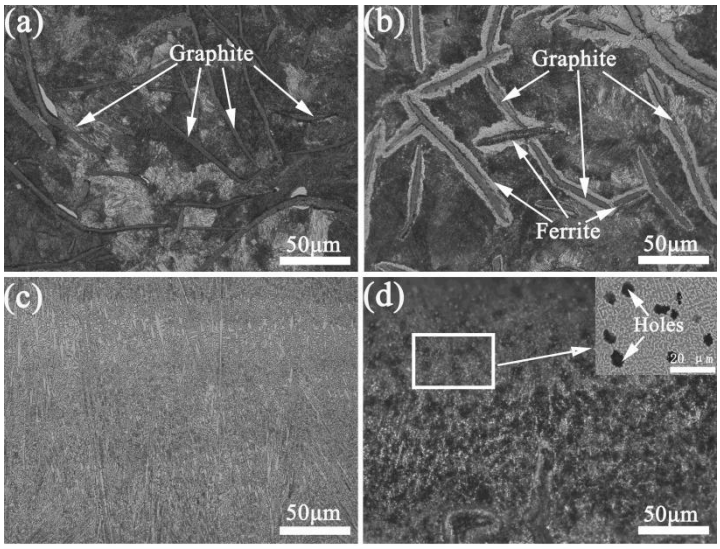


Fig.4.16 (a)microstructure of base before thermal fatigue test; (b), the microstructure of the base at 300 times of thermal fatigue; (c), the structure morphology of the unit before thermal fatigue test; (d), the microstructure of the unit at 300 times of thermal

fatigue

Since the microstructure of the base changed after a certain number of thermal cycles, the microhardness changed accordingly. Fig.4.17 shows the microhardness change curves of the base and unit of samples with different carbon content under different conditions. According to 4.17A, within the range of samples used in this study, the higher the carbon content of the base without any treatment, the higher the microhardness of the base. The main reason is that the base is based on pearlite, and the higher the proportion of pearlite with high carbon content, the higher the hardness. After 300 thermal fatigue tests, there is a large difference between the microhardness values of the wear surface and the inner surface of the sample, and even the hardness of the wear surface is slightly higher than that of the base without thermal fatigue test, while the hardness of the inner surface is much lower than that of the wear surface. The thermal fatigue test is accompanied by the decomposition of pearlite, and part of the carbon is enriched on the surface of the sample, while the other part is dissociated in the sample base [216]. Therefore, the microhardness inside the base is much lower than that without the thermal fatigue test. The hardness of the surface worn after thermal fatigue is higher than that of the untreated sample, partly because the excessive cooling rate during thermal cycling leads to the formation of martensite [32]; on the other hand, the surface work hardening of the sample during the wear process leads to the increase of its hardness. Fig.4.17b shows the microhardness curve of the unit under different conditions. It can be seen from the figure that the microhardness of the unit is also the higher the carbon content, the higher the hardness, and the

smaller the microhardness with the thermal fatigue and the more thermal cycles. The main reason is that the grey cast iron with higher carbon content in the laser processing process has more carbon dissolved in the laser melted zone, and the carbide in the unit is relatively more. In addition, comparing the hardness curves of the untreated base and unit, it can be seen that the hardness value of the unit is more than two times higher than that of the base. However, with the progress of the experiment, the cementite decomposed into ferrite and graphite, and the metastable structure was gradually transformed into a stable structure, so the hardness decreased.

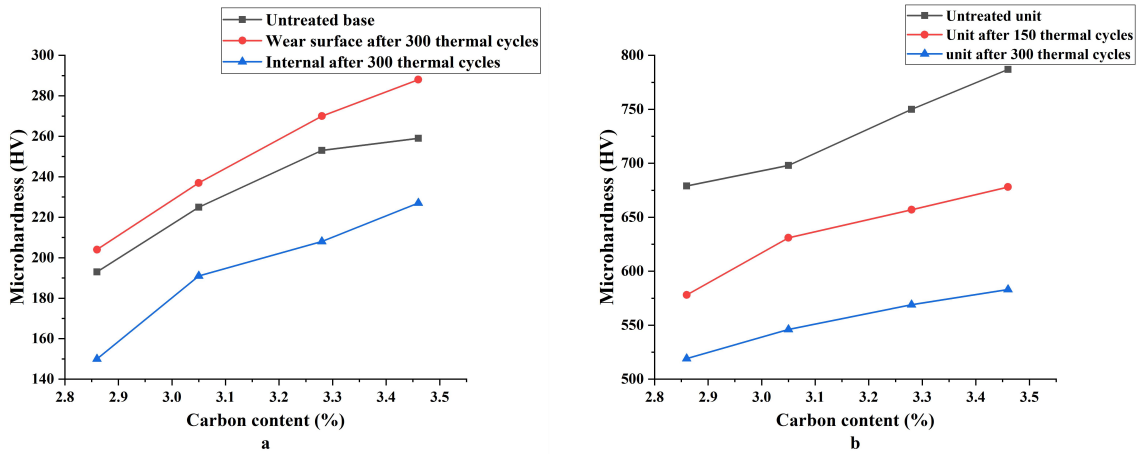


Fig.4.17 a, microhardness curve of blank samples with different carbon contents under different conditions; b, curve of microhardness change of unit with different carbon content under different conditions

As mentioned above, oxidation has a great influence on the thermal fatigue resistance of grey cast iron, and oxidation will accelerate the expansion of thermal fatigue cracks in the thermal cycling process. Therefore, it is necessary to study and analyze the oxidation resistance of grey cast iron with different carbon content. First of all, the

material's organization, structure, trace elements and so on will have a certain impact on the oxidation resistance. For grey cast iron carbon content increases, relative also increases, the amount of graphite after certain thermal cycle, graphite and base, due to the different thermal physical properties such as the different thermal expansion coefficient, which combined with the existing gap, at this time the oxygen in the air can enter the gap, is equivalent to the contact area of increased. Therefore, as mentioned above, the carbon content of grey cast iron increases, the amount and size of graphite increase, and the oxidation rate increases at the same time. Fig.4.18 shows the statistical chart of oxide layer thickness of grey cast iron base and unit with different carbon content substrate and oxygen, accelerating the oxidation rate of the materials. The thickness of the oxide layer increases with the increase of carbon content regardless of whether the unit is contained or not, but the thickness of the oxide layer of the unit is much lower than that of the base, indicating that the unit has better oxidation resistance. Unit is obtained by laser fused with ultrafine organization structure of graphite in the region of the fused completely dissolved, grain refinement is due to good thermal conductivity metal itself makes fused area rapid cooling, thus unit thin organization, the oxygen in the air is not easy to enter the unit inside, contact with different base, and the relatively narrow, so better oxidation resistance. However, the oxide layer thickness of the unit also increases with the increase of carbon content, and the reduction degree of the base oxide layer thickness gradually decreases, which is 54%, 45%, 40%, 35% in turn. The main reason is that the carburizing inside the unit is decomposed during the thermal cycle, and a large amount of carbon

precipitates and oxidizes with oxygen element. And when the thermal cycle is carried out to a certain extent, the unit as hard phase is brittle, which is easy to break after bearing a certain thermal stress, leading to the increase of contact surface with oxygen element.

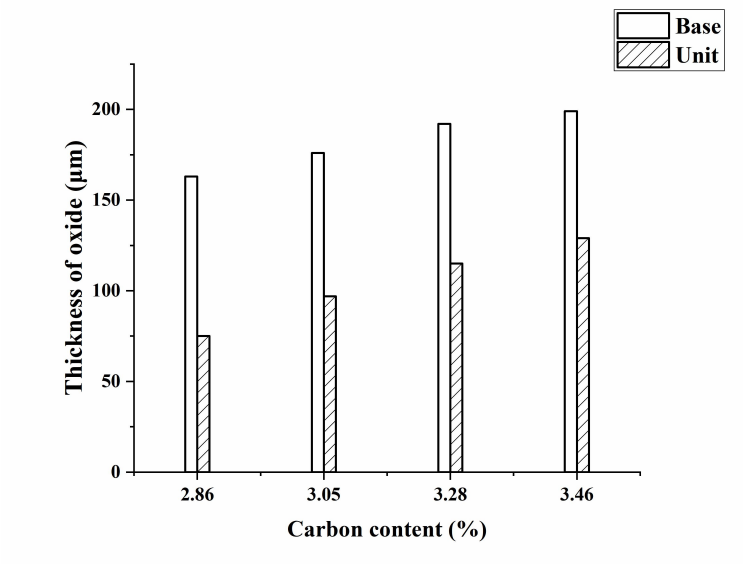


Fig.4.18 Oxide layer thickness of base and unit with different carbon contents

This chapter studies the influence of different carbon content on the thermal fatigue and wear resistance of grey cast iron. The graphite type is type A grey cast iron, and the material itself has relatively good performance. Changing the carbon content within a certain range can find different thermal fatigue resistance laws among grey cast iron. When the carbon content is higher, the quantity, size and length of graphite in grey cast iron increase, and the thermal fatigue resistance of grey cast iron is also different. Fig.4.19 shows the statistical chart of the number of thermal fatigue cracks of blank samples and bionic samples under different thermal fatigue times for samples

with different carbon content. Fig.4.20 shows the statistical chart of the main thermal fatigue crack length of blank samples and bionic samples under different thermal fatigue times for samples with different carbon content. The figure shows that all the samples of thermal fatigue cracks with the increase of the carbon number increase, the main reason is that carbon content increase means that the number of graphite base, and the size and the increase of the length, the graphite itself is equal to the crack source in the thermal cycle, graphite easy to crack initiation stress concentration, the greater graphite morphology, the equivalent of defects, the greater the more the more prone to thermal fatigue crack. At the same time, the amount and size of graphite have a certain impact on the thermal fatigue crack bridging, the more graphite makes the crack bridging easier, so the more carbon content, the more cracks. On the contrary, the main crack length of the samples with different carbon content is opposite. The higher the carbon content, the lower the main crack length is. The reason is that the thermal conductivity of graphite is much higher than that of cast iron. The higher the carbon content, the more graphite, the better the thermal conductivity of the base metal. Good thermal conductivity can reduce the temperature gradient in the process of thermal fatigue test, that is, reduce the internal stress of the sample. At the same time, the higher the carbon content, the higher the pearlite content in the base material, which has a certain ability to hinder the microscopic cracks in the early stage of thermal cycle. After several thermal cycles, the microscopic crack grows and expands into macroscopic thermal fatigue crack. The morphology and quantity of graphite are no longer the main factors affecting the crack growth. Therefore, the length of the

main thermal fatigue crack of grey cast iron with better thermal conductivity is shorter and the thermal fatigue resistance is better.

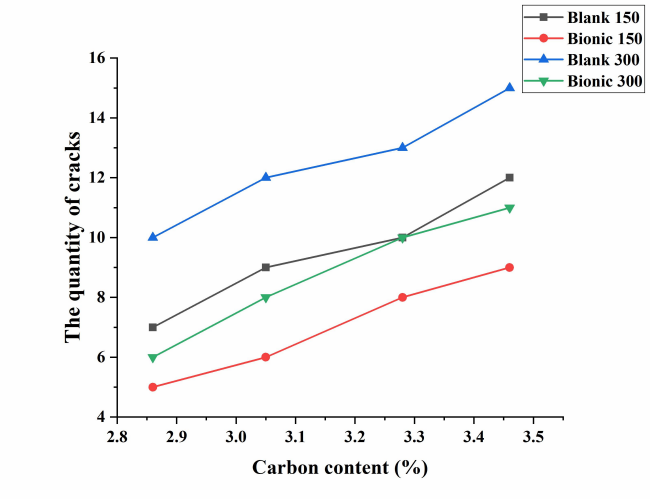


Fig.4.19 The quantity of thermal fatigue cracks in different thermal fatigue cycles of grey cast iron with different carbon contents

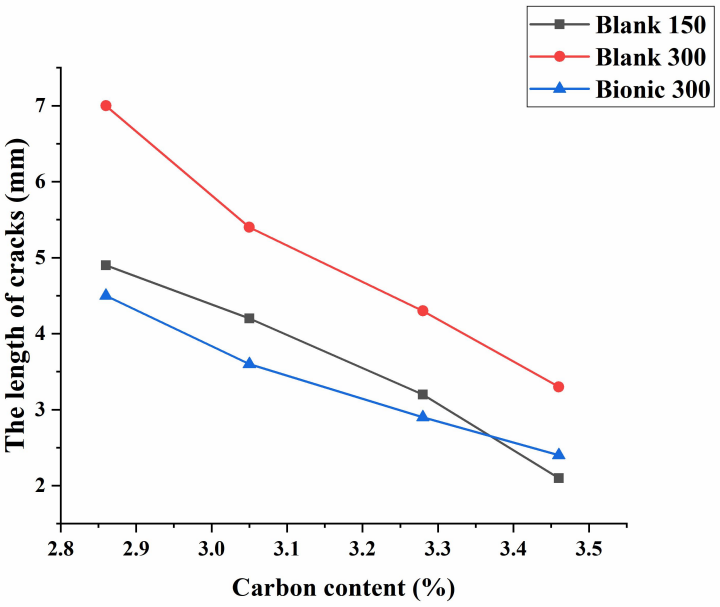


Fig.4.20 Length of thermal fatigue main crack of grey cast iron with different carbon contents in different thermal fatigue cycles

In addition, it can also be seen from the figure that the number of thermal cycles and

the coupling bionic unit have a significant impact on the thermal fatigue resistance of samples with different carbon content. Firstly, the more thermal cycles, the more thermal fatigue cracks of blank and bionic samples with different carbon content, and the longer the main crack length. The reason is that thermal cycling will accelerate the oxidation rate, and the higher the number of thermal cycles, the faster the oxidation rate. At the same time, the pearlite decomposition, the hardness of the base metal will decrease with the increase of the number of thermal cycles, so the thermal fatigue resistance of the sample gradually weakens. The sample with coupling bionic unit has better performance in terms of the number and length of cracks than the blank sample. Even when the number of cracks of the bionic sample is similar to that of the blank sample after 300 thermal cycles, the main crack length is similar, and the thermal fatigue resistance of the sample is greatly improved. With the increase of carbon content, the hardness of the unit is higher, and the hindering effect of microcrack is obvious in the early stage of thermal fatigue test, so the growth rate of crack is relatively slow. With the progress of the test, the unit becomes brittle and prone to cracking under sufficient thermal stress [32]. However, the crack formed in this way helps to release the stress on the surface, effectively hinders the thermal fatigue crack propagation of the base, changes the direction of crack growth, and increases the path of crack propagation. For grey cast iron samples with relatively little carbon content, the number and shape of graphite are relatively small, and the thermal fatigue crack is not easy to initiate and expand. Compared with the samples with high carbon content, the effect of preventing crack initiation is better.

4.3.4 Influence of different carbon content on wear performance

Different carbon content in this chapter is thermal fatigue and wear resistance of bionic grey cast iron were investigated, the influence of grey cast iron drum brake on thermal fatigue crack is born of braking friction heat after cooling, by reciprocating cycle generates hot fatigue crack, resulting in drum brake, so design wear test for every 150 times thermal fatigue wear test was carried out on the sample after test, In order to simulate the actual working conditions of the drum brake, the sliding wear time is 20 hours, the load is 100N, and the friction speed is 0.15m/s. The friction pair used in this experiment is taken from ceramic brake pads, and the hardness is about 620.5HV. The wear resistance of the samples with different carbon content was detected by comparing the weight loss and wear morphology before and after the test. Fig.4.21 under different carbon samples in different thermal cycling times, namely the grinding weight loss as a result, the blank sample results show that with the increase of carbon loss weight became smaller, the main reason is to increase the content of pearlite in the base material, the carbon content of base hardness is relatively large, so in less weight loss in the process of wear and tear. In addition, the number and size of graphite samples with higher carbon content are relatively more, and graphite can play a certain lubricating role in wear, so the higher the carbon content of the sample, the less weight loss. For the wear results of blank samples after 150 thermal cycles, compared with the blank samples for thermal fatigue test, it can be seen that the overall weight loss is higher, and the higher the carbon content is, the lower the

weight loss is. The reason is that after the thermal cycle, the surface work hardening of the sample leads to higher hardness, but the hardness of the base material is lower than that before the treatment, and more grinding occurs during the wear process. Moreover, thermal fatigue cracks will aggravate the wear to a certain extent. Therefore, the same load conditions and the same friction pair make the wear degree of the base material higher. For blank samples, the change rate of weight loss decreases with the increase of carbon content, which is closely related to the graphite pits and thermal fatigue cracks on the surface of samples after thermal fatigue test.

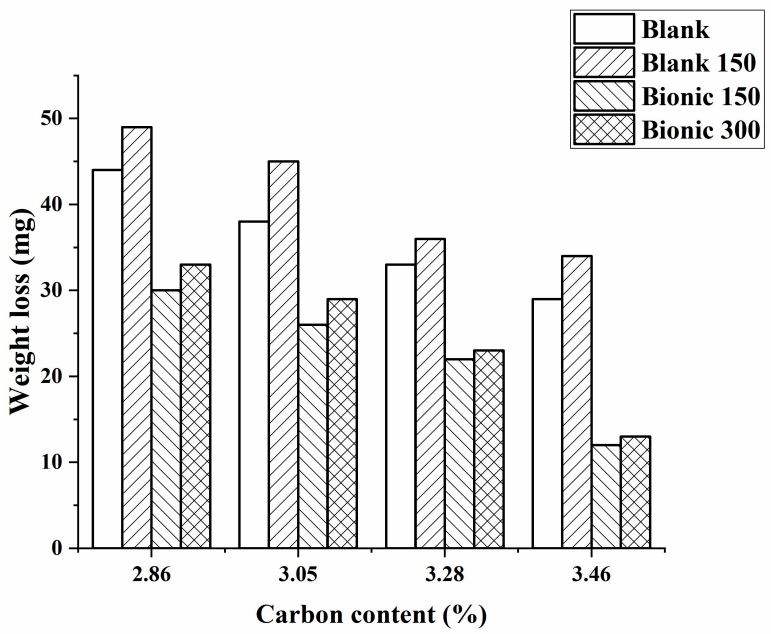


Fig.4.21 Grinding weight loss of samples with different carbon contents after different thermal fatigue tests

Fig.4.22 shows the wear topography of graphite pit region and thermal fatigue crack region. The figure illustrates the degree of wear of graphite pit area and crack area is much higher than other area, the plough cut around, and because the carbon content

increases the number of leads to graphite pit also increases, the graphite pit is a result of thermal cycle after accumulated to a certain degree, combined with close enough to graphite and base from, formed in the friction surface of graphite pit. In the process of friction, the abrasive particles on the surface of the sample will accumulate in the graphite pits and cracks to a certain extent. With the wear test, the abrasive particles detaching leads to the generation of ploughing, which aggravates the wear amount. Therefore, with the increase of carbon content, the reduction rate of weight loss slows down.

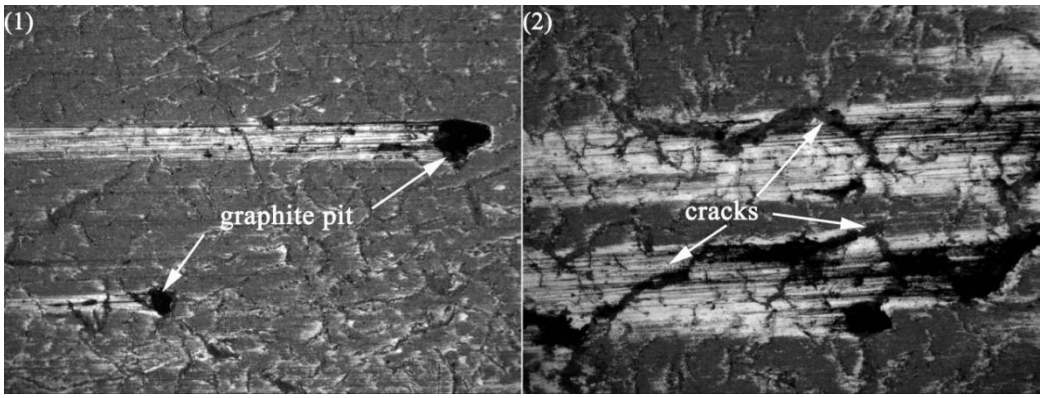


Fig.4.22 Wear morphology: a, wear morphology in graphite pit area; b, wear morphology of thermal fatigue crack area

Fig.4.23 is the elemental analysis diagram of the graphite pit region and the thermal fatigue crack region. By EDS analysis result, the graphite iron pit and thermal fatigue crack area decreased, oxygen, there are a lot of iron oxide particles in the pit, it is because of the existence of these particles cause the plough cut production in the process of wear and tear, as shown by graphite pit and crack wear path wear degree is greater than the other parts of the substrate material, Thus, the wear on the sample

surface is increased.

However, the wear of the bionic sample is much lower than that of the blank sample. According to the results of wear loss weight, within the research scope of this study, the trend of wear loss weight of samples with different carbon content is similar to that of blank samples, the higher the carbon content is, the less weight loss will be lost, and with the increase of thermal cycles, the wear loss of samples with the same carbon content is relatively higher. Main reason lies in the high strength and high hardness of the unit itself played a supporting role in the process of wear and tear, the bionic model for the most part bear the stress, effectively reduce the wear of base, at the same time for after the thermal fatigue wear process unit can not only hinder the thermal fatigue crack, can also be a certain extent, prevent wear debris damage to the substrate, Therefore, the wear resistance of the bionic sample is much higher than that of the blank sample. Fig.4.24 the unit and the junction of the wear morphology base, and the figure of the unit area is on the right and left for the base area, the images to the red part shows relatively prominent, the more biased towards the blue area relative to sag, the figure shown distinct boundary base and unit, unit area is relatively flat, the height difference is not big, and the height difference base part, It can be seen that the wear resistance of the unit is better than that of the base. When the base is severely worn, the unit can play a supporting role and effectively improve the wear resistance of the sample.

Fig.4.25 shows the wear morphology of the substrate area of bionic samples with different carbon content. Within the scope of the research of this study, all sample

almost no visible graphite pit or thermal fatigue crack can accelerate abrasion defects, such as main existence was part of the base spalling, and the lower the carbon content of sample surface spalling of the more severe, the more the higher the carbon content material containing graphite, lubrication, the more obvious in the wear process, and bionic model good wear-resisting performance, Therefore, the higher carbon content of the sample, the less wear, the better wear resistance. At the same time, it can be seen from the above that the hardness of the unit decreases after a certain number of thermal fatigue times are accumulated, so the supporting effect of the unit for friction is a gradual decline process. With the progress of the test, the function of the unit is gradually weakened, and the wear rate is gradually increased.

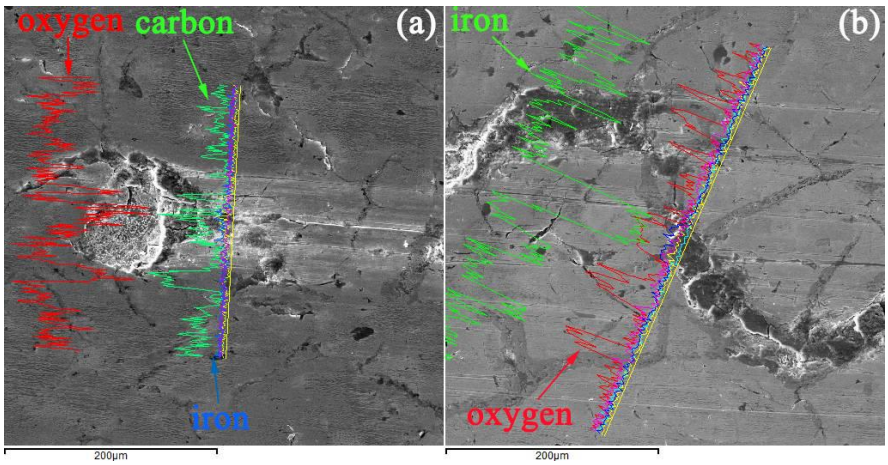


Fig.4.23 EDS analysis: a, element analysis at graphite pit; b, element analysis at thermal fatigue crack

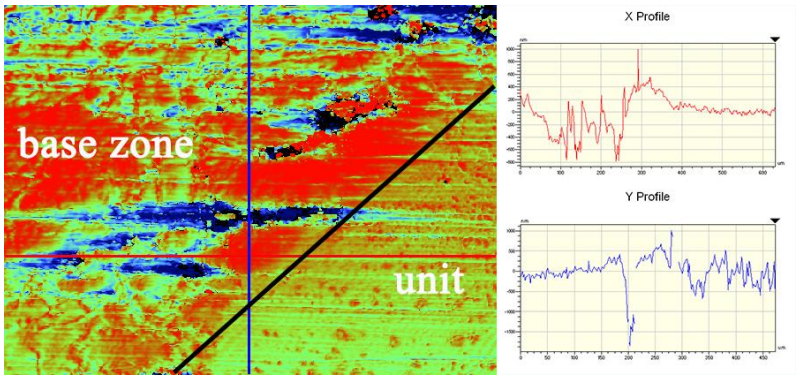


Fig.4.24 Wear morphology at the interface between the bionic sample unit and base

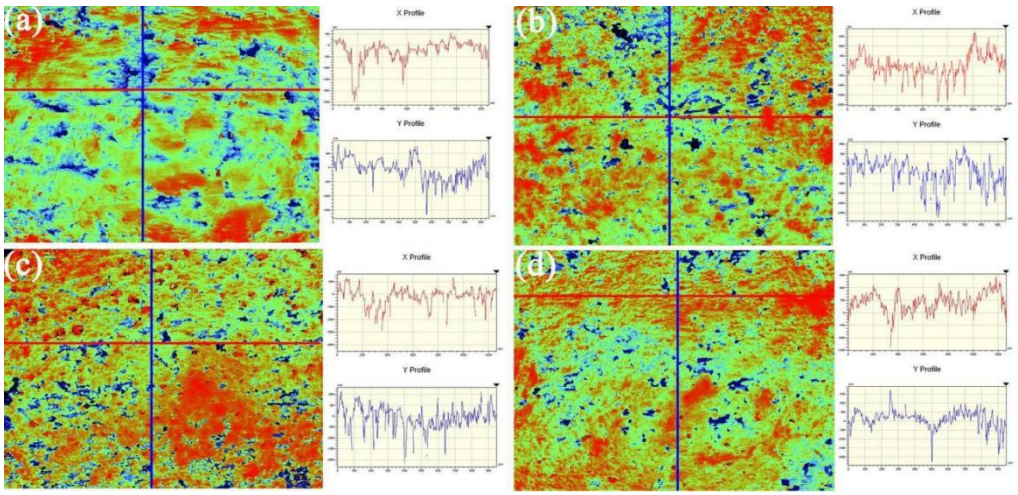


Fig.4.25 Wear morphology of samples with different carbon contents: (a), 2.86%; (b), 3.05%; (c), 3.28%; (d), 3.46%

4.4 Effects of pearlite content and interlamellar spacing on thermal fatigue and wear resistance of coupling bionic samples

As the main research the different types of graphite and carbon content on the preparation of coupling laser bionic grey cast iron the influence law of thermal fatigue and wear resistance, except graphite grey cast iron base in the base metal main organization is pearlite and ferrite, by the above research shows in grey cast iron after a certain number of thermal cycle base organization changes, it will affect its own

performance and the preparation of the coupling bionic unit. Similarly, the change of pearlite before and after thermal fatigue has a great influence on the performance of grey cast iron. Many conclusions have been drawn on the research of pearlite in grey cast iron. However, the influence of pearlite on the coupling bionic unit, on the thermal fatigue and wear of coupling bionic grey cast iron has not been studied. Therefore, this chapter selects the parts with different pearlite content and interlamellar spacing in different parts and regions of grey iron drum brake due to different cooling rates during casting and prepares grey iron samples with different content and interlamellar spacing, so as to study their influence on coupling bionic grey iron during thermal fatigue and wear cycle. This study provides data and theoretical support for the selection of different pearlite content and interlamellar spacing substrates when using laser surface coupling bionic treatment in practical production.

4.4.1 Base metal structure with different pearlite content and interlamellar spacing

The pearlite content of each sample is calculated according to quantitative metallography. The pearlite content of each sample is shown in Table 4.1 and the metallographic diagram of each sample is shown in Fig.4.26. Since the automatic image analysis software is based on the quantitative analysis of different microstructures presented in different grey levels after corrosion, the pearlite with larger interlamellar spacing cannot be identified because it appears white under the

microscope after corrosion. The pearlite content varies in different regions of the drum brake because the thickness of the casting wall is closely related to the cooling rate during the casting process [217]. Considering the drum brake top reinforcing ring position is the thickest, the bottom flange position is the thinnest. When the wall thickness decreases and the cooling rate increases, the graphite becomes finer, the pearlite increases, and the strength and hardness increase. On the contrary, when the wall thickness is thick and the cooling rate is slow, the graphite becomes coarse, the ferrite content increases, and the strength and hardness decrease.

Table 4.1 Pearlite contents and interlamellar spacing of all samples.

Sample	Pearlite contents (pearlite+ ferrite=100%)	Pearlite interlamellar spacings
A	70%	865nm
B	80%	792nm
C	85%	813nm
D	90%	832nm
E	95%	736nm
F	98%	745nm
S1	90%	860nm
S2	95%	720nm
S3	90%	188nm
S4	95%	152nm

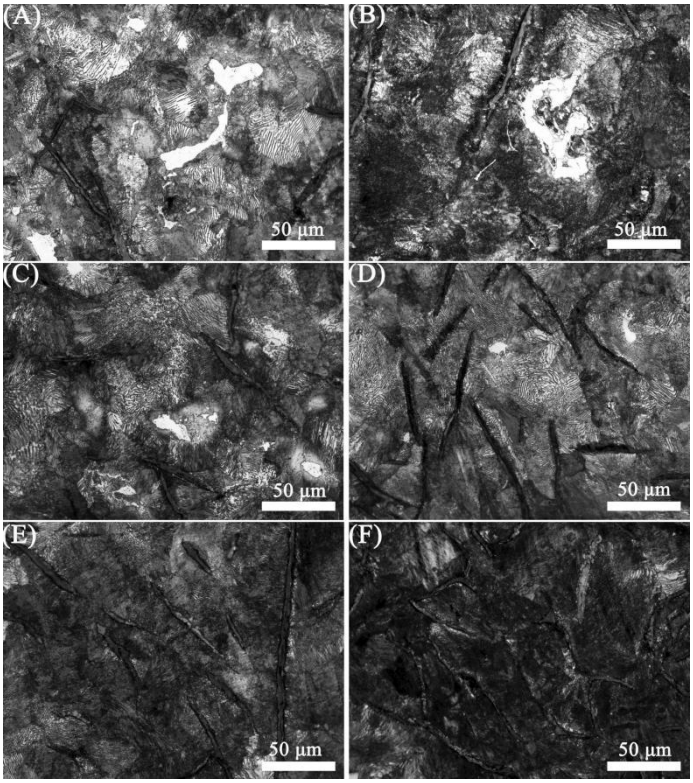


Fig.4.26 Metallographic photographs of different pearlite contents: (A), 75%;(B), 80%;(C),85%;(D), 90%;(E), 95%;(F),98%

Fig.4.27 shows the optical microscope images of samples with different pearlite interlamellar spacing at 1000 times magnification. As the distance between the pearlite interlamellar spacing of S3 and S4 samples in Fig. 4.27 is very small, the optical microscope cannot meet the observation requirements. Therefore, the scanning electron microscope (SEM) is also carried out on S3 and S4 samples, as shown in Fig. 4.28. The interception method was used to measure [218], and the average spacing between the pearlescent layers was 860nm, 720nm, 188nm and 152nm. Pearlite interlamellar spacing is determined by temperature [219]. The formation of pearlite requires a certain temperature range. Because the formation temperature of the pearlite is higher in the first cooling, the diffusion speed of C atom is fast, the

diffusion distance is long, and the pearlite interlamellar spacing is large. With the decrease of temperature, the pearlite obtained after cooling increases due to the increase of condensation inhibition, the nucleation rate increases, and the diffusion velocity and diffusion distance of C atoms decrease, resulting in the decrease of interlamellar spacing.

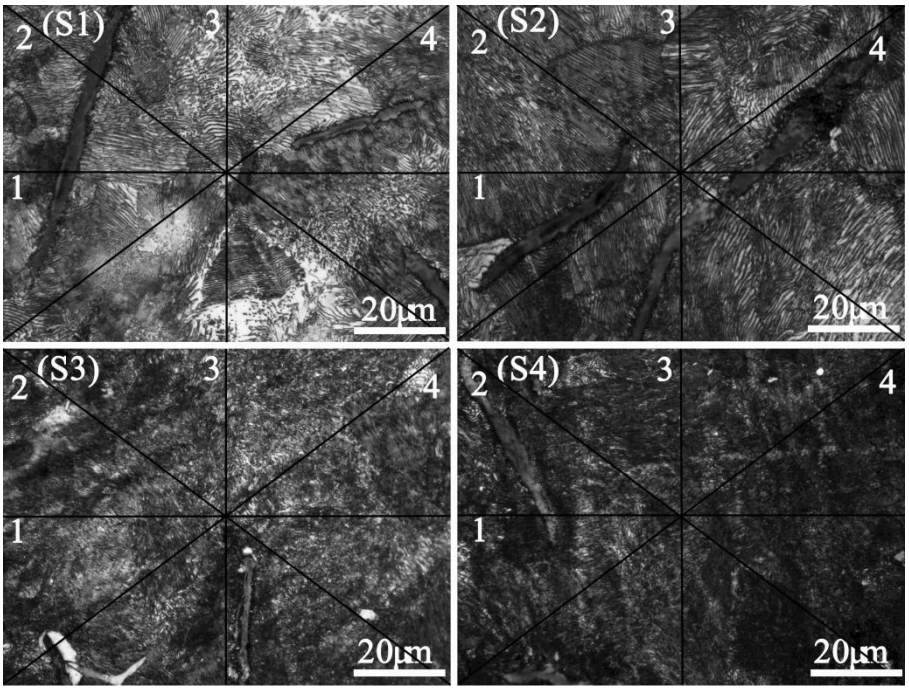


Fig.4.27 Metallographic pictures of different pearlite interlamellar spacing: (S1), 860nm; (S2) ,720nm; (S3), 188nm; (S4), 152nm

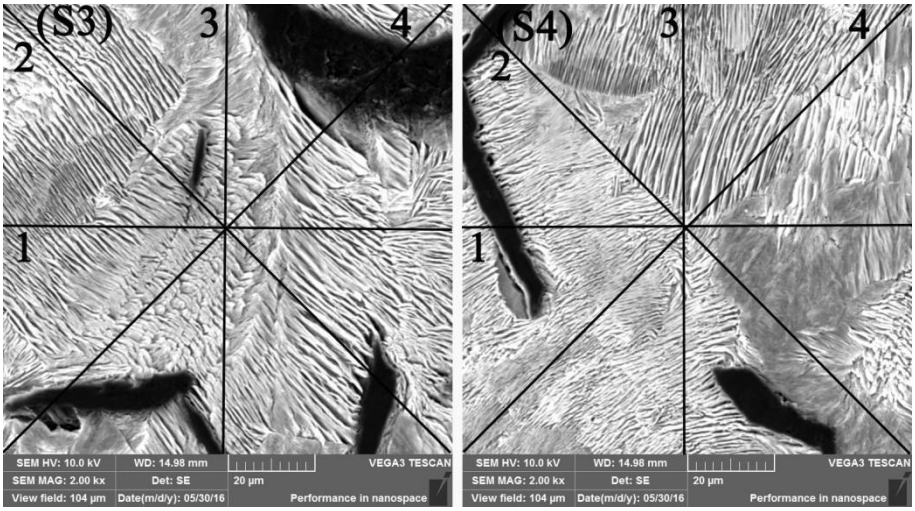


Fig.4.28 SEM metallographic of different interlamellar spacing of pearlite: (S3), 188nm;(S4), 152nm

Base hardness and unit hardness of samples with different pearlite content are shown in Fig.4.29. Two different modes are used to represent the base and the unit respectively. Vertical trapezoidal display is used to show the hardness difference between the samples more clearly. The hardness of the unit of all samples is much higher than that of the base, and the hardness of each sample unit is not different. From A to F, the hardness of the base of each sample shows an increasing trend. The different hardness of base is due to the different pearlite content. Because pearlite is a mechanical mixture of ferrite and cementite [220], it has higher strength and hardness, so the sample with more pearlites has higher hardness. When comparing all the samples, there is no significant difference in the hardness of the unit, because the solid phase transformation occurs in the laser-fused region, all the graphite is dissolved, and then the melted region is rapidly cooled to obtain fine structures such as martensite and ledeburite.

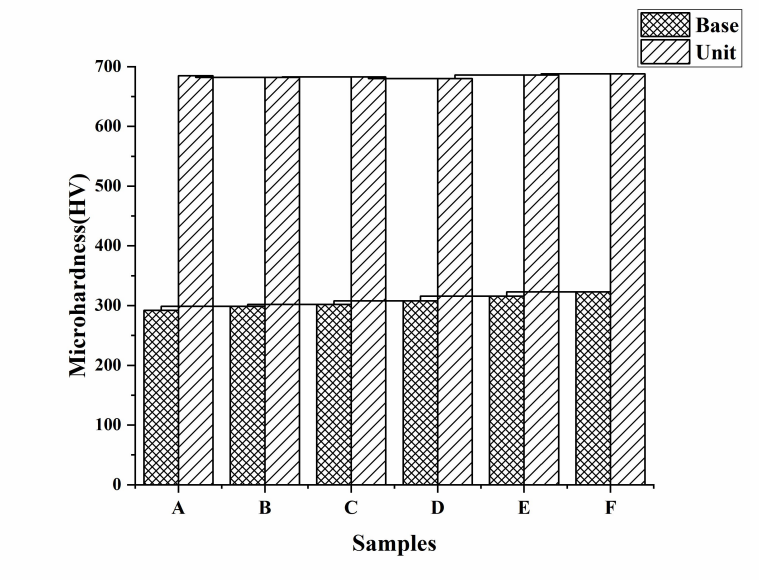


Fig.4.29 Microhardness of samples with different pearlite contents

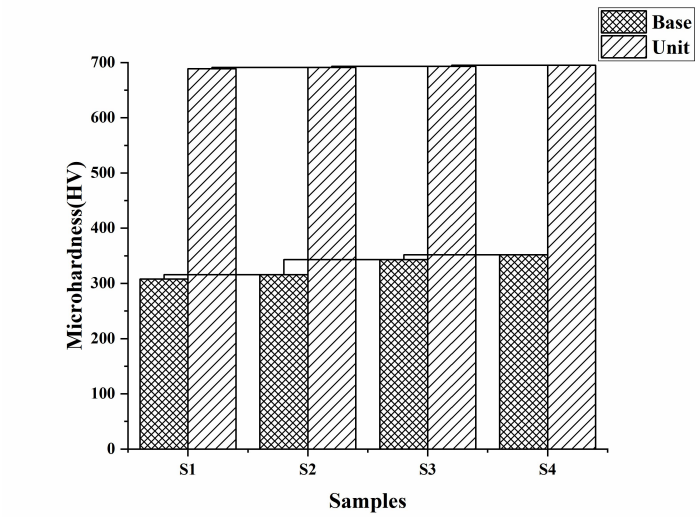


Fig.4.30 Microhardness of samples with different pearlite interlamellar Spacing

Fig.4.30 shows the microhardness results of samples with different pearlite interlamellar spacing. The hardness of the unit in the figure is much higher than that of the base, and the hardness of the unit in each sample is very similar. S1 and S2 have similar hardness, S3 and S4 have similar hardness, S3 and S4 have higher

hardness than S1 and S2. The hardness of sample S4 with the smallest spacing is the highest. The reason for this result is that the mechanical properties of the pearlite are determined by the distance between the pearlite sheets. The smaller the distance between the pearlite sheets, the higher the strength and hardness. It can be seen that the hardness after laser bionic treatment is related to the unit itself and has nothing to do with the distance between the interlamellar spacing before laser treatment.

4.4.2 Effect and analysis of different pearlite content on thermal fatigue resistance of samples

In this study, the number of cracks and the length of the main cracks are observed and calculated every 200 cycles through the thermal fatigue test. Since the thermal fatigue crack of the drum brake is macroscopic, the observed crack must be greater than or equal to 1mm.

Firstly, the thermal fatigue test was carried out on the samples with different pearlite content. According to the results shown in Fig.4.31A, the number of cracks increases with the increase of the number of thermal fatigue cycles, but the growth rate is not the same. It can be seen from the figure that when thermal fatigue cracks were observed 200 times for the first time, sample A with the lowest pearlite content had the largest number of cracks, while sample F with the highest pearlite content had the smallest number of cracks. At 600 cycle tests, the number of thermal fatigue cracks began to approach, and during 600-800 cycle tests, the number of cracks of all samples increased at a similar rate and tended to be flat. In Fig.4.31b, the number of

cracks in samples A to F varies from more to less, and the number of cracks in samples at each stage is smaller than that in Fig.4.31A. The following results can be obtained from the main crack length results in Fig.4.32A. At the end of the experiment, the main crack length of all samples is basically the same, and the fastest crack growth stage is 600 ~ 800 cycles. When the period is from 200 to 400, the difference of the main crack length between samples is the largest, in which the main crack of sample A is the longest and the main crack of sample F is the shortest. For the bionic sample in Fig.4.32B, the anti-cracking ring plays a great role in preventing cracks due to the small number of thermal cycles at 200 cycles. After that, although the crack continues to expand, the overall crack length is much shorter than that of the untreated sample.

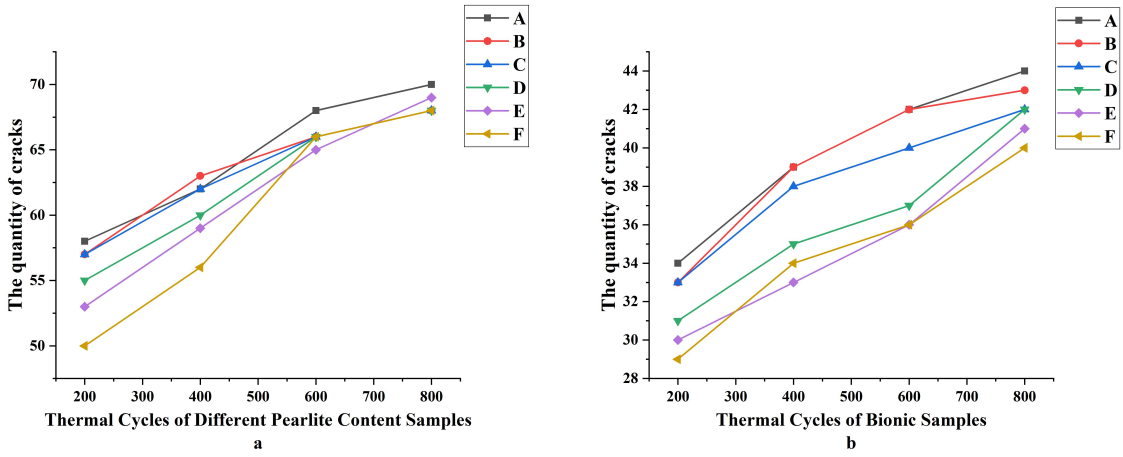


Fig.4.31 The quantity of thermal fatigue cracks of different pearlite contents:(a), untreated samples; (b), bionic samples

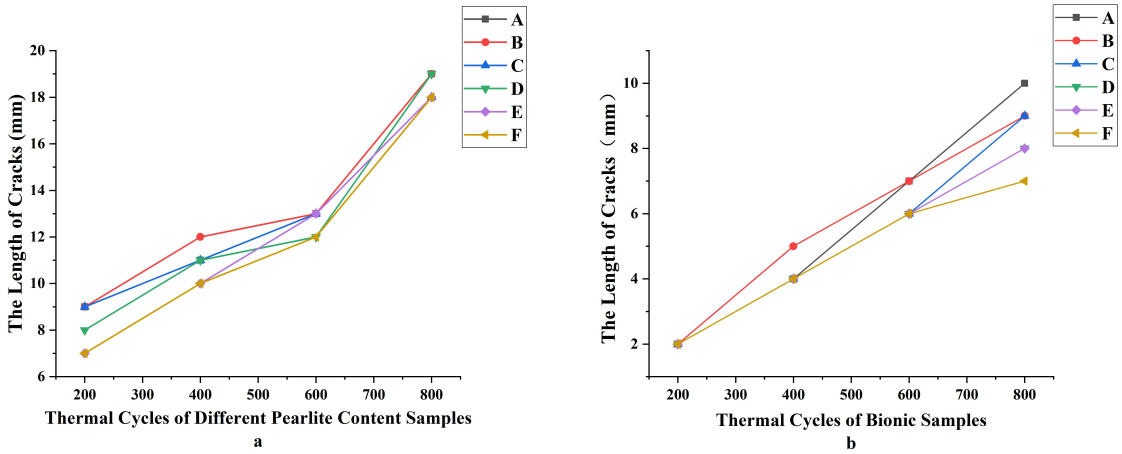


Fig.4.32 The main crack length of different pearlite contents: (a), untreated samples; (b), bionic samples

Thermal fatigue cracks occur due to thermal stress generated by temperature changes, which deforms materials and leads to cracking and even destruction [221]. For grey cast iron, graphite tip is the main crack initiation site due to stress concentration. Cracks start from the graphite tip and grow together with other graphite tip cracks [222]. The pearlite is distributed among the graphite, and due to its high hardness and strength, it can resist the initial small thermal stress. It can be seen from Fig.4.33 that the crack is generated at the graphite tip. Due to the existence of pearlite, crack propagation is blocked, and the direction of crack propagation is affected by the direction of lamellar pearlite, so that the crack has to bridge a longer distance with another graphite. Precisely because of the role of pearlite in the early stage of thermal fatigue test, the number of cracks and the main crack are the least in sample F with 90% pearlite content. At the later stage of the experiment, the crack continued to expand, the pearlite decomposed, the hardness and strength decreased, and many small cracks were connected to form the main crack. Finally, at the end of the test, the main cracks of all samples grew to the limit value.

Since cracks mainly occur at the graphite tip and all the microstructure in the melted zone is dissolved after laser treatment [223], the unit itself limits the initiation of cracks. The thermal fatigue test results of the bionic samples are obviously better than those of the original samples. At the beginning of the experiment, the thermal fatigue cracks were generated at the sample boundary, and the bionic model with an angle of 0° parallel to the sample boundary hindered the crack propagation. With the progress of the experiment, the bionic mesh model not only prevents the crack initiation, but also limits the crack propagation in the mesh.

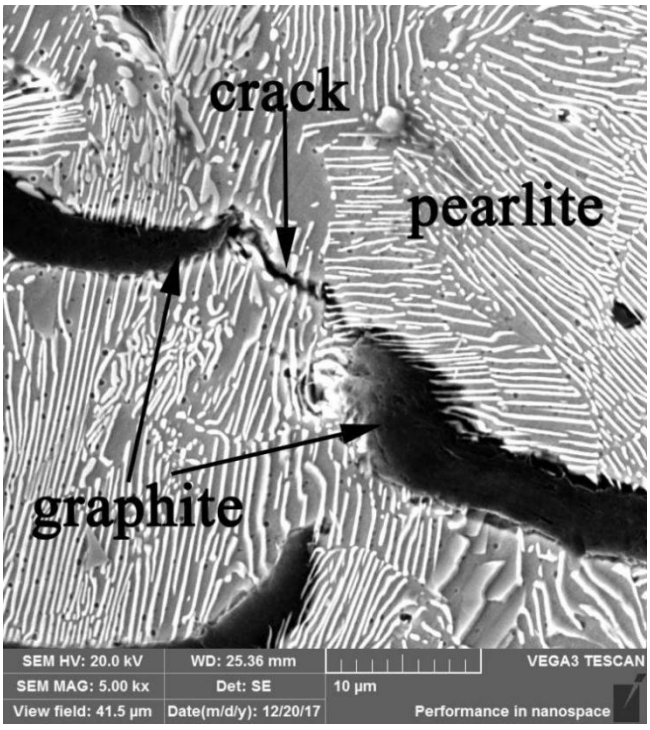


Fig.4.32 Schematic diagram of thermal fatigue crack propagation

4.4.3 Influence and analysis of different pearlite interlamellar spacing on thermal fatigue resistance of samples

The number of cracks and the length of main cracks were observed every 200 times in four samples with different pearlite layers. It can be seen from the results in Fig.4.34A that in 200 cycles, the number of cracks of the four samples in descending order is S1 > S2 > S3 > S4. As the experiment continues, the number of cracks in S1 and S2 is the same, and the number of cracks in S3 and S4 is the same. In Fig.4.34b, the number of cracks of the four samples in each cycle is smaller than that of Fig.4.34A. At the end of the experiment, the number of cracks of S3 and S4 samples is slightly smaller than that of S1 and S2 samples. As for the length of the main crack in Fig.4.35A, it can be seen that, among the 200 cycles, S1 has the longest main crack length, S2 has the second longest extended crack length, S3 is the same as S4, and the shortest main crack length. During 600 ~ 800 cycles, the main crack growth rate is the fastest, and the final main crack length is S1 > S2 > S3 > S4 from long to short. The result of the bionic sample is shown in Fig.4.35B. In 200 cycles, the main crack length of all samples was limited to 2mm. The main crack lengths of S3 and S4 at 800 cycles are smaller than those of S1 and S2, and the main crack lengths of all samples are much smaller than those of the samples in Fig.4.35A.

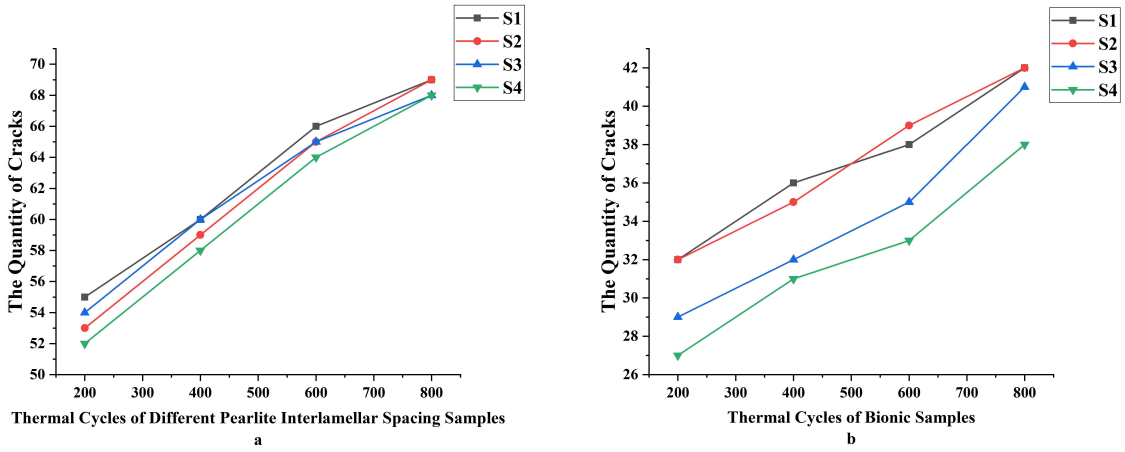


Fig.4.34 The quantity of thermal fatigue cracks of different pearlite interlamellar spacing: (a), untreated samples; (b), bionic samples

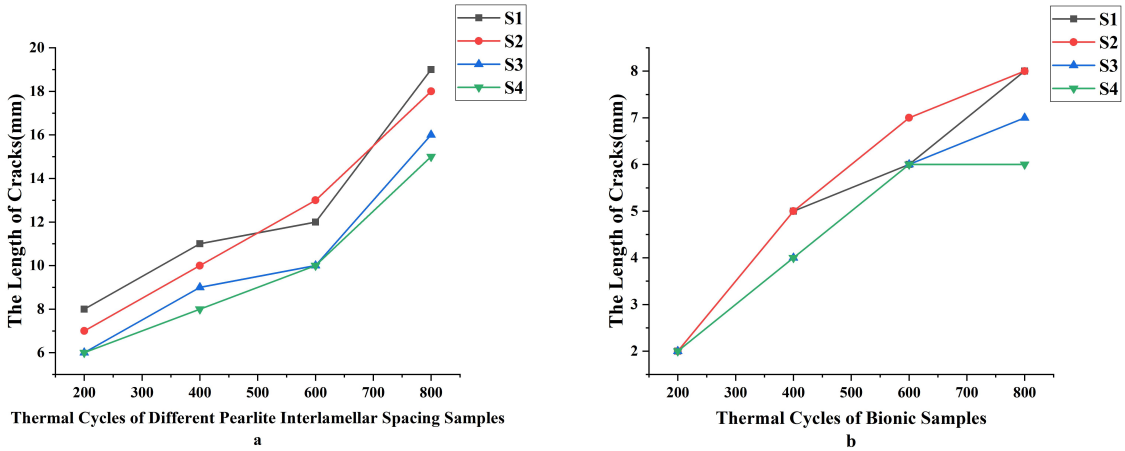


Fig.4.35 The main crack length of different pearlite interlamellar spacing:(a), untreated samples; (b), bionic samples

Since the mechanical properties of the pearlite depend on the interlamellar spacing [32], crack propagation requires more thermal stress to break through the pearlite with smaller interlamellar spacing. Therefore, both the number of cracks and the length of cracks in S3 and S4 with shorter spacing are less and shorter than those in S1 and S2. Compared with the results of samples with different number of pearlite, different interlamellar spacing can better reflect the performance of pearlite. Before 600 cycles, the propagation rate of the main crack is slow, which is related to the fine properties of the pearlite. However, in 600-800 cycles, with the decrease of pearlite content and

the increase of ferrite content, the crack propagation speed is accelerated. Fig.4.36 shows the inhibition effect of bionic coupling unit on thermal fatigue crack. When contacting the unit, the crack first goes through passivation reaction [224]. With the increase of the number of thermal fatigue cycles, the crack bifurcates and deflects in two opposite directions along the boundary of the unit and grows in the original direction where the energy of the crack accumulates.

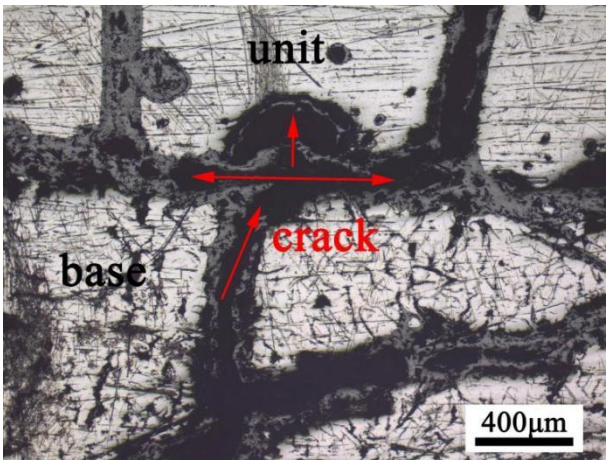


Fig.4.36 Schematic diagram of unit block thermal fatigue crack

4.4.4 Effect of different pearlite content and interlamellar spacing on wear performance

The main failure form of grey cast iron drum brake is thermal fatigue crack, the heat comes from the friction between drum brake and friction pair, so the wear property of the sample must be tested. According to the wear results, the wear weight loss trend of samples with different pearlite content in Fig.4.37A is roughly the same. The weight loss of 200 cycles is inversely proportional to the pearlite content, because the microhardness of the sample with large pearlite content is higher, and the pearlite can

exert specific wear resistance. With the development of thermal fatigue test, the pearlite content decreased and gradually decomposed into ferrite, the hardness and strength decreased, the wear resistance also decreased, and the wear amount increased significantly. By observing the results of the 4.37B bionic sample, the following conclusions can be drawn: the bionic sample is not only effective for thermal fatigue crack, but also can improve the wear resistance of the sample, and the weight loss of the bionic sample is far lower than that of other samples. This is because the stress is mainly distributed on the bionic model with higher hardness, which plays a role in supporting and protecting the rest of the surface.

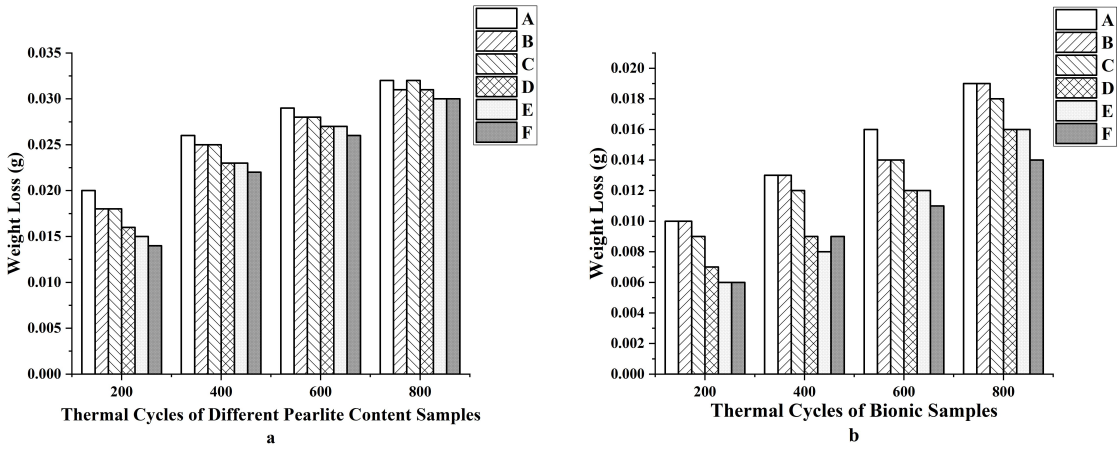


Fig.4.37 Weight loss results of samples with different pearlite contents:(a), untreated samples; (b), bionic samples

As can be seen from Fig.4.38A, S3 and S4 with smaller interlamellar spacing have lower weight loss than S1 and S2, indicating that the sample with smaller pearlite spacing has better wear resistance. Fig.4.38b Results of the bionic sample also follow the same rule, but the weight loss of each sample in each stage is smaller than that of the untreated sample. For the bionic samples, the small pearlite interlamellar spacing

also plays a supporting role in the early stage of the experiment. In general, the wear resistance of the bionic sample is much better than that of the untreated sample. From the results at the end of the experiment, it can be seen that when the effect of pearlite almost disappears, the bionic coupling surface can still improve the wear resistance. At present, the influence of pearlite quantity and interlamellar spacing on thermal fatigue resistance and wear resistance of laser bionic grey cast iron has not been studied, so this study has certain research significance and reference value for industrial application.

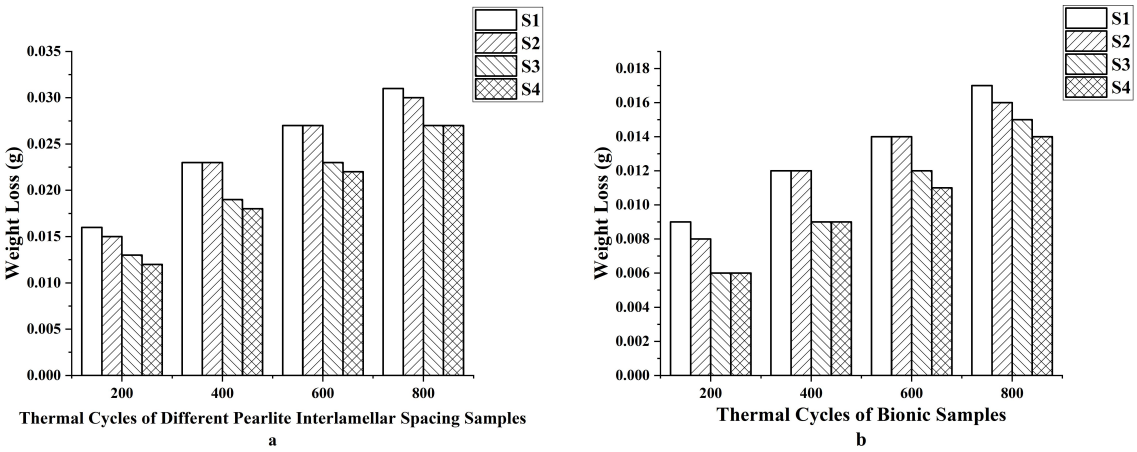


Fig.4.38 Weight loss of different pearlite interlamellar spacing: (a), untreated samples; (b), bionic samples

4.5 Chapter summary

The main casting material of truck drum brake is grey cast iron. Grey cast iron can be divided into many types because of different graphite shapes, different base structures or different solidification modes during casting. This chapter aims to find out the influence law between thermal fatigue resistance and wear resistance of different

types of grey cast iron base metal couplers and laser-prepared coupling bionic units, so as to provide a theoretical basis and reference for the selection of grey cast iron base metal and the application of laser coupling bionic treatment technology in practical production. Within the scope of this research, this chapter has done the following work and drawn the following conclusions:

(1) Using the same laser parameters on the surface of grey cast iron with different graphite types, the coupling bionic units with different microstructures can be obtained. The microhardness of the units is much higher than that of the base with different graphite types, which increases by 151%, 188%, 145%, 199%, 47% from the A-E type. Different graphite types play a decisive role in the initiation and propagation of thermal fatigue cracks. The number of thermal fatigue cracks is the largest in coarse type C graphite and type D graphite with dendrite dendrite density distribution. The main crack length of type D graphite is the longest, and type A graphite has the best thermal fatigue resistance. The thermal fatigue resistance of different graphite bionic samples is better than that of untreated blank samples. The graphite dissolved in the area of the unit, ledeburite, martensite and residual austenite appeared, and the grain was refined, which made the unit have good resistance to the initiation and propagation of thermal fatigue cracks. Among them, the thermal fatigue resistance of type D graphite bionic sample is improved the most, and the thermal fatigue resistance of type C graphite bionic sample is the worst.

(2) The wear performance of different graphite bionic samples is better than that of

untreated blank samples. The higher hardness of the unit area plays a supporting role in the wear process to improve the wear resistance of the sample. Among them, the type C blank graphite sample has the best wear resistance, the type D blank graphite sample has the worst wear resistance, and the type D graphite in the bionic sample has the most improved wear resistance. With the increase of the number of thermal cycles, the structure of the base and the unit changes, and the hardness and wear resistance gradually decrease.

(3) The graphite type of the control sample is type A when the grey cast iron with different carbon content is studied. The higher the carbon content of the sample, the weaker the oxidation resistance of grey cast iron in the thermal cycling process. The increase of the oxide layer thickness can promote the initiation and expansion of thermal fatigue cracks. The thickness of the oxide layer of the bionic sample decreases by 54%, 45%, 40% and 35% in turn. The higher the carbon content in the bionic sample, the higher the hardness of the unit, and the slower the growth rate of the number of thermal fatigue cracks. With the increase of the number of thermal cycles, the unit is easy to crack due to the higher hardness, and the resistance effect of the bionic sample with higher carbon content to thermal fatigue crack growth decreases.

(4) For the samples with different carbon content of type A graphite, the hardness of grey cast iron plays a decisive role in the wear test after thermal fatigue. The higher the carbon content, the stronger the lubrication effect of graphite in the wear process, the higher the hardness of base metal and the better the wear

resistance. For the bionic sample, the higher the carbon content, the higher the hardness of the unit, the better the wear resistance. The thermal fatigue cracks and graphite pits in the thermal fatigue test have great influence on the wear resistance of the sample. The unit can reduce the effect of defects on the wear property of grey cast iron.

(5) The greater the pearlite content, the better the thermal fatigue resistance and wear resistance, and the smaller the interlamellar spacing, the better the thermal fatigue resistance and wear resistance. With the thermal fatigue experiment, the pearlite will gradually decompose, and the pearlite function will gradually disappear in the later stage of the experiment. Due to the presence of ledeburite, martensite and residual austenite in the laser melted zone, the laser melted zone has better structure than the base and thus higher hardness. The thermal fatigue resistance and wear resistance of the bionic samples are better than those of the untreated samples. For the untreated and bionic samples, the best thermal fatigue resistance and wear resistance are obtained when the pearlite content is 98% and the pearlite interlamellar spacing is 152nm. After laser treatment, the influence of pearlite is reduced, and the experimental results of each sample are less different, and the performance of the bionic sample is better than that of the untreated sample.

Chapter 5: Influence of Morphological Coupling Characteristic Quantity on Thermal Fatigue and Wear Resistance of Grey Cast Iron Truck Drum Brake and Design of Coupling Bionic Model

5.1 Introduction

The laser parameters suitable for machining the coupling unit of high-quality structure on the surface of truck drum brake are obtained through orthogonal test. Then, the influence of the base material coupling element on the thermal fatigue resistance and wear resistance of the bionic grey cast iron truck drum brake is analyzed. And the preparation of coupling bionic unit provides a strong theoretical basis and basic research data. Based on the above research, a coupling bionic unit can be prepared by laser on the brake surface of a specific grey cast iron, which can improve its performance. However, the core of coupling bionic is that organisms in nature evolve corresponding characteristics to cope with their surroundings in order to adapt to different environments or complex conditions. Therefore, organisms in nature have diversity and specific characteristics. Also for the coupling bionic technology of laser processing technology, although the optimization of the laser processing parameters to the preparation of quality structure coupling element unit, and the base metal coupling element also studied the influence of bionic technology, but how to according to the requirements and characteristics of drum brake, the bionic coupling unit model of representational be arranged according to certain rule, to maximize the advantages of coupling bionic technology becomes the focus of the next research. In recent years,

most of the related studies use a single model composed of a single morphological coupling element characteristic quantity to prepare on the material surface. The single model obviously cannot meet the failure characteristics of truck drum brake. Therefore, the main contents of this chapter are as follows: according to the failure characteristics of grey cast iron drum brake with non-uniform regional damage, referring to biological prototypes such as shells and leaves, and combining with actual laser processing conditions, a bionic model of double combination coupling elements with different morphological coupling element characteristic quantities is designed. Double combination model as its name implies is to two forms coupling characteristic of a single model combination, so first of all, through the thermal fatigue and wear test, and Ansys finite element analysis of single model and untreated sample test and equivalent stress analysis, comparison with different spacing and the angle of two kinds of single model of the characteristics of the experimental results, and according to actual needs, drum brake to select the characteristics of a single model after the combination, design of the double combination model, the same to heat fatigue test, equivalent stress wear test and Ansys simulation results, finally be applied to bionic coupling model of grey cast iron drum brake, for the practical production and application of laser coupling bionic processing provides technical reference and theoretical basis.

5.2 The Influence and Analysis of Morphological Coupling Characteristic Quantity on Thermal Fatigue and Wear Resistance of

Samples

The characteristic quantities of morphological coupling elements of the laser - fabricated coupling bionic model is mainly divided into two types: spacing and angle. This chapter mainly studies the model of stripe coupling bionic unit composition with different spacing and different angles, conducts thermal fatigue and wear tests, analyzes the equivalent stress distribution of each model with Ansys finite element software, and compares the thermal fatigue and wear resistance of different models. According to the characteristics of grey cast iron drum brake with regional failure, a single model suitable for different regions of drum brake is selected to provide a basis for the design of the subsequent double combination model.

5.2.1 Influence and analysis of morphological coupling element distribution spacing characteristic quantity

This section of laser processing parameters was optimized by using the above in grey cast iron sample preparation quality coupling surface bionic unit, design as the only variable distribution with different element spacing stripe single bionic coupling model, compared with a blank sample, research unit spacing distribution of the law and the influence of thermal fatigue and wear resistance.

Fig.5.1 is the schematic diagram of samples with different spacing characteristics and blank samples. According to the figure, the coupling bionic model is processed on the surface of $40\times20mm^2$, which is the grinding surface with the friction pair. The stripe

model used to study the characteristic quantity of unit distribution spacing is at an angle of 90° with the wear direction, and the spacing refers to the distance between the light spots during laser processing. Since the width of the unit processed by the laser parameters is 1mm, the spacing presented on the sample surface is the distance between the center points of each unit as shown in the figure. The spacing of samples (a) - (f) used in the test is 2mm, 3mm, 4mm, 5mm, 6mm, and a blank sample, respectively. If the spacing is 1mm, it indicates that the units belong to the phase state, which means that the units will cover the whole surface. This part will be explained and analyzed later. In addition, the material of the unit is defined as: density, 7850kg/m^3; Poisson's ratio, 0.3; Young's modulus, 2×10^5; Tensile yield strength, 250MPa; Compressive yield strength, 250MPa.

In this test, the area of the unit contained on the surface of the sample is defined as S_u, the surface area of the laser processing surface of the sample is S_a, and the area ratio of the unit is defined as P_u. The calculation formula of area ratio of unit can be expressed as:

$$P_u = \frac{S_u}{S_a} \quad (5.1)$$

According to Formula 5-1, it can be calculated that the surface area ratio of sample units with different spacing characteristics in Fig.5.1 is 50%, 35%, 25%, 20% and 17.5% respectively. The area ratio of the unit of the blank sample, P_u, is 0%.

Firstly, the thermal fatigue test was carried out on the samples with different spacing characteristics, and the test was suspended after every 200 thermal cycles. The

number of thermal fatigue cracks and the length of the main crack on the laser-processed surface were observed and recorded after the samples were taken out and cleaned. The experimental results are shown in Fig.5.2. It can be seen from Fig. 5.2a that the number of thermal fatigue cracks in the blank sample is far more than that in the bionic sample at each stage. The growth rate of thermal fatigue cracks in the bionic sample is similar, which increases with the increase of the number of thermal cycles and shows a law that the larger the distance between the stripe units, the more thermal fatigue cracks there are. That is, the thermal fatigue cracks of the sample with a spacing of 2mm and a surface area ratio of 50% of the unit are the least at each stage, except for the blank sample with a spacing of 6mm and a surface area ratio of 17.5% of the unit are the most at each stage, and the number of thermal fatigue cracks decreases by 43%, 39%, 34%, 31% and 28% successively. Fig.5.2b is the sample as a result, the crack length by a figure the all sample main crack growth rate, relatively stable before 600 times thermal cycling, the rate increased by 600 times, blank samples of main crack length is greater than the bionic samples, including spacing characteristic quantity for 2 mm sample thermal fatigue of the main crack length in the process of the thermal cycle is the shortest, The main crack length of 6mm sample is the longest, and the thermal fatigue crack growth rate decreases by 42%, 37%, 26%, 18%, and 13%, respectively.

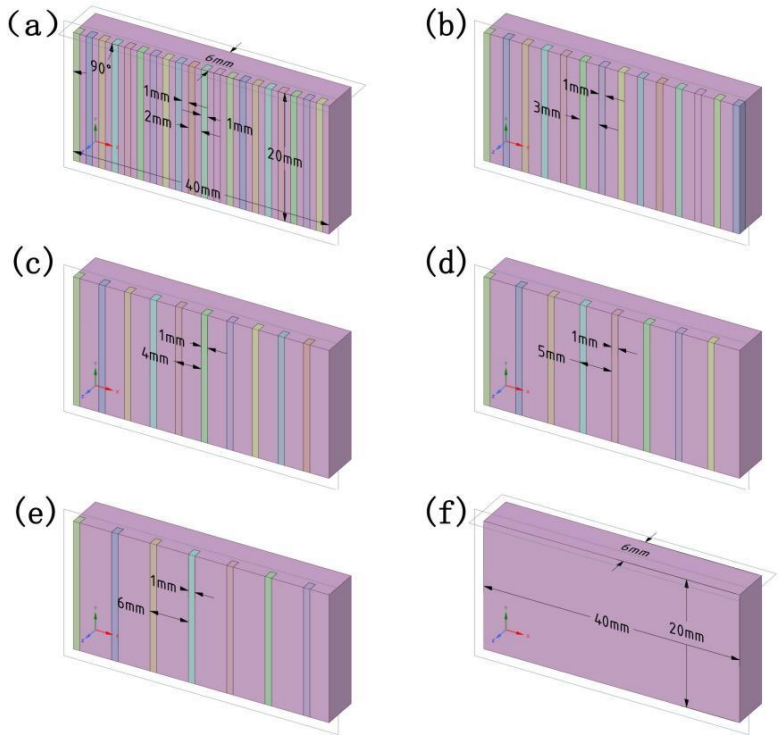


Fig.5.1 Schematic diagram of samples with different spacing characteristics and blank samples

Because there is no unit on the blank sample surface, the thermal fatigue crack is not hindered, and the number and length of cracks are the largest in all samples. Fig.5.3 shows the propagation of thermal fatigue crack in the model with different spacing characteristic quantities. As can be seen from the arrow direction in the figure, the crack mainly starts from the edge of the sample, and the crack begins to expand to the center of the sample with the increase of the number of thermal cycles. Due to the different spacing, the area for thermal fatigue crack growth is also different. When the spacing between the two units is relatively large, the crack has enough space to expand and will not be hindered by the units, while the base area is small when the spacing between the units is small. With the increase of thermal cycle times, the crack initiated at the edge first touched the unit with 2mm spacing, and then the crack

gradually touched the unit with other spacing characteristics, so the length of the main crack was different. However, for the model perpendicular to the wear direction, the crack propagating from the short side of the sample has the hindering advantage, while the crack initiated from the long side of the sample has the hindering disadvantage. Only when the growth direction of the crack changes and the wear direction of the unit is 90° angle will hinder it. At the same time, this also explains that the main crack length of the bionic sample is not too large as the gap between the number of cracks and the blank sample.

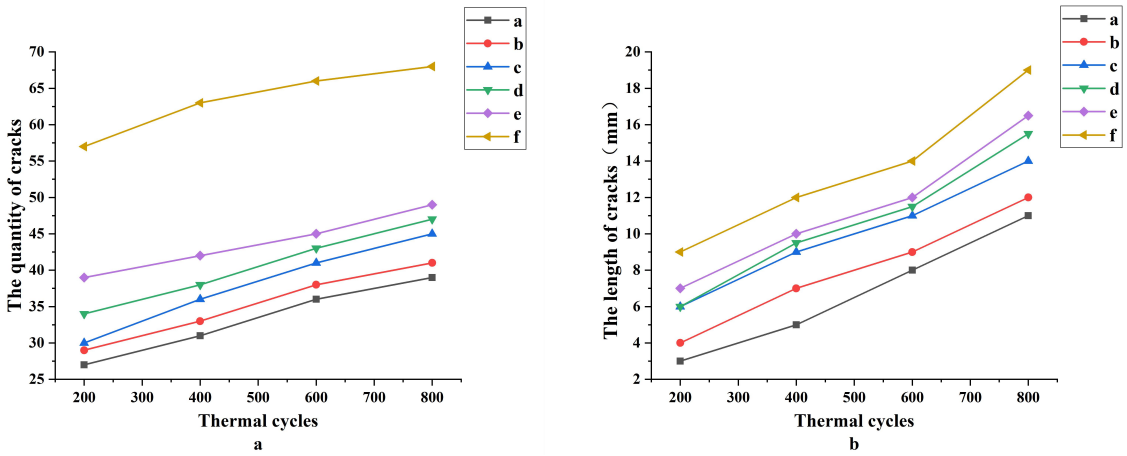


Fig.5.2 Thermal fatigue test results of samples with different spacing characteristics :(a), the quantity of thermal fatigue cracks; (b), length of thermal fatigue main crack

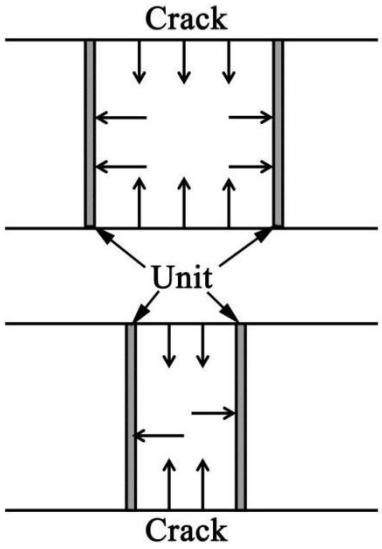


Fig.5.3 Schematic diagram of thermal fatigue crack propagation on samples with different spacing characteristics

Fig.5.4 for different spacing of sample after the thermal fatigue characteristics of grinding weight loss as a result, the overall weightlessness regularity of all samples for thermal cycle, the more the more weight loss after the thermal fatigue wear, including blank sample in each stage of weight loss is the most, the bionic sample weight loss results, first decreases increased like parabolic trend. In the early stage when the number of thermal cycles is small, the number of thermal fatigue cracks on the sample surface is small, and the impact of cracks on wear resistance is mainly from the properties of the unit and the sample itself. It can be seen from the figure that the wear loss weight of the 2mm spacing characteristic sample is the largest except for the blank sample at 200 thermal cycles, and the wear loss weight of the 6mm spacing characteristic sample becomes the largest except for the blank sample at the beginning of 400 thermal cycles. In addition, according to the results of weight loss of samples

with different spacing characteristics, the weight loss of bionic samples is not much different from that of blank samples. The reason for this result can be analyzed by combining the finite element simulation results.

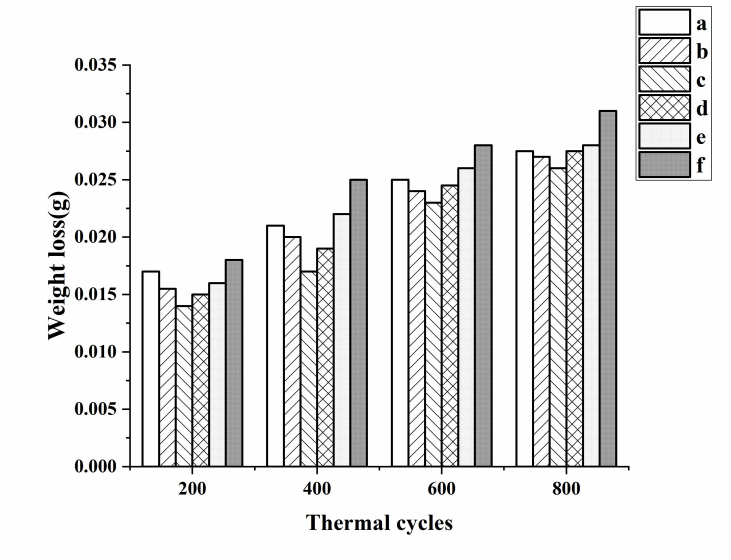


Fig.5.4 Wear weight loss of samples with different spacing characteristics

Fig.5.5 and Fig.5.6 show the equivalent stress simulation results of wear path and wear surface, respectively. The closer the figure is to red, the larger the stress value, and the closer it is to blue, the smaller the stress value. Since the friction direction of the wear test is fixed, a path with the same friction direction is drawn during the finite element simulation, and the equivalent stress distribution on this path is simulated. The equivalent stress values of the samples with different spacing characteristics and blank samples on the wear path are compared. At the same time, the finite element analysis of the whole wear surface is carried out to obtain the equivalent stress distribution results of the sample surface, to analyze the difference of wear resistance.

Fig.5.5 shows the equivalent stress distribution diagram of wear paths of samples with different spacing characteristic quantities and blank samples. The abscissa of the stress curve on the right of the figure is the distance from the left side of the path to the right side of the sample, and the ordinate is the stress value. It can be seen from the figure that the stress peaks all appear on the stripe unit, but the distribution is uneven. For the sample unit surface stress of 2mm spacing is between 0.053 and 0.063MPa, and for the sample unit surface stress of 3mm spacing is between 0.057 and 0.068MPa. 4mm spacing sample unit surface stress value in 0.066~0.069MPa, 5mm spacing sample unit surface stress value in 0.063~0.068MPa, 6mm spacing sample unit surface stress value in 0.057~0.068MPa, blank sample surface stress edge stress value is larger, the internal stress value is small, and the distribution is parabolic. It can be concluded that, for the bionic sample, the wear stress is mainly concentrated on the surface of the unit, and the unit as the hard phase bears most of the stress, which plays a protective effect on the base material. The stress on the edge of both sides of the wear path of the blank sample is the largest, which confirms the stress concentration at the edge of the sample. The stress distribution of the sample units with different spacing characteristics is not the same. In the sample with 2mm spacing, 7 units bear more stress, while the surface stress values of the other units are different, and the stress peak value is the lowest in the bionic sample. In the sample with 3mm spacing, four units bear more stress, and the surface stress values of all units differ greatly. The stress of the unit with 4mm spacing is the most average, the difference of stress values is the smallest, and the stress peak value is the highest, indicating that

the unit bears most of the surface stress. In addition to the 5mm spacing sample edge unit outside the rest of the unit surface stress is more average, the stress difference is small; For the sample with a spacing of 6mm, only two units bear more stress, and the surface stress values of the units differ greatly. On the wear path, the difference between the unit and the base is 4mm > 3mm > 6mm > 5mm > 2mm in descending order. Fig.5.6 for different spacing characteristic sample and blank sample surface equivalent stress distribution as a result, it can be seen that the bionic surface mainly undertakes the sample unit stress, while 2 mm spacing of sample unit of sample surface area ratio most, but the unit surface stress and base stress difference in bionic sample minimum, stress of the blank sample are mainly concentrated on the edge of the sample.

Considering that the experimental conditions of all samples are consistent, the stress value on the surface of the samples is certain. According to the results of finite element analysis, when the unit bears more equivalent stress, the base material bears less stress. Therefore, it can be judged that the smaller the spacing characteristic quantity is, the better the result will be. When the distance between two unit is 2 mm, the unit on the surface of the unit surface equivalent stress and equivalent stress difference on the surface of the substrate is the smallest of bionic sample surface stress value and the unit is not average, at the same time on the worn path unit and base differential stress value is the smallest, means that the stress value in the base under bionic is one of the biggest in the sample, Therefore, it is explained that the weight loss of 2mm spacing sample is the highest in the wear test after 200 thermal

cycles. With the progress of the thermal fatigue test, the influence of thermal fatigue cracks on wear in the later stage of the thermal cycle becomes greater. The samples with larger spacing of units have more thermal fatigue cracks on the surface, which leads to the larger weight loss growth rate of 5mm and 6mm spacing in the later stage of the test. However, for the sample with 4mm spacing, the equivalent stress value of the unit is the most average, and the stress difference between the unit and the base material is the largest, so the weight loss from grinding is the least.

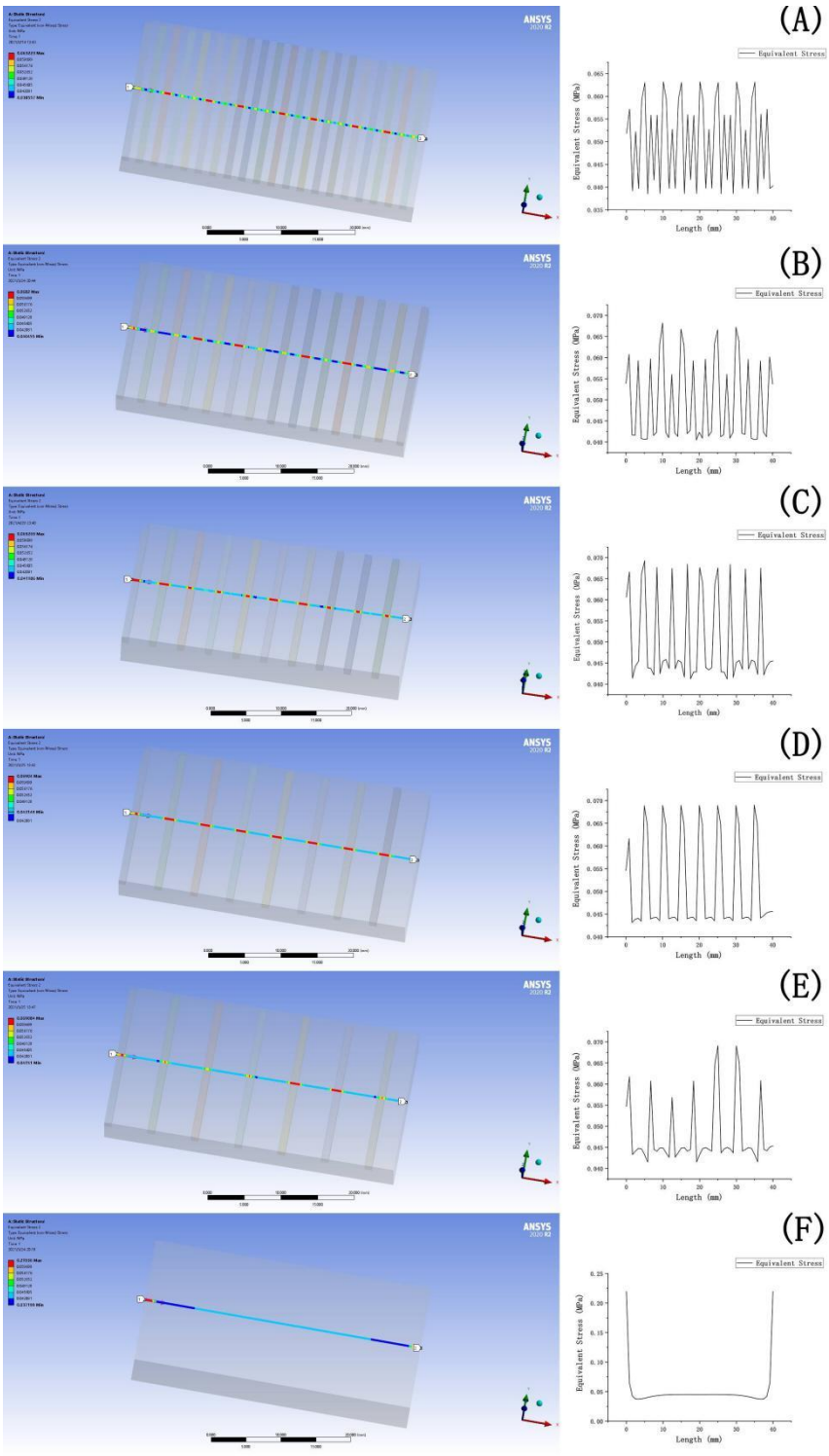


Fig.5.5 Equivalent stress distribution of wear path of samples with different spacing characteristics

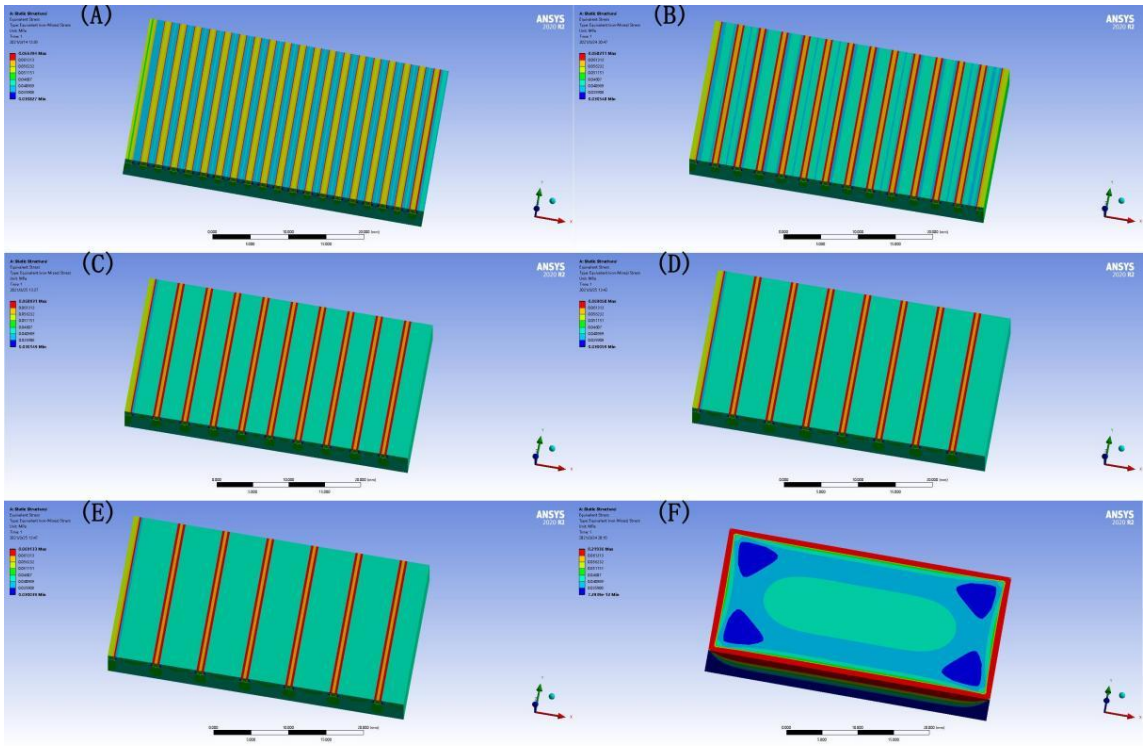


Fig.5.6 Surface equivalent stress distribution of samples with different spacing characteristics

When designing the coupling bionic model above, it is mentioned that the sample surface is prepared as a full unit. In this study, Ansys finite element analysis is conducted on the full unit sample, and the results are shown in Fig.5.7. Similarly, a path is drawn in the sample wear direction to detect the equivalent stress distribution on the sample surface and the wear path. It can be seen from the figure that when the sample surface is full of units, the equivalent stress distribution result on the surface is similar to that of the blank sample in Fig.5.6, with the stress mainly concentrated at the edges around the sample. The stress distribution on the wear path is also like that of the blank sample, with the maximum stress at the edges on both sides of the path.

To sum up, in order to give full play to the excellent performance of the coupling bionic model in thermal fatigue and wear tests, meet the requirements of thermal

fatigue and wear resistance of the drum brake according to the special failure characteristics of the drum brake, reflect the characteristics of the coupling bionic unit, take into account the production efficiency in practical application, and combine the experimental results above, The stripe unit spacing with a spacing characteristic quantity of 4mm was selected as the spacing between the two unis of the following model with different angles.

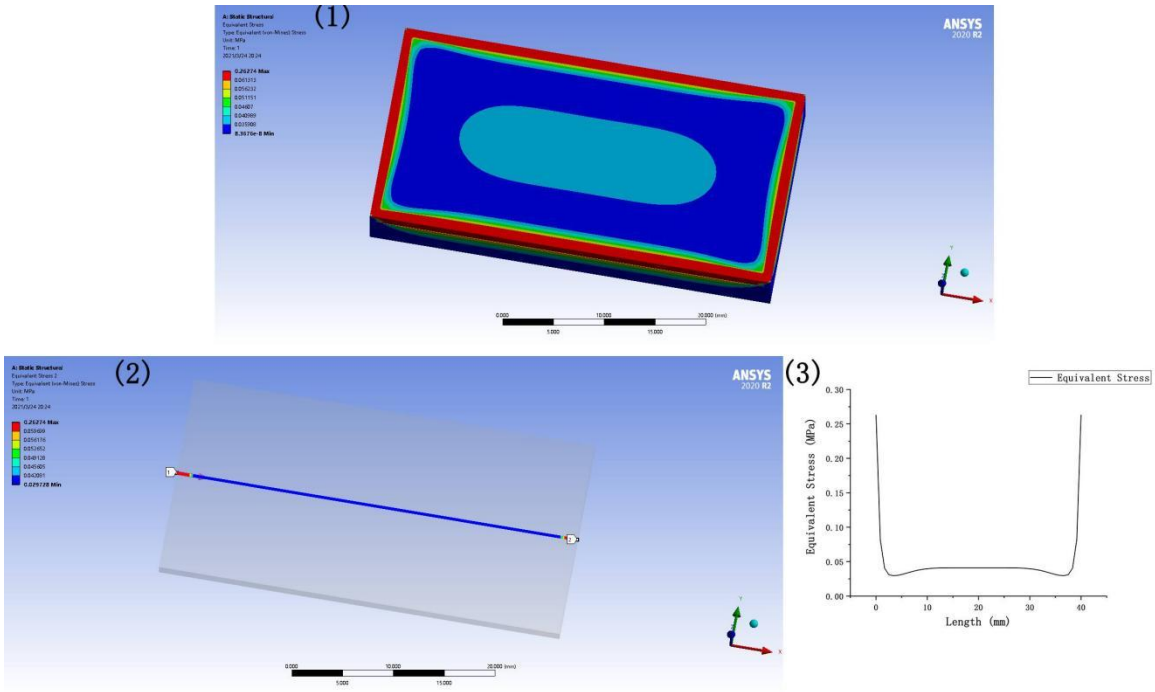


Fig.5.7 Equivalent stress distribution of full units on sample surface

5.2.2 The influence and analysis of morphological coupling element distribution angle characteristic quantity

After obtaining the optimized laser parameters, the next step is to design the bionic coupling model according to the requirements of the drum brake. The main failure mode of the drum brake is thermal fatigue crack through the top, and the heat comes

from the friction between the drum brake and the friction pair. The failure of drum brake is characterized by regional failure. Therefore, a single model cannot give full play to the advantages of coupling bionic. The influence of the spacing characteristic quantity on the thermal fatigue and wear resistance of the coupling bionic model was studied. Then it is necessary to study the influence of angle characteristic quantity on the single bionic coupling stripe model. Therefore, a single model and blank samples with 0°, 30°, 45°, 60° and 90° angles with (a) - (f) spacing of 4mm were designed for thermal fatigue and wear experiments after thermal fatigue. Samples with different angle characteristic quantities are shown in Fig.5.8. Since only the angle of the coupling bionic surface is the only variable, the long side of 0° angle and the wide side of 90° angle should be processed into a stripe model respectively, so that the surface area ratio of the coupling bionic unit is almost equal. In addition, the vertical distance between each unit in the model is 4mm, and the coupling bionic model of all samples is processed on the surface of $40\times20mm^2$.

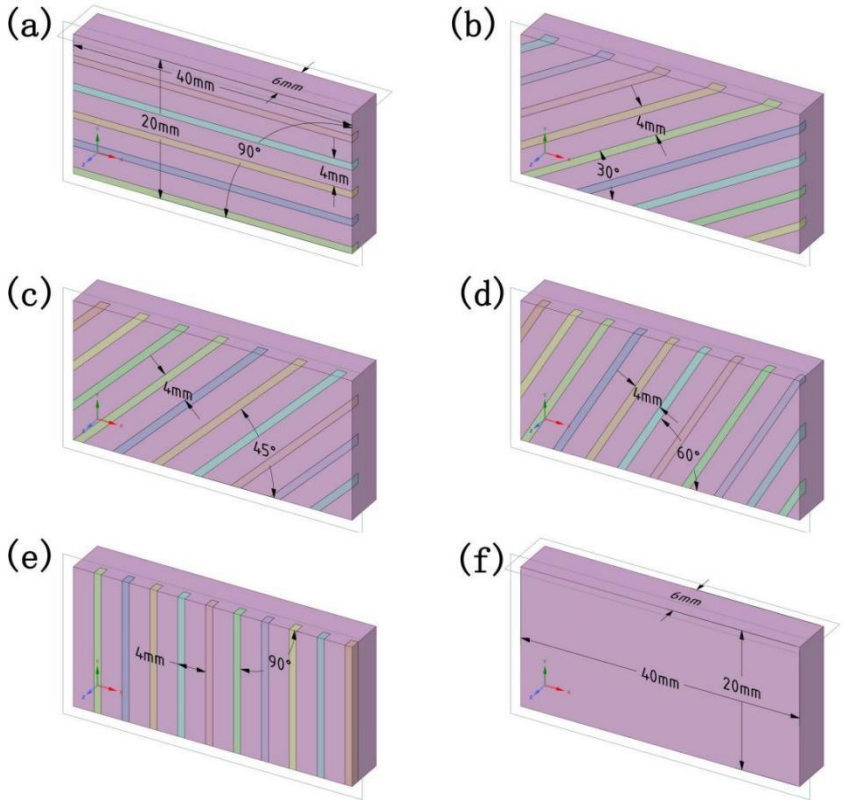


Fig.5.8 Schematic diagram of characteristic samples and blank samples from different angles

The thermal fatigue test result is to judge the thermal fatigue performance of the sample by observing and recording the number of cracks and the length of the main crack. Fig.5.9 shows the thermal fatigue test results of the single coupling bionic sample and blank sample with different angle characteristic quantities. The results of bionic coupling samples at each stage are obviously better than those of blank samples. Before 600 cycles in Fig.5.9A, the number of cracks in the 0° angle model and the 90° angle model decreases, while the number of cracks increases in the final stage. This is because the crack initiation mainly comes from the edge of the sample. Since the long side and wide side of the 0° angle model and 90° angle model are processed with one unit respectively, these two samples have fewer cracks than other

samples in the early stage of the test. The cracks of the 0° angle model and the 90° angle model began to grow at the late stage of the test. According to Fig.5.10 (a), this was because the 0° angle model had a disadvantage on the short side, and the 90° angle model had a disadvantage on the long side. The initiation and propagation of cracks in the middle of the two units were not hindered. In addition, among all the bionic samples, the 30° angle model has the largest number of cracks, which is due to the limited number of long side units in this model, while the 60° angle model has no advantage in the wide side. Before 600 cycles, the number of cracks in the 45° angle model is only lower than that in the 0° angle model and the 90° angle model. After 600 cycles, the number of cracks in the 45° angle model is the least at the end of the experiment due to the advantages of the long side and short side of the sample, and the number of thermal fatigue cracks decreases by 32%, 32%, 37%, 35% and 34% successively.

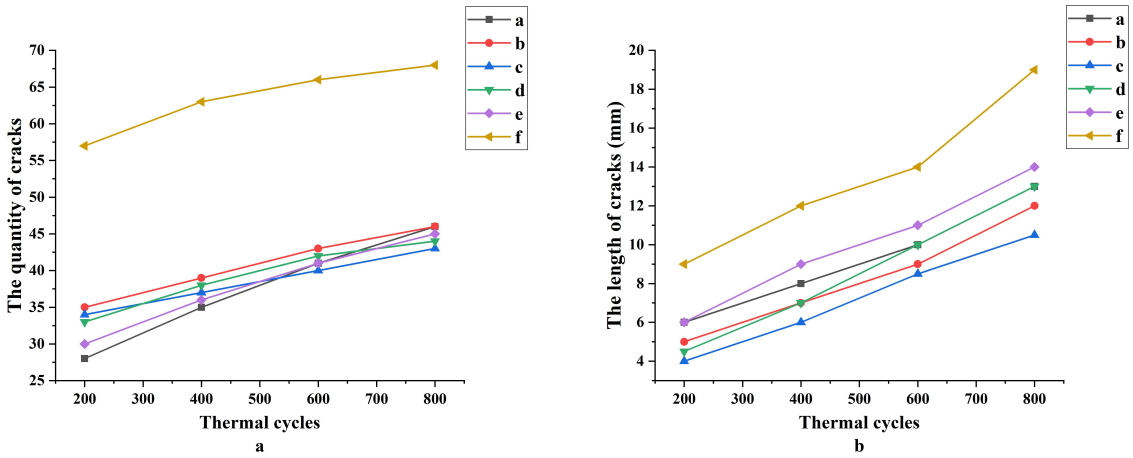


Fig.5.9 Thermal fatigue test results of samples with different angle characteristic:(a), the quantity of thermal fatigue cracks; (b), length of thermal fatigue main crack

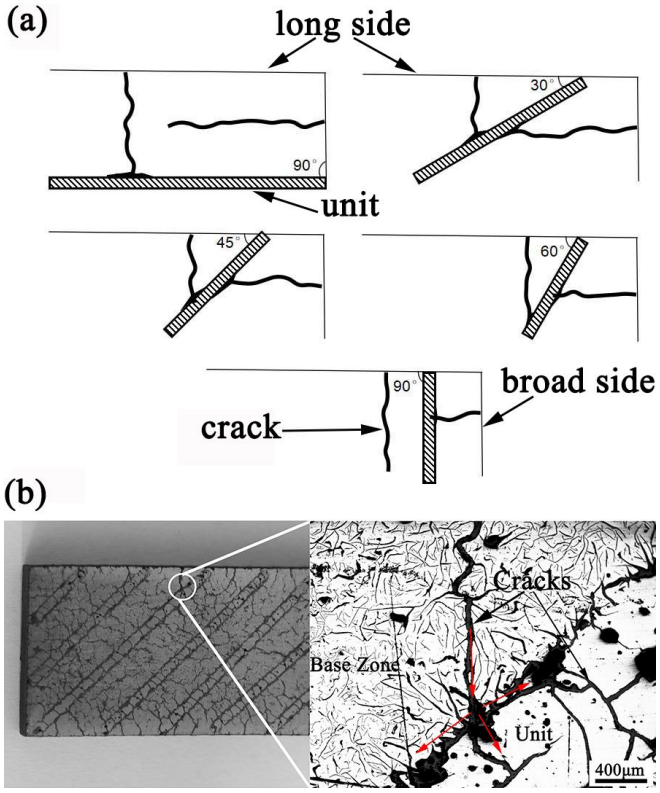


Fig.5.10 Schematic diagram of thermal fatigue crack propagation on samples with different angle characteristic

Fig.5.9b shows the main crack length of all samples at each stage. The main crack length of all bionic samples is much smaller than that of blank samples. The growth trend of the main crack in all samples is similar, and it increases with the increase of thermal cycling. Among all the bionic samples, the 90° angle model has the worst crack suppression performance, followed by the 60° angle model. The 45° angle model is the best, followed by the 0° angle model, and the thermal fatigue crack growth rate decreases by 31%, 37%, 45%, 32%, 26%, respectively. The laser bionic coupling model at the stage of inhibiting crack growth is shown in Fig.5.10b. The crack grows in two ways after encountering the unit. One is along the boundary between unit and base; The other is through the unit. It can be seen from the figure that the former effectively changes the direction of crack propagation; In the second

way, the crack needs to accumulate more energy through more thermal fatigue cycles to break through the unit.

The weight loss after thermal fatigue is shown in Fig.5.11. The weight loss of blank samples was the highest in each thermal cycle. The weight loss of the 60° angle model is similar to that of the 90° angle model, which is only smaller than that of the blank sample. In the early stage of the test, the weight loss of the 0° and 30° angle models was always smaller than that of the 45° angle model, but the 45° angle model finally had the smallest weight loss. The difference between thermal fatigue wear and conventional wear mainly lies in the influence of thermal fatigue cracks on wear properties. With the increase of the number of thermal fatigue cycles, the number of cracks on the surface of the sample increases and increases, and the abrasive particles are easy to accumulate in the cracks, and the abrasive particles wear and form grooves in the base. As shown in Fig.5.12, there is a large amount of abrasive debris in the crack, and the furrow through the crack is significantly deeper. The overall wear resistance of the bionic sample is better than that of the blank sample due to the good supporting function of the coupling bionic unit [225], as well as the obstruction and dispersion effects [155].However, due to the different angle characteristics of the coupling bionic model, the hindrance to the thermal fatigue crack is different, resulting in the number of thermal fatigue cracks and the length of the main crack are different, which directly leads to the different weight loss and wear resistance of samples with different angle characteristics.

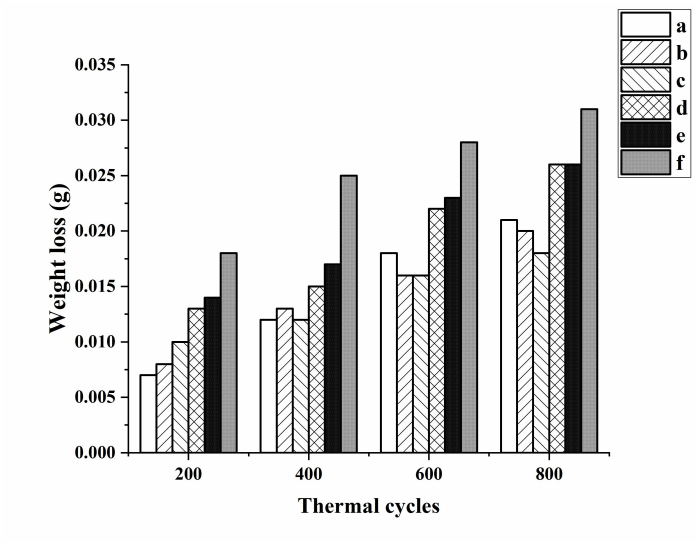


Fig.5.11 Wear weight loss of samples with different angle characteristic

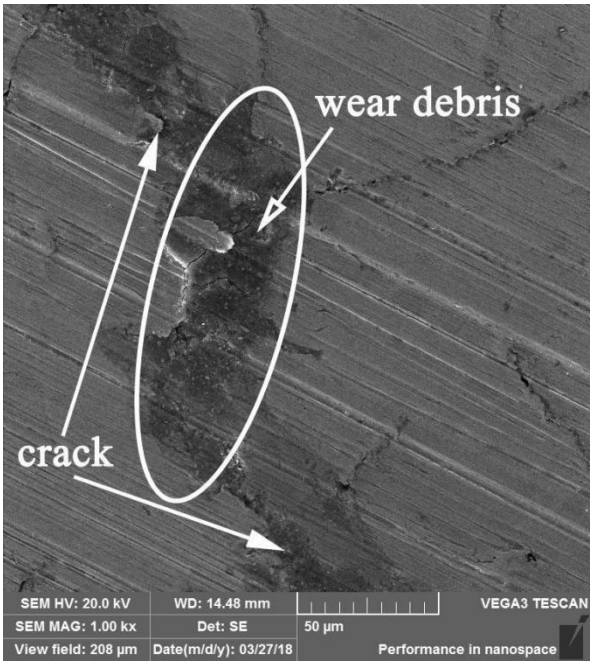


Fig.5.12 Schematic diagram of thermal fatigue crack effect on wear

Fig.5.13 shows the equivalent stress distribution diagram of sample surface with different angle characteristic quantities and blank sample surface. In the figure, the redder the color is, the larger the stress value is the bluer the color is, the smaller the stress value is. The stress value of the legend boundary in each picture is the same.

Since the unit on the surface of the bionic sample occupies basically the same surface area ratio and the surface pressure is the same, it can be judged from the results in the figure that the unit surface of the 45° angle sample has the largest equivalent stress value, indicating that the 45° angle model can bear the most stress in the wear process and can play a good supporting role. At the same time, the unit has high hardness and better wear resistance than the base material. It can bear more stress to protect the relatively soft base material and improve the wear resistance of the whole sample. For the blank sample, it can be seen that the stress is mainly concentrated at the edge of the surface, and the stress concentration at the edge is easy to initiate cracks, while the bionic sample concentrates the stress on the unit, which not only hinders the thermal fatigue crack, but also hinders and disperses the abrasive particles during the wear process. In conclusion, the coupling bionic model with a 0° angle to the thermal fatigue crack growth direction has the strongest performance in thermal fatigue crack resistance, and the coupling bionic model with a characteristic quantity of 4mm spacing and 45° angle has the most for the improvement of thermal fatigue resistance and wear performance of grey cast iron.

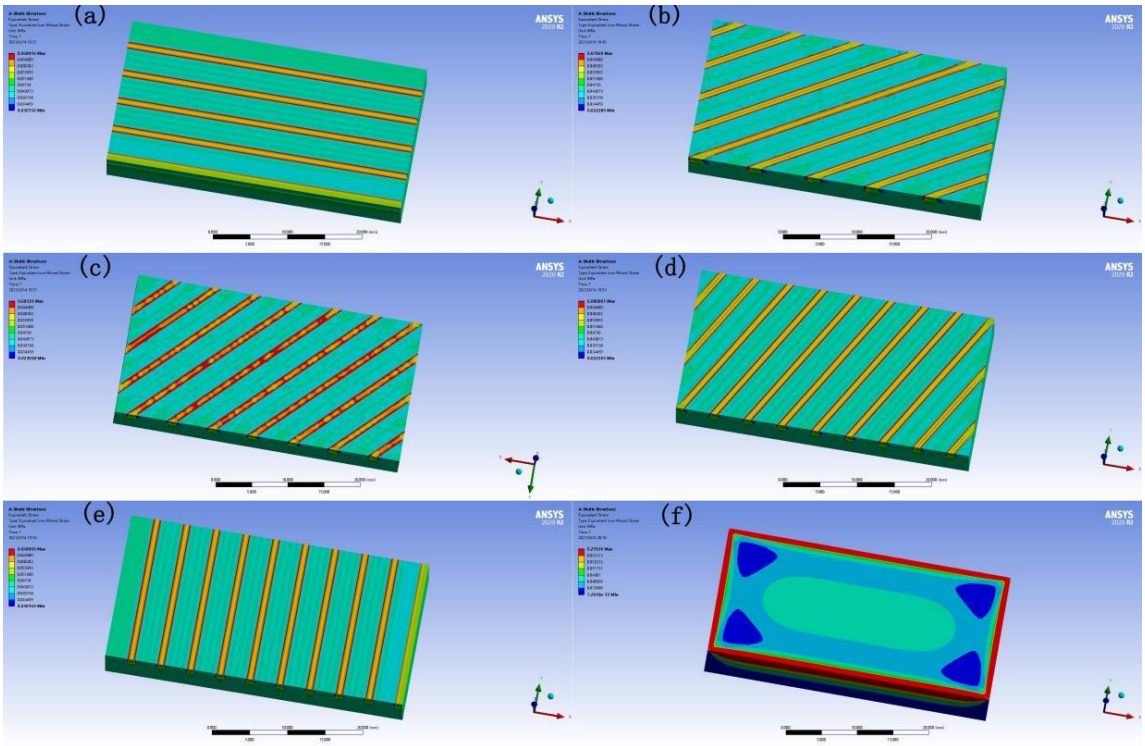


Fig.5.13 Surface equivalent stress distribution of samples with characteristic from different angles

5.3 Double Combination Coupling Bionic Model Design

The spacing and angle of the coupling bionic model were studied respectively above. Finally, it was found that the unit of 0° angle characteristic quantity had the strongest hindrance to thermal fatigue crack, and the sample of the coupling bionic model with 4mm spacing characteristic quantity and 45° angle characteristic quantity had the best thermal fatigue and wear resistance. Due to destruction of grey cast iron drum brake is non-uniform regional failure characteristics of thermal fatigue crack perpendicular to the growth characteristics of the drum brake wall, in order to improve the service life of the drum brake, according to the above research results, this chapter after selection of the characteristic according to the demand for a single, double composite coupling bionic design model designed to improve thermal fatigue and wear resistance of drum

brake. During the test, the thermal fatigue cracks of grey cast iron samples start from the boundary and grow perpendicular to the boundary to the center, which is similar to the growth direction of the thermal fatigue cracks on the inner wall of drum brake. Therefore, this chapter is designed to connect with the unit stripes parallel to each side in turn, which is called the anti-crack ring, which hinders the expansion of thermal fatigue cracks to the greatest extent. In processing the anti-crack ring, the laser spot is located at 2 mm sample edge, the reason is that in the final model characteristic need to make sure that each sample unit surface of sample surface area than similar, and sample the edge stress concentration, if the unit system ready on the edge of the sample, prone to rupture, cracks unit itself it may hinder crack initiation to a certain extent but lose the ability to hinder crack propagation.

5.3.1 Influence and analysis of characteristic quantities with different distribution spacing

In this chapter, the laser parameters optimized above are used to design a bionic model with the coupling of anti-crack ring and different spacing characteristic quantities. Compared with blank samples, the influence law of spacing characteristic quantities on the thermal fatigue and wear resistance of the dual combination model is studied.

Fig.5.14 shows the schematic diagram of the double combination model and blank sample with different spacing characteristics. According to the figure, the double combination coupling bionic model is processed on the surface of 40×20mm^2. The

spacing characteristic quantity refers to the distance between the light spots during laser processing, which shows the distance between the center points of two units. The spacing characteristics of the test samples (A) - (F) were respectively up to the anti-crack ring +2mm, anti-crack ring +3mm, anti-crack ring +4mm, anti-crack ring +5mm, anti-crack ring +6mm and a blank sample. The processing position of stripe unit is based on the center point, and the spacing characteristic quantity is distributed to both ends in turn. According to Equation 5.1, it can be calculated that the surface area ratio of each unit in the double combination model with different spacing characteristic quantities is 46.8%, 35.6%, 29.9%, 26.1%, 22.4%, and the area ratio P_u of blank sample unit is 0%.

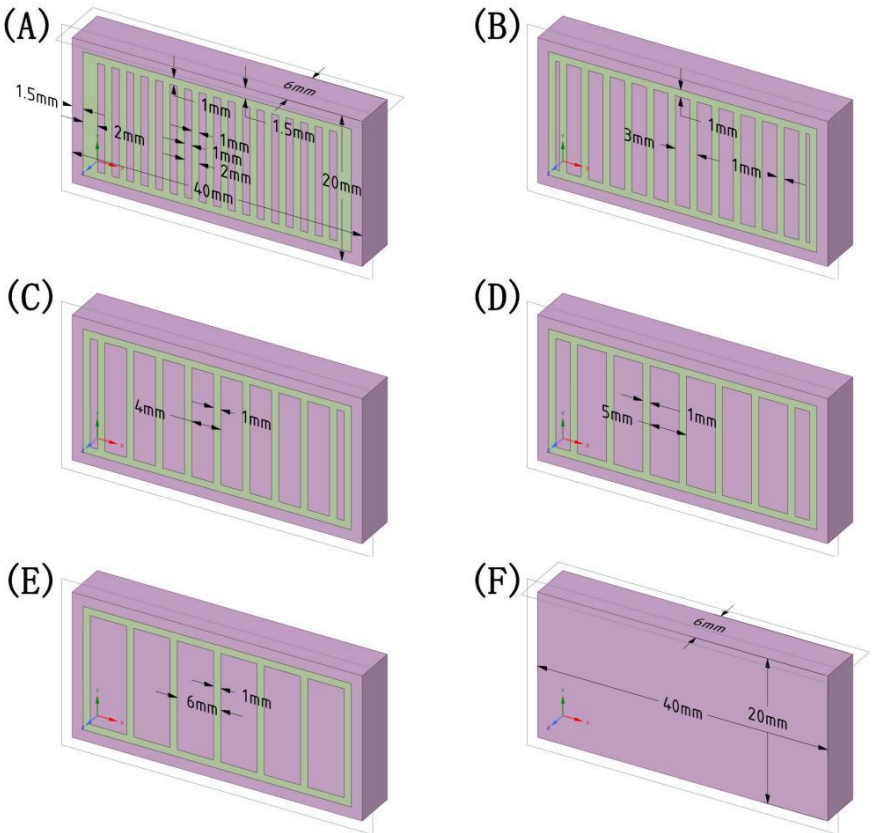


Fig.5.14 Schematic diagram of samples with different spacing characteristics and blank samples

Firstly, the thermal fatigue test was carried out on the double combination model samples with different spacing characteristics. After every 200 thermal cycles, the samples were taken out, cleaned, and observed for surface cracks, and the number of thermal fatigue cracks and the length of main cracks were recorded. The test results are shown in Fig.5.15. It can be seen from the figure that the number of cracks and the main crack length of the bionic sample are far less than those of the blank sample. Bionic samples under thermal fatigue test of the early crack number close to gap bigger after 400 times thermal cycling, also for the main crack length, bionic sample at 200 times thermal cycling is 2 mm, above is anti-crack ring play its thermal fatigue crack resistance, crack initiation at the sample boundaries, on the one hand, the unit itself is not easy to crack, On the other hand, the anti-crack ring model perpendicular to the growth direction of the crack can well hinder the growth of the thermal fatigue crack. When the crack touches the anti-crack ring, it needs to save more energy if it wants to pass through the unit, or the crack first passivates and then deflects, which changes the direction of the growth. After 400 times thermal cycling thermal fatigue crack breakthrough anti-crack ring, different spacing characteristic model selection is a vertical stripe unit and the friction angle, so the shorter edges of thermal fatigue crack growth for sample have hindered the advantage, in contrast to the growth of the long side hot fatigue crack, hinder the disadvantage, between the two unit can be extended unhindered, Therefore, the number of cracks and the main crack length began to increase after 400 thermal cycles. At the end of the experiment, the number

of thermal fatigue cracks and the main crack length of the 2mm spacing characteristic sample are the minimum. The number of thermal fatigue cracks decreases by 48%, 46%, 37%, 35%, 32%, and the thermal fatigue crack growth rate decreases by 50%, 47%, 37%, 32%, 26%, respectively.

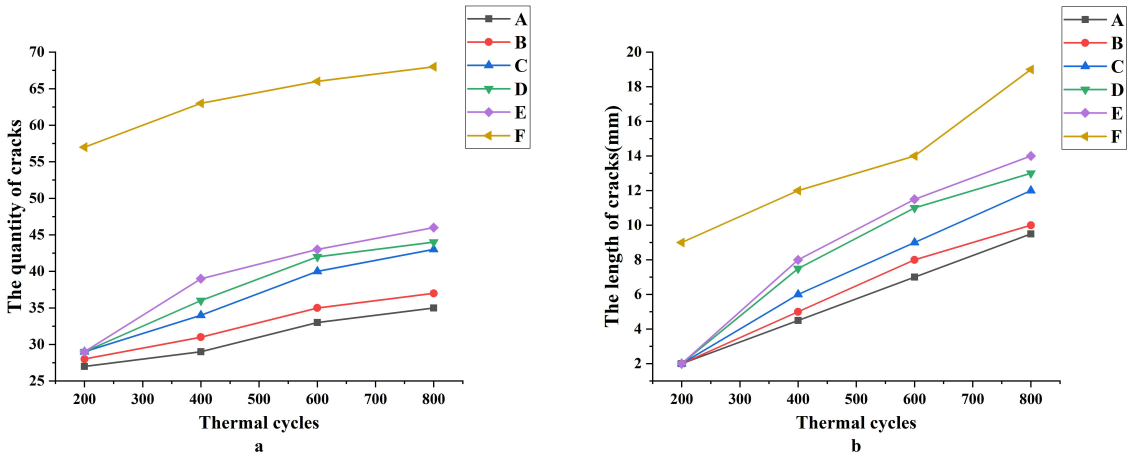


Fig.5.15 Thermal fatigue test results of samples with different spacing characteristics :(a), the quantity of thermal fatigue cracks; (b), length of thermal fatigue main crack

The wear results after thermal fatigue of the double combination model with different spacing characteristic quantities are shown in Fig.5.16. The wear loss weight of the blank sample is higher than that of the bionic sample, but the difference between the wear loss weight and that of the bionic sample is smaller than that of the single model. A~E are the samples with spacing characteristic quantities of 2mm~6mm in turn, and the wear loss weight decreases first and then increases in each stage. Among them, the weight loss of 4mm spacing characteristic sample is the least. The main reason is that the stripe units with different spacing characteristic quantities are vertically distributed with the friction direction at an angle of 90°, and the friction coefficient is

relatively large [226, 227]. The unit of 2mm spacing sample occupies the largest surface area ratio, but its wear resistance is similar to that of 6mm spacing sample. The reason can be analyzed by combining Ansys finite element simulation results.

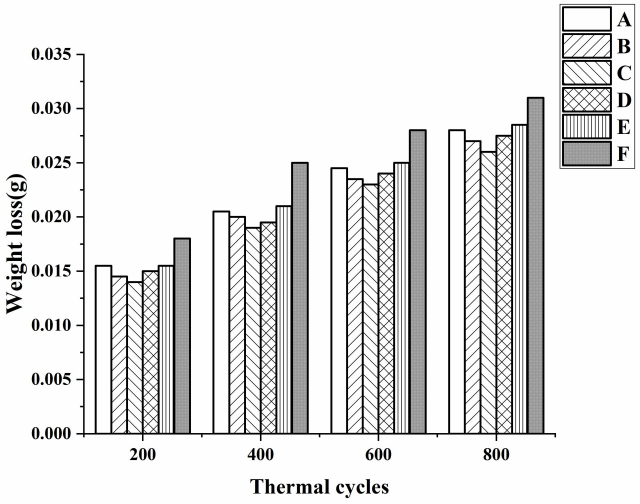


Fig.5.16 Wear weight loss of samples with different spacing characteristics

Fig.5.17 shows the equivalent stress distribution of the wear path of the double combination model with different spacing characteristic quantities. The surface stress value of the sample units with 2mm spacing ranges from 0.053 to 0.063MPa, and the surface stress value of the sample units with 3mm spacing ranges from 0.056 to 0.068MPa. 4mm spacing sample units surface stress value range in 0.059~0.072MPa, 5mm spacing sample units surface stress value range in 0.056~0.067MPa, 6mm spacing sample units surface stress value range in 0.057~0.068MPa, blank sample wear path stress was a parabolic distribution, the stress is concentrated at the edge of the sample. On the wear path, the difference between the unit and the base is 4mm > 3mm > 6mm > 5mm > 2mm in descending order. Fig.5.18 shows the surface

equivalent stress distribution results of the double combination model with different spacing characteristic quantities. In the figure, the more the color is red, the greater the surface stress value is, and the bluer the smaller the surface stress value is. It can be seen that the stress value on the surface of the bionic sample is mainly on the surface of the unit, and the stress value on the surface of the unit of the sample with 4mm spacing is the largest. The surface stress value of the sample with 2mm spacing is the smallest, and the stress of the blank sample is concentrated at the edge around the surface. It can be seen that although the hard unit on the surface of the 2mm spacing sample occupies the largest proportion, the stress borne by the unit is small, and the stress difference between the unit and the base material is the smallest. On the other hand, the 6mm sample has the smallest proportion of unit, and the number of thermal fatigue cracks and the main crack length are the largest among all the bionic samples, so it is most affected by cracks during wear. The extreme value of equivalent stress in the wear path of the 4mm spacing sample is the largest, and the surface equivalent stress is also the largest among all the samples, indicating that the base metal of the base bears the least stress, and the hard unit can effectively protect the base.

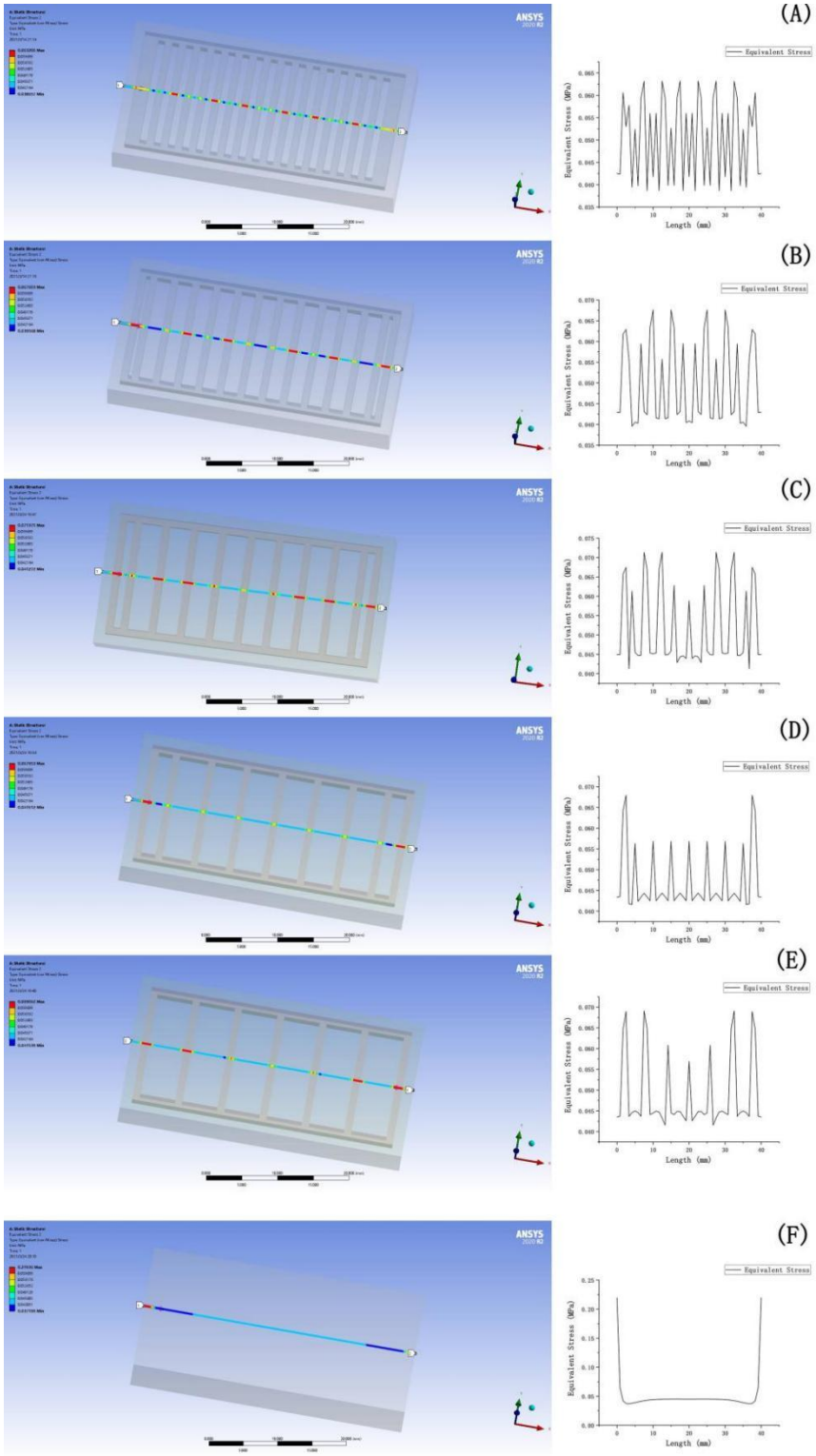


Fig.5.17 Equivalent stress distribution of wear path of samples with different spacing characteristics

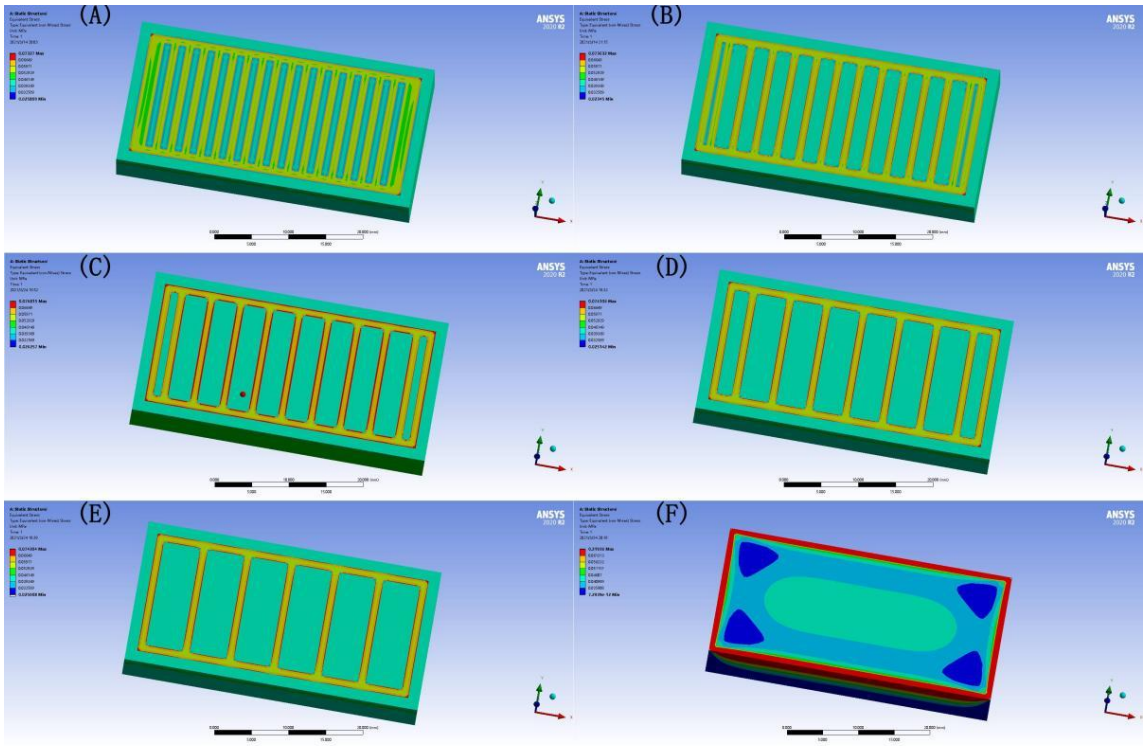


Fig.5.18 Surface equivalent stress distribution of samples with different spacing characteristics

5.3.2 The influence and analysis of characteristic quantities with different distribution angles

In order to give full play to the good performance of the truck drum brake, the bionic coupling model of the truck drum brake was designed. On the basis of the previous research, it is found that the model perpendicular to the crack growth direction has the best thermal fatigue resistance, which is suitable for the thermal fatigue zone of drum brake to prevent the macroscopic crack generation. Since the cracks at the sample boundary grow in the vertical boundary direction, which is similar to the thermal fatigue zone of drum brake, an anti-crack ring model is designed and combined with a single model from different angles to prepare a double combination coupling bionic model. As shown in Fig.5.19, six samples (A) - (F) successively end the double

combination model of anti-crack ring +0° angle, anti-crack ring +30° angle, anti-crack ring + 45° angle, anti-crack ring + 60° angle, and anti-crack ring + 90° angle. In order to maintain the same surface area ratio of sample surface units, adjacent stripe unit were processed on the long side of sample A and the short side of sample E.

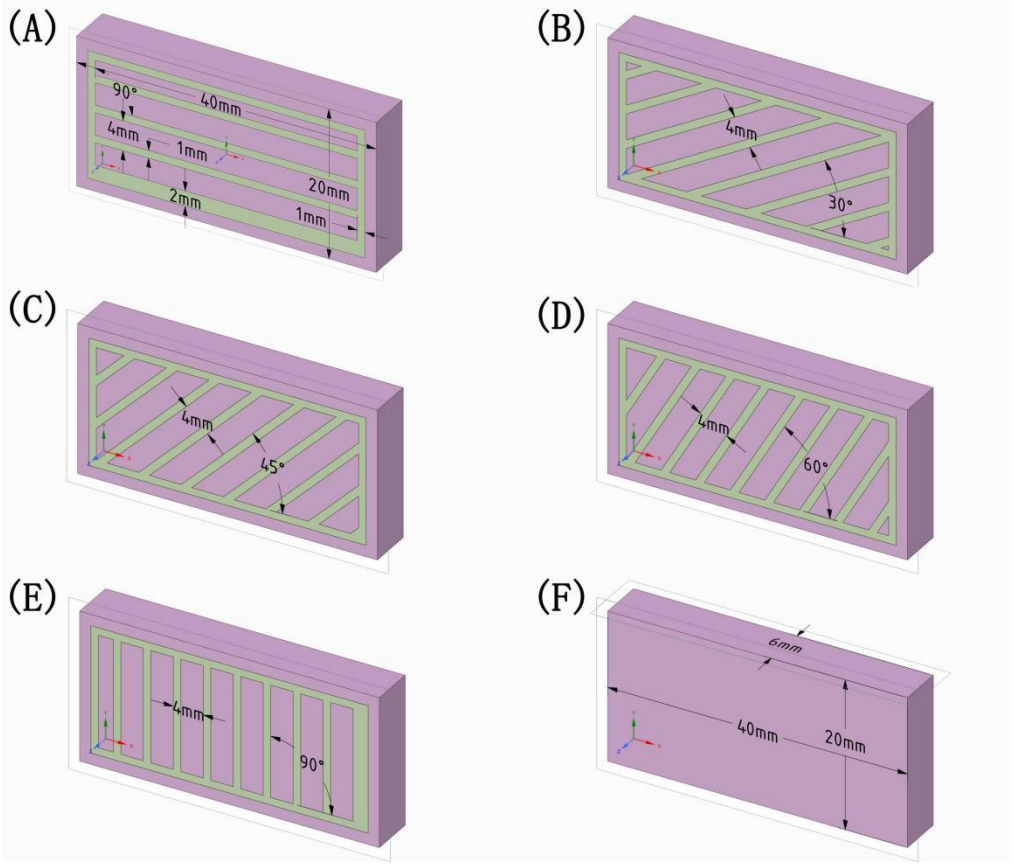


Fig.5.19 Schematic diagram of characteristic samples and blank samples from different angles

According to the calculation results of the number of thermal fatigue cracks in Fig.5.20a, the crack growth rate of all samples is similar, and the number of thermal fatigue cracks decreases by 36%, 38%, 41%, 40%, and 37% in turn. Fig.5.20b main crack length results. At 200 cycles, the main crack of all samples was limited to 2mm. With the progress of thermal fatigue test, the main crack breaks through the anti-crack

ring. Although samples A and E have two connected long and short sides of the unit, they are still not enough to make up for the disadvantage of the short and long sides. At the end of the test, the main crack length of sample E is the longest and that of sample C is the shortest. For all samples, although the number of cracks and the length of the main crack increase with the increase of the number of thermal fatigue cycles, there are differences among samples. This is mainly due to the different thermal fatigue resistance of different angle models. Similar to the above, sample C has advantages on both the long side and the short side compared with other samples. Therefore, the thermal fatigue resistance of sample C is the best, while the thermal fatigue resistance of sample A and sample E is poor, but they fully demonstrate the performance of anti-crack ring. It also proves that the unit perpendicular to the crack growth direction is the most effective way to hinder the crack. The thermal fatigue crack growth rate decreases by 39%, 50%, 55%, 42% and 37%, respectively. Fig.5.21 shows the weight loss result of the double combination model. It can be seen from the figure that the weight loss of sample A is the least when 200 thermal cycles are carried out in the thermal fatigue experiment. This is because the thermal fatigue cracks are few and short, which have little influence on wear, while the 0° angle model is parallel to the friction direction, and the friction coefficient is the smallest. The maximum weight loss of sample E is because the 90° angle model is perpendicular to the friction direction, and the resistance is the largest. Subsequently, with the progress of the thermal fatigue experiment, the thermal fatigue cracks increase and expand continuously, and the influence of thermal fatigue cracks on wear increases in the later

stage of the experiment. Therefore, the weight loss of sample C is minimized at the end of the experiment.

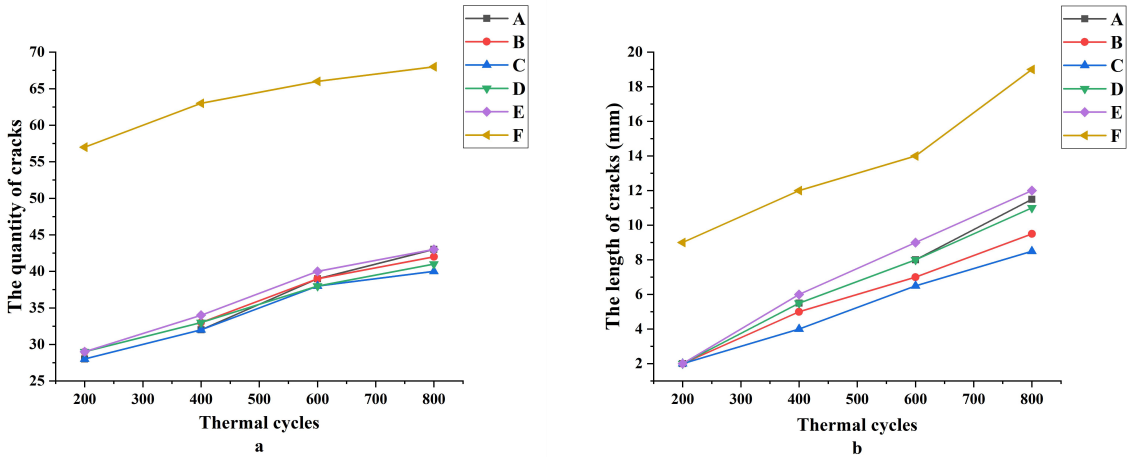


Fig.5.20 Thermal fatigue test results of samples with different angle characteristic:(a), the quantity of thermal fatigue cracks; (b), length of thermal fatigue main crack

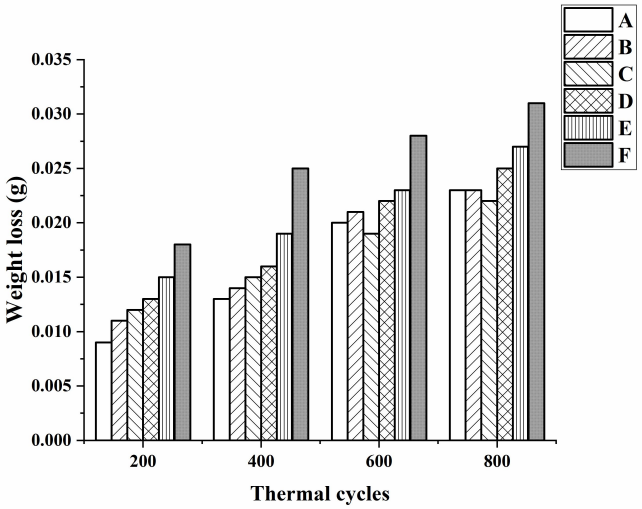


Fig.5.21 Wear weight loss of samples with different spacing characteristics

Fig.5.22 shows the Ansys finite element simulation results of the surface equivalent stress of the double combination model with different angle characteristic quantities. In the figure, the set values of stress in legends with different colors are consistent.

The redder the color is, the larger the stress value is, and the bluer the smaller the stress value is. The stress value of the bionic sample is mainly distributed on the surface of the unit, and it can be seen that the stress value of the 45° angle characteristic quantity model is the largest. The stress distribution of blank sample is mainly concentrated at the edges around the surface. The simulated equivalent stress distribution results are consistent with the thermal fatigue and wear test results above.

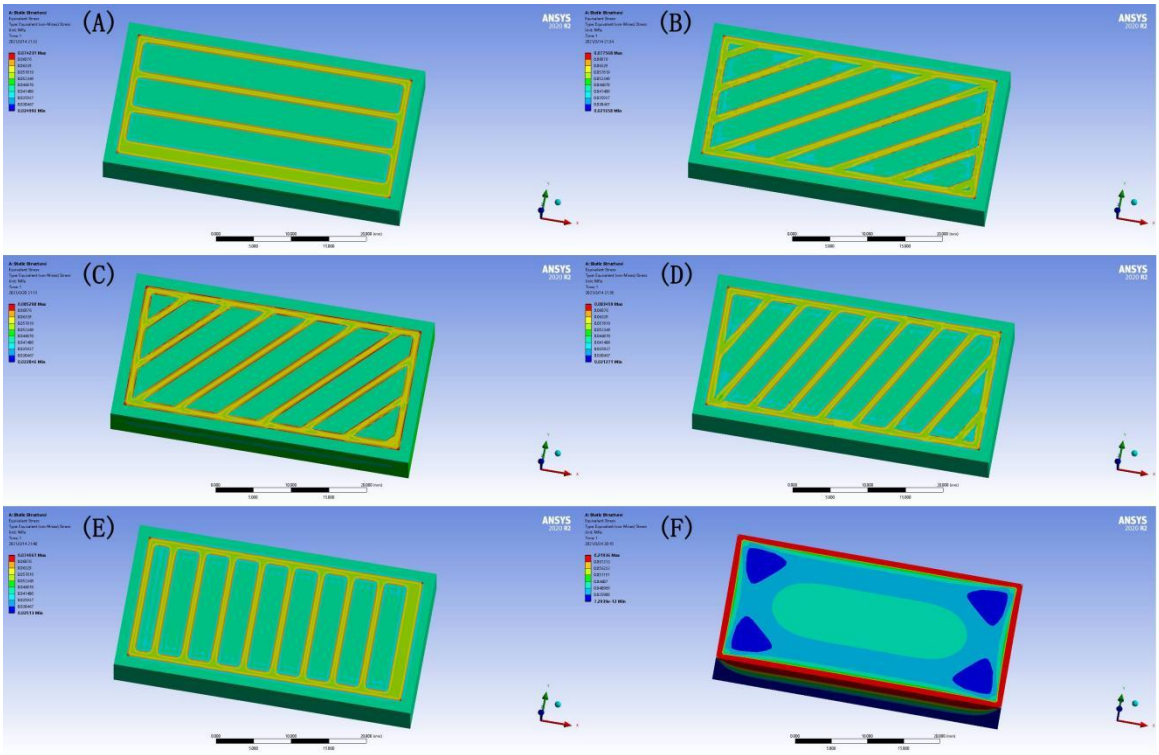


Fig.5.22 Surface equivalent stress distribution of samples with characteristic from different angles

In this chapter, by studying the thermal fatigue and wear resistance of stripe units with different characteristic quantities, the coupling bionic model suitable for different areas of grey cast iron drum brake is obtained, and the double combination coupling bionic model on the working surface of drum brake is designed and fabricated. In

previous studies, it was found that the mesh model had an obvious arrest effect on thermal fatigue crack [228]. Therefore, the 4mm spacing characteristic and 45° angle characteristic were retained, and the double combination model of anti-crack ring +45° angle mesh was designed the equivalent stress of the model was analyzed by Ansys finite element analysis software. Fig.5.23 is the schematic diagram of the double combination model of the anti-crack ring +45° angle mesh. The distance between the center points of each two units is 4mm, and the distance between the center points of the anti-crack ring and the edge of the sample is 2mm. The equivalent stress distribution result of the model is shown in Fig.5.24, which shows that the equivalent stress on the surface of the sample is mainly distributed on the surface of the coupling bionic model. A path was drawn in the wear direction of the sample, and the distribution of stress values on this path was calculated. It can be seen that the stress values were mainly concentrated on the anti-crack rings on both sides, and the stress values of the unit ranged from 0.053 MPa to 0.066MPa. Hence presumably anti-crack ring in the early stage of the thermal cycle and wear can bear the stress of the sample surface, with the increase of thermal cycles, thermal fatigue crack breakthrough after anti-crack ring, mesh encircled the crack will rely on its own characteristics in the mesh, increase the difficulty of the breakthrough of crack, increase the length of the crack propagation path, improve thermal fatigue and wear resistance of the sample.

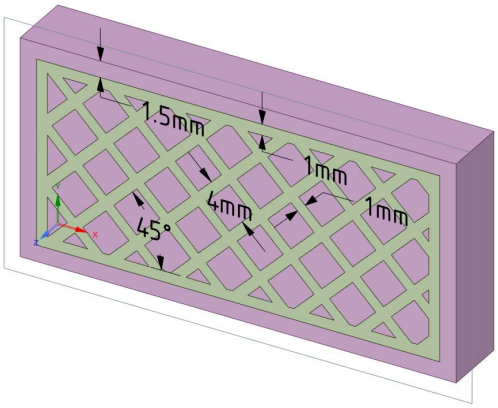


Fig.5.23 Schematic diagram of anti-crack ring + 45° angle mesh model

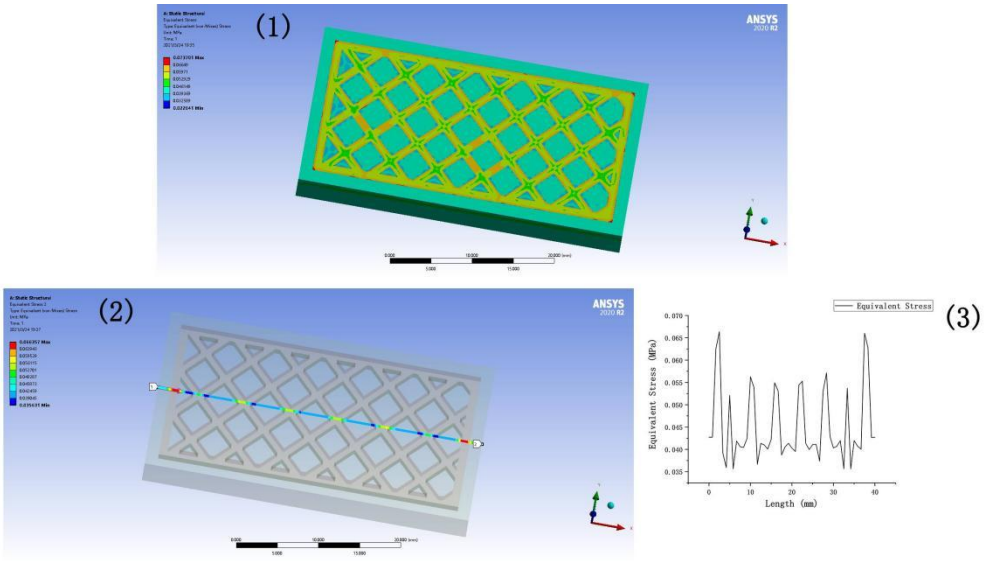


Fig.5.24 Equivalent stress distribution of anti-crack ring + 45° angle mesh model

5.4 Chapter Summary

In view of the failure characteristics of grey cast iron drum brake with non-uniform regional damage, in order to maximize the advantages of coupling bionic idea, this chapter aims to design the coupling bionic model suitable for machining on the working surface of drum brake. The following work is done, and the following conclusions are drawn:

(1) Design different spacing between the stripes of the characteristic model, show 90 ° vertical stripe friction angle and direction, compared with a blank sample, combined with the finite element analysis, thermal fatigue and wear resistance of bionic sample than the blank sample, among them 2 mm spacing is one of the best characteristics of thermal fatigue crack resistance, bear the stress value is less, but because the unit the weight loss of the sample is the most in the wear test. The surface area ratio of the samples with 6mm spacing is the least, and the number of cracks in the late thermal cycle has a great influence on the wear. The 4mm spacing characteristic sample has the best wear resistance. The stress of a blank sample is concentrated on the edge of the sample surface, and the stress of a full unit sample is also concentrated on the edge of the surface.

(2) Spacing design different angles stripe model, the characteristics of each sample unit of surface area ratio than the basic same, two stripe center spacing of 4 mm, compared with blank sample, combined with the finite element analysis, thermal fatigue and wear resistance of bionic sample than the blank sample, where 0 ° angle model has the best performance of thermal fatigue crack resistance from the vertical direction, with the increase of thermal cycles, The 45° angle characteristic quantity sample has the best thermal fatigue resistance, and the 45° angle characteristic quantity unit surface bears the most equivalent stress, and has the best wear resistance.

(3) The anti-crack ring and different spacing characteristic quantity stripe model were designed. The spacing between the center point of the s anti-crack ring and the

edge of the sample was 2mm, and the characteristic quantity fringe with different spacing was 90° perpendicular to the friction direction. The anti-crack ring +2mm spacing sample with the largest surface area ratio of the unit has the best thermal fatigue crack resistance. However, due to the minimum stress borne by the unit and the minimum stress difference between the unit and the base metal, its wear performance is only better than that of the blank sample. The unit of the anti-crack ring +4mm bore the most stress. Although the length of the surface thermal fatigue crack and the main crack was not the best, it could rely on the hard unit to prevent the wear of the abrasive particles and protect the base during the wear process, so it had the best wear resistance.

(4) The surface area ratio of each sample element is basically the same. Anti-crack ring can hinder the initiation and propagation of thermal fatigue crack in the early stage of thermal cycle. The samples with +45° angle have the best thermal fatigue and wear resistance. Compared with the blank samples, the total number of thermal fatigue cracks and the thermal fatigue crack propagation rate of the bionic samples with different morphologic coupling elements decreased by 28%-48% and 13%-55%, respectively.

Chapter 6 Study on Bench Test

6.1 Introduction

All the above test results show that appropriate laser processing parameters can be used to prepare high-quality structural coupling element units on the corresponding base metal surface. The coupling bionic model can be processed into a coupling bionic model according to a certain morphological coupling element spacing and angle characteristics, which can greatly improve the thermal fatigue and wear resistance of base metal. In order to verify the conclusions obtained in the laboratory, this chapter selects several grey cast iron drum brakes produced in the same batch for bench test, and further studies the thermal fatigue and wear resistance performance of drum brakes with coupling bionic model surface, as well as the influence on their service life under the actual state of engineering.

6.2 Trial Manufacture of Bionic Drum Brake

The drum brake used in the test is the grade 200 grey cast iron drum brake produced by Guangdong Fuwa Company, which is consistent with the base material used in Chapter 3 and Chapter 5 of this research. The failure mode of the drum brake is that the thermal fatigue crack starts from the frictional area and extends through the top, and the growth direction of the thermal fatigue crack is 90° perpendicular to the frictional direction. Therefore, the purpose of this study is to inhibit the initiation and expansion of the thermal fatigue crack and extend the service life of the drum brake.

Based on the conclusion of all the above studies, the double combination model of anti-crack ring +45° angle stripe and anti-crack ring +45° angle mesh is fabricated on the working face of drum brake with anti-crack ring have the best performance of resistance to thermal fatigue crack, but due to friction in the same direction, the anti-crack ring does not have the best wear resistance, therefore is suitable for processing in the region of the frictionless drum brake at the top of the thermal fatigue impact area, thermal fatigue crack will be much extended to the area after thermal cycles, the anti-crack ring can play a good blocking performance, delay crack propagation to the top of the drum brake failure time, so as to extend the service life of the drum brake. According to the principle of the same surface area ratio of the unit, the top of the following square stripe model is selected as the starting position when preparing anti-crack rings on the drum brake working surface. An anti-crack ring is prepared every 7mm, and a total of three anti-crack rings are arranged in parallel in the thermal fatigue affected area of the working surface. 45 ° angle stripes and mesh model were processed in the region of the friction, the friction area or drum brake and the friction pair contact area, the thermal fatigue crack initiation in this area, as the thermal cycle of crack extension along the vertical scaling up, through the study above, 45 ° angle characteristic has the best thermal fatigue and wear resistance, The model can be constructed in the friction area to maximize its performance. The spacing characteristic quantity was calculated according to the surface area ratio of the unit, and the spacing between the center points of the two stripes was 50mm. The laser parameters for the preparation of the coupling bionic model are the processing

parameters obtained after optimization above, and an untreated blank drum brake is used as a comparison reference for the bench test. The working surface of the drum brake is shown in Fig.6.1.



Fig.6.1 Drum brake working face: (1), untreated drum brake; (2), anti-crack ring +45° angle stripe; (3), anti-crack ring +45° angle mesh

6.3 Drum Brake Bench Test Results and Analysis

Bench tests can simulate drum brakes working under extreme conditions to test their braking performance and service life. According to the test, the drum brake to be tested will start to check the crack condition of the working face after 200 times of braking, and the drum brake will be removed from the test bench every 10 cycles for observation. Due to too much data, representative result pictures are selected in this chapter for illustration, and the same area is selected for lateral comparison. Fig.6.2 shows the working face of the three drum brakes at 200 cycles. It can be seen that long thermal fatigue cracks have appeared in the friction area of the untreated drum brake, and the lower part of the working face and the thermal fatigue influence area are full of small cracks. Meanwhile, the number and length of thermal fatigue cracks

of the bionic drum brake are far less than that of the blank drum brake. In particular, the cracks of the bionic drum brake basically grow in the base region in the middle of the two stripe units. When the cracks expand to the top, they meet the obstacles of the unit, so that there are few cracks under the unit in the picture. When the number of tests reached 250, dense thermal fatigue cracks extending from the friction area to the top of the drum brake could be seen on the surface of the untreated drum brake. However, most of the longer cracks of the bionic drum brake were confined to the base part in the middle of the unit, and the bionic model successfully hindered the expansion of thermal fatigue cracks. When the bench test was carried out for 300 cycles, the surface of the blank drum brake had a large number of penetrating cracks growing from the friction area to the top of the drum brake, and the number of cracks of the drum brake with anti-crack ring +45° stripe increased faster and its length increased at the same time, but at this time the unit could still play an excellent performance of blocking cracks. The crack growth of the +45° mesh model is still not obvious. After 360 cycles of the test, a large number of thermal fatigue cracks are connected to the untreated drum brake. At this time, cracks running through the top of the drum brake have appeared, and the drum brake fails, as shown in Fig.6.7. The crack on the working face of the drum brake in the stripe model began to break through the 45° angle unit, and the anti-crack ring began to play an obstruction role. In the mesh model, the thermal fatigue crack was still confined to the enclosed area of the unit. After 420 bench tests, as shown in Fig.6.6, the crack on the surface of the drum brake in the stripe model has broken through the anti-crack ring, while the

growth trend of the crack in the mesh model is similar to that in the stripe model after 300 tests.

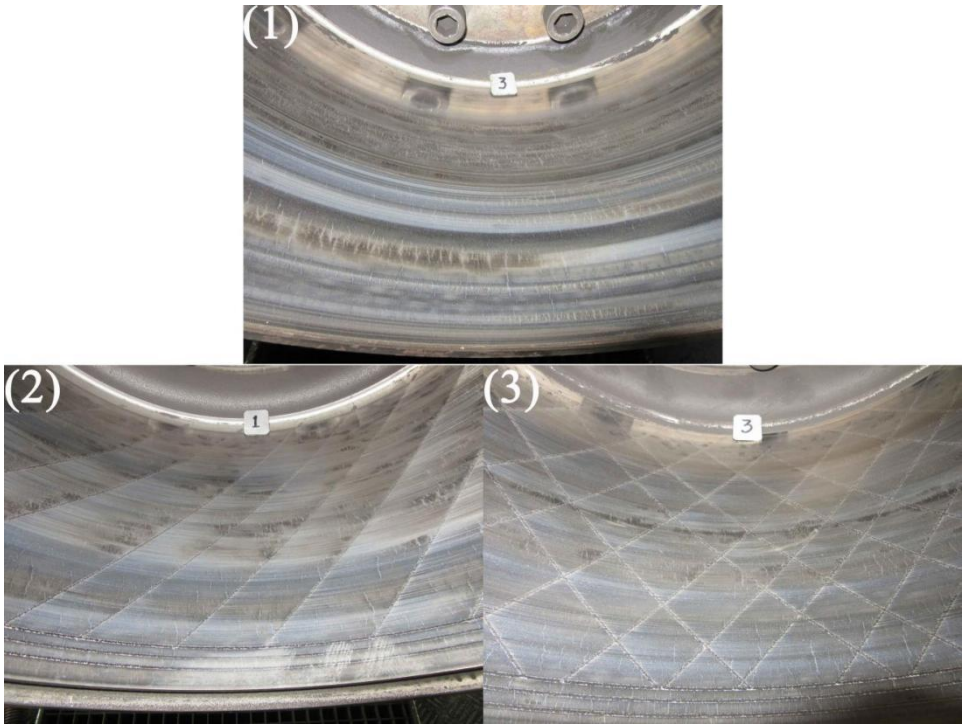


Fig.6.2 Drum brake after 200 cycles of bench test

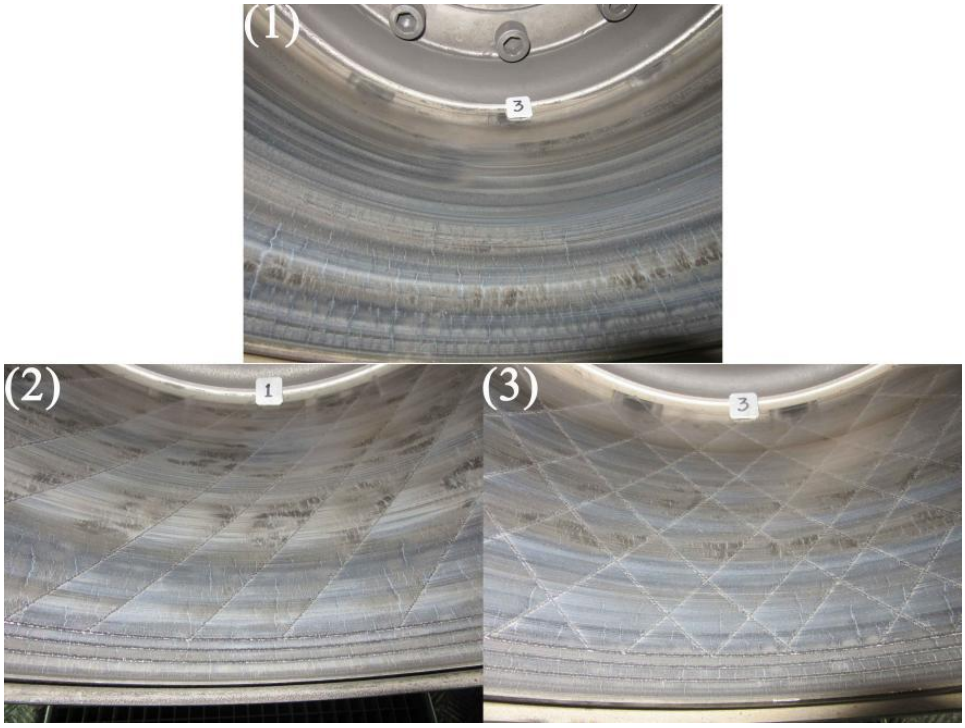


Fig.6.3 Drum brake after 250 cycles of bench test

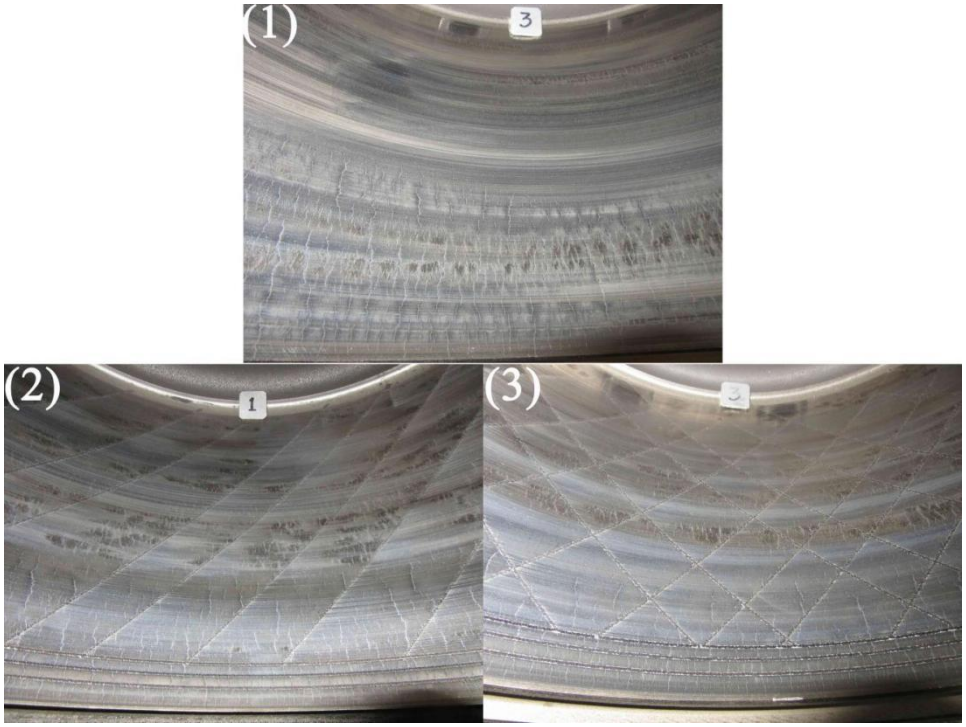


Fig.6.4 Drum brake after 300 cycles of bench test

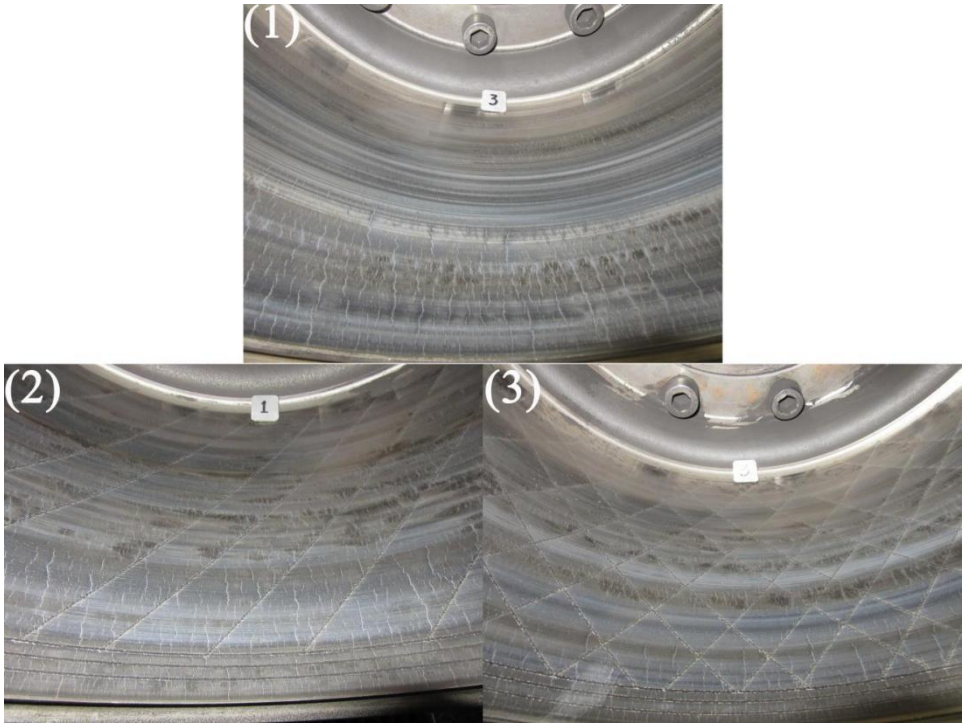


Fig.6.5 Drum brake after 360 cycles of bench test

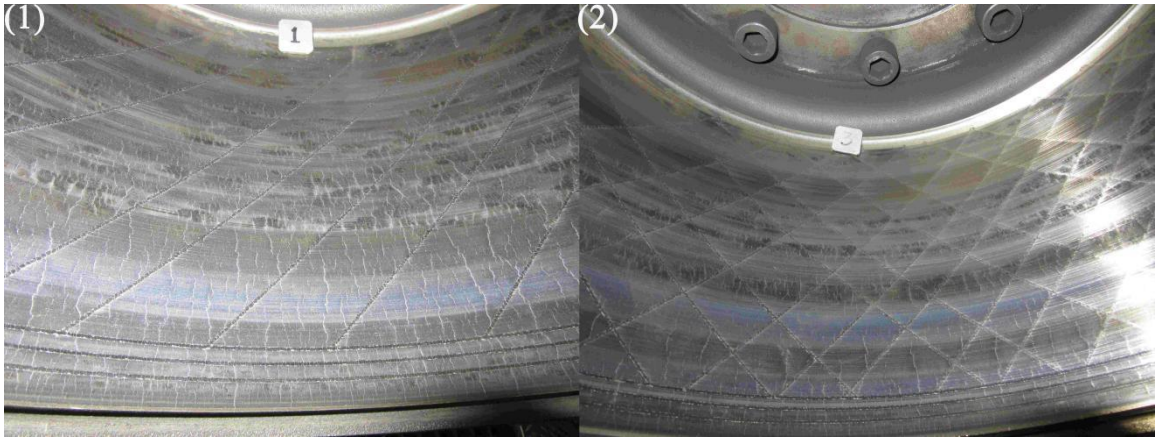


Fig.6.6 Drum brake after 420 cycles of bench test

The drum brake of the double combination model with the most terminal anti-crack ring +45° stripe model failed after 480 tests, and the drum brake of the double combination model with the anti-crack ring +45° mesh model failed after 530 tests. The main crack morphology resulting in failure is shown in Fig.6.7. Permeants and

imaging agents are successively sprayed on the surface of the main crack to observe the crack morphology clearly. The service life of the most anti-crack ring +45° stripe model is increased by 33%, and the service life of the anti-crack ring +45° mesh model is increased by 47%. Because the bench test simulates the performance of the drum brake under extreme working conditions, it can be inferred that the bionic drum brake can improve the service life in the actual operation of trucks and other conventional use, so as to reduce the service cost and increase the transportation efficiency.

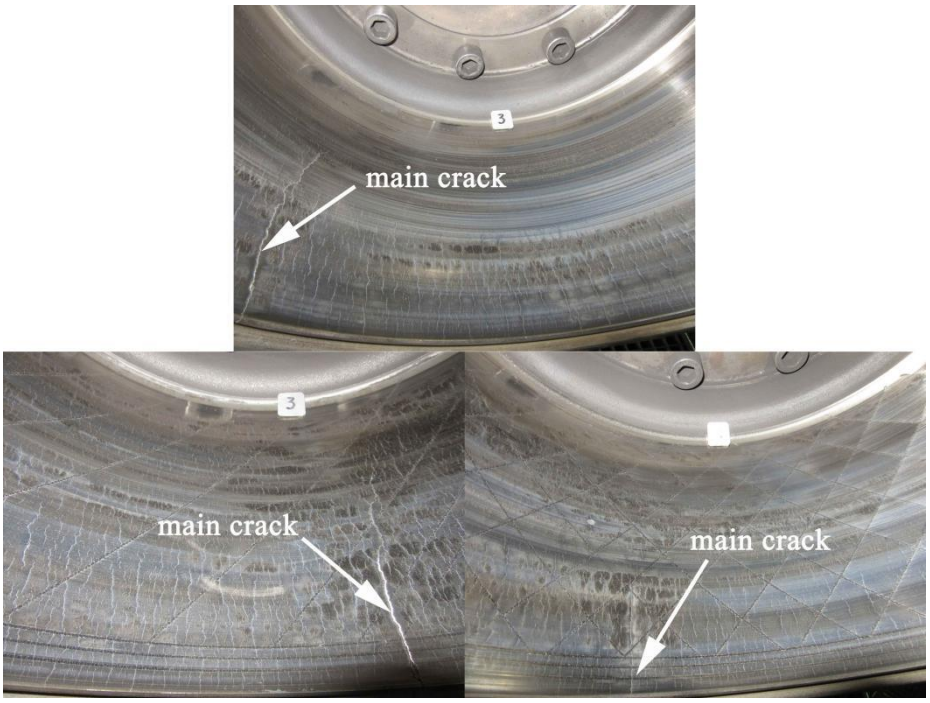


Fig.6.7 Failure picture of drum brake

6.4 Trial-manufacture and test of multi-combination coupling bionic drum brake

The success of the bench test of the bionic drum brake with a double combination

model proves that the advantages of coupling bionic idea can be given full play to the characteristics of regional damage of drum brake, and machining different models in different areas of drum brake working surface can improve its service life with very low cost and provide a new idea at the same time. Blank according to the picture of the drum brake fails, you can see that thermal fatigue damage is not serious, located at the base of the mining area are tiny hot fatigue crack, considering the machining efficiency, friction drum brake area the following part does not need to existing bionic coupling model, so the design much more combination of the characteristics of bionic coupling model, That is, anti-crack ring +45° angle 50mm spacing characteristic quantity mesh +45° angle 100mm spacing mesh model, as shown in Fig.6.8. The thermal fatigue influence area on the top of drum brake is still three parallel anti-crack rings, and the friction area is a 45° angle 50mm spacing characteristic quantity, which is consistent with the double combination model mentioned above. The area under the drum brake is a 45° angle 100mm spacing mesh model, which is designed to ensure the connectivity of the model. According to the bench test conditions above, the bionic drum brake with double combination coupling is tested.



Fig.6.8 Multi-combination coupling bionic drum brake

Fig.6.9 bench test results of multi-combination coupling bionic drum brake. The image is still selected for comparative study of crack morphology of drum brake working face in the same area under different test times. As can be seen from the figure, the bionic model has an obvious blocking effect on thermal fatigue cracks. Cracks increase with the increase of test times, but most cracks are blocked by the unit before 450 cycles and cannot be connected until the drum brake fails at 510 cycles. Multi-combination coupling bionic drum brake life increased by 42%. The proposed multi-combination model provides a reference and a new idea for the design of coupling bionic in the future.

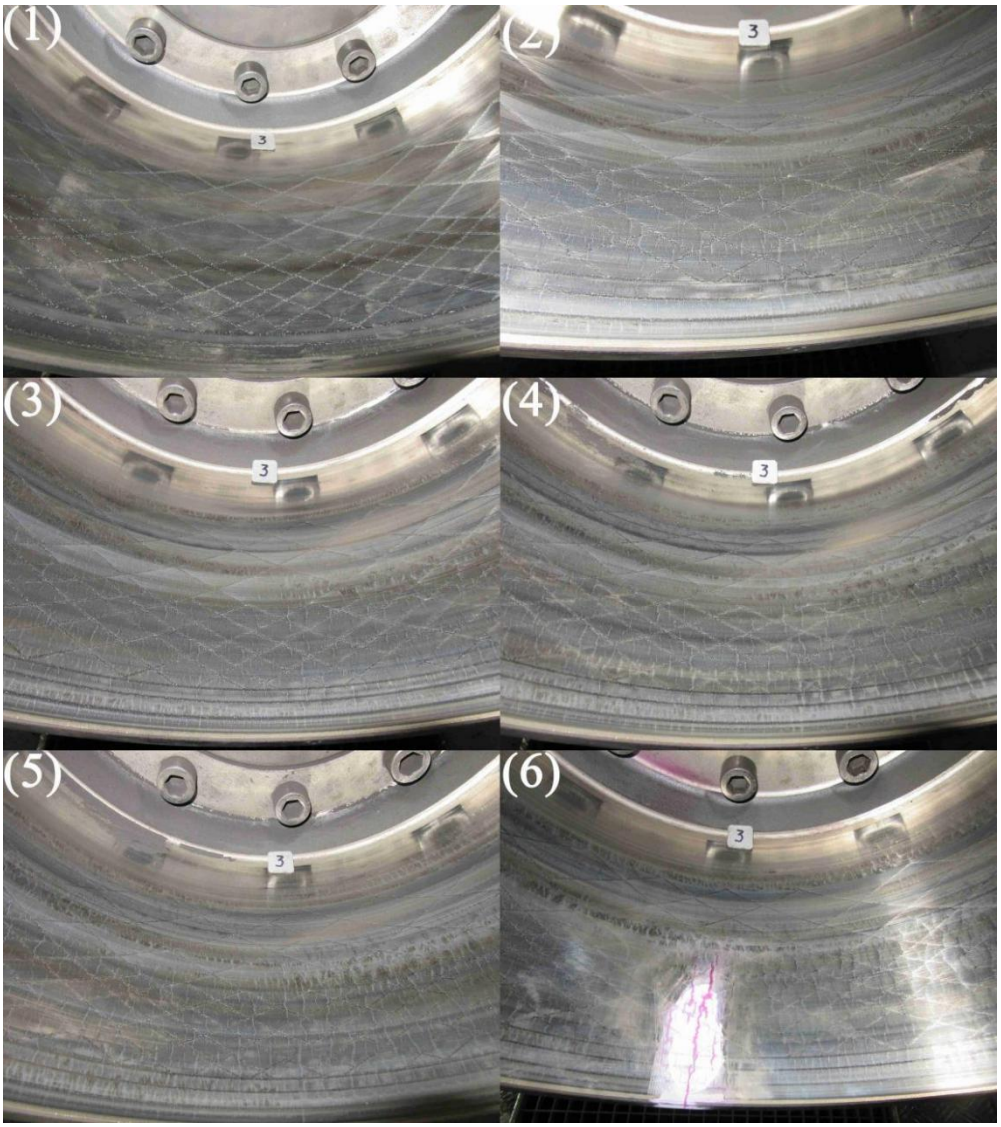


Fig.6.9 Results of multi-combination coupling bionic drum brake: (1), 200 cycles; (2), 250 cycles; (3), 300 cycles; (4), 360 cycles; (5), 450 cycles; (6), 510 cycles

In addition, according to the average friction coefficient output of the bench test bench, as shown in Fig.6.10, it can be seen that all bionic drum brakes can improve the service life of the drum brake without affecting the braking performance or even strengthening it.

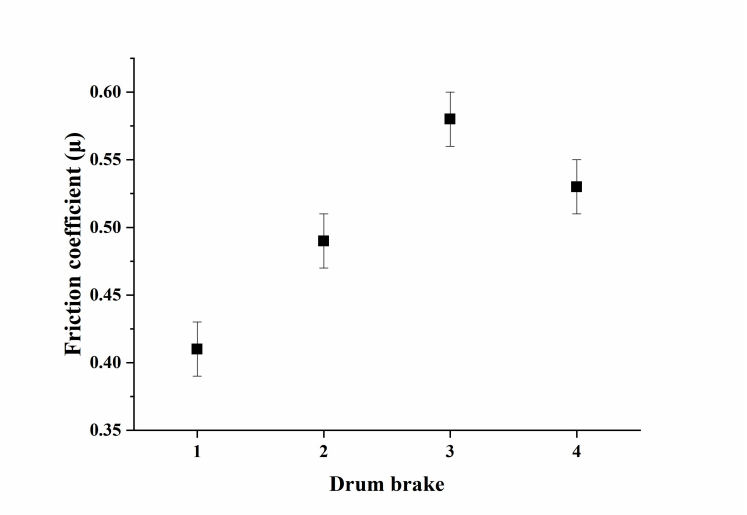


Fig.6.10 Friction coefficient:1, untreated drum brake; 2, anti-crack ring +45° angle stripe; 3, anti-crack ring +45° angle mesh;4, multi-combination coupling bionic drum brake

6.5 Chapter summary

From the selection of laser processing parameters in the laboratory in this study, on the base of the influence of laser coupling bionic processing and coupling model of bionic design based on the research, manufacture with more different bionic coupling model on the surface of grey cast iron drum brakes, and compared with untreated blank drum brake, the bench test. The following conclusions are drawn:

(1) The life of the untreated blank drum brake in bench test is 360 times, the life of the anti-crack ring +45°stripe model is 480 times, the life of the anti-crack ring +45° mesh model is 530 times, and the life of the bionic drum brake is improved by 33% and 47% respectively. The application of laser coupling bionic treatment technology to the surface of the grey cast iron drum brake can enhance its thermal fatigue and wear resistance and improve its service life.

(2) According to the idea of coupling bionic, organisms in nature will constantly evolve and change according to the living environment to adapt to the environment, and the design of coupling bionic model also presents diversity according to the needs of target objects. The proposed multi-combination coupling bionic model provides a new idea for the design of coupling bionic model in the future.

(3) Bionic drum brakes can improve the service life of drum brake through bench tests, which is to give the drum brake more extreme conditions of use, bionic drum brake in the daily use of trucks also extended the service time, greatly improve the transportation efficiency and save costs.

(4) Laser coupling bionic processing technology is a low-cost, high-performance improvement of drum brake, very cost-effective means. Under the premise of only needing the laser, electricity bill and labor as the cost, the daily transportation service time of truck drum brake can be increased by at least 50%. The application prospect of laser coupling bionic processing technology is broad, and the development of coupling bionic drum brake is important for promoting drum brake manufacturing industry.

Chapter 7 Conclusion

7.1 Summary and Conclusions

In this study, the grey cast iron truck drum brake was taken as the research object, and the biological adaptive fatigue and wear resistance surface in nature was used as the prototype by laser melting method. Structural coupling elements with different characteristic values were prepared on the grey cast iron surface used for truck drum brake. Through the laser parameters optimization and selection of drum brake laser processing parameters, grey cast iron material coupling relationship between base metal and laser bionic coupling surface in the research, in view of the drum brake failure forms, to design of the double combination bionic coupling model, aimed at the preparation has the bionic coupling at the surface of the drum brake, under the effect of coupling elements to improve its thermal fatigue and wear resistance, Improve service life. The conclusion is as follows:

(1) The same laser parameters were used to process the samples with different thicknesses, and it was found that the thicker the samples were, the worse the quality of the coupling elements of the structure was. The finite element simulation analysis showed that with the increase of wall thickness, the longitudinal length of the cross section of the laser melted area became smaller, and the thicker the samples were, the smaller the thermal impedance was. Through the orthogonal design, the high-quality unit with the least number of pores and cracks and the ratio of depth to width of 0.722 was obtained. The laser processing

parameters were 140A, 8ms pulse width, 4Hz frequency, 1.2mm/s scanning speed and 9.8mm defocus. The relationship between sample wall thickness and laser power density is fitted. The laser power density of grey cast iron truck drum brake is 150.8W/mm^2. The microhardness of the high-quality unit is much higher than that of the base. The microhardness of the melted zone is 133% higher than that of the base, and the microhardness of the transformed zone is 90% higher than that of the base.

(2) Using the same laser parameters to process different graphite types of grey cast iron, the microhardness increases by 151%, 188%, 145%, 199%, 47% from A-E type. Within the scope of this study, type A graphite has the best thermal fatigue resistance, type C and type D graphite has the largest number of thermal fatigue cracks, type D graphite has the longest main crack length, and the unit improves the thermal fatigue resistance of type D graphite the most. The wear resistance of type C graphite is the best, while that of type D graphite is the worst. The unit can improve the wear resistance of type D graphite the most.

(3) The higher the carbon content, the weaker the oxidation resistance and the worse the thermal fatigue resistance of grey iron with the different carbon content of type A graphite. Within the scope of this study, the higher the carbon content, the higher the microhardness of the unit, the slower the growth rate of the number of thermal fatigue cracks, and the thermal fatigue resistance gradually decreases at the later stage of thermal cycling. The higher the carbon content, the better the wear resistance and the higher the hardness of the unit.

(4) The greater the pearlite content, the better the thermal fatigue resistance and wear resistance, and the smaller the interlamellar spacing, the better the thermal fatigue resistance and wear resistance. With the thermal fatigue experiment, the pearlite will gradually decompose, and the pearlite function will gradually disappear in the later stage of the experiment. The thermal fatigue resistance and wear resistance of the bionic samples is better than those of the untreated samples. For untreated samples and bionic samples, the best thermal fatigue resistance and wear resistance are obtained when the pearlite content is 98% and the pearlite interlamellar spacing is 152nm. After laser treatment, the influence of pearlite is reduced, and the difference of experimental results of each sample is reduced.

(5) Design different spacing between the stripes of the characteristic model, compared with blank sample, combined with the finite element analysis, thermal fatigue and wear resistance of bionic sample is better than blank sample, of which 2 mm spacing is one of the best characteristics of thermal fatigue crack resistance, bear the stress value is less, but because the unit, which results in the wear test sample lose weight the most. The surface area ratio of the samples with 6mm spacing is the least, and the number of cracks in the late thermal cycle has a great influence on the wear. The 4mm spacing characteristic sample has the best wear resistance. The stress of blank sample is concentrated at the edge of the sample surface, and the stress of full unit sample is also concentrated at the edge of the surface.

(6) Stripe model, the characteristics of different perspectives on the design of each sample unit surface area ratio than the basic same, compared with blank sample,

combined with the finite element analysis, thermal fatigue and wear resistance of bionic sample than the blank sample, where 0 ° angle model has the best performance of thermal fatigue crack resistance from the vertical direction, with the increase of thermal cycles, The 45° angle characteristic quantity sample has the best thermal fatigue resistance, and the 45° angle characteristic quantity element unit surface bears the most equivalent stress, and has the best wear resistance.

(7) A stripe model with different spacing between the center point of the ring and the edge of the sample was designed 2mm, with different spacing characteristic quantity stripe and friction direction are 90° vertical. The anti-crack ring +2mm spacing sample with the largest surface area ratio of the unit has the best thermal fatigue crack resistance. However, due to the minimum stress borne by the unit and the minimum stress difference between the unit and the base metal, its wear performance is only better than that of the blank sample. The unit of the anti-crack ring with a spacing of +4mm bears the most stress value. Although the thermal fatigue resistance is not optimal, it can rely on the hard unit to prevent the abrasive wear and protect the base during the wear process, so it has the optimal wear resistance. Then, the anti-crack ring and different angle characteristic quantity stripe model were designed, and the surface area ratio of each sample unit was basically the same. The anti-crack ring can hinder the initiation and propagation of thermal fatigue crack in the early stage of thermal cycle. The anti-crack ring samples with a +45° angle have the best thermal fatigue and wear resistance.

Compared with the blank samples, the total number of thermal fatigue cracks and the thermal fatigue crack propagation rate of the bionic samples with different morphologic coupling elements decreased by 28%-48% and 13%-55%, respectively.

(8) More than a test with different coupling surface bionic models of grey cast iron drum brake, and compared with untreated drum brake, bench test, the results showed that the untreated drum brake life expectancy of 360 times in the bench test and anti-crack ring + 45 ° angle stripe model for 480 times, the life of anti-crack ring + 45 ° angle of the life of the mesh model for 530 times, The life improvement of bionic drum brake is 33% and 47% respectively. The proposed multi-combination coupling bionic model can present diversity according to the needs of the target object, which provides a new idea for the design of the coupling bionic model in the future.

7.2 Suggestions for future work

In practical application, the improvement research of grey cast iron drum brakes remains in the optimization of the casting process of grey cast iron drum brakes. There are few related studies on the application of laser coupling bionic processing technology to grey cast iron drum brakes. Therefore, this study not only has technical value, but practical engineering application value.

In the following work, the simulation of the temperature and stress field of the bionic drum brake should continue to be studied. Meanwhile, applications of laser coupling

bionic technology in other materials, such as copper, should continue to be investigated.

Reference

[1] J. Berechman, Oecd, Oecd, Transport and economic development - Summary, 119th Round Table on Transport and Economic DevelopmentParis, France, 2001, pp. 103.

[2] T. Zhu, S.Z. Zhu, Establishment of Performance Evaluation Model of Highway Environmental Protection Based on Deep Learning, Wireless Communications & Mobile Computing, 2022 (2022).

[3] L. Palkovics, M. ElGindy, Examination of different control strategies of heavy vehicle performance, Journal of Dynamic Systems Measurement and Control-Transactions of the Asme, 118 (1996) 489-498.

[4] P.S. Shanker, A review on properties of conventional and metal matrix composite materials in manufacturing of disc brake, Materials Today-Proceedings, 5 (2018) 5864-5869.

[5] H. Hong, M. Kim, H. Lee, N. Jeong, H. Moon, E. Lee, H. Kim, M. Suh, J. Chung, J. Lee, The thermo-mechanical behavior of brake discs for high-speed railway vehicles, Journal of Mechanical Science and Technology, 33 (2019) 1711-1721.

[6] N.M. Ali, M.H. Peeie, M.A.H. Rasid, H. Ogino, Study on Differential Regenerative Braking Torque Control to Increase the Stability of the Small Electric Vehicle with Four In-Wheel Motors, 2nd International Conference on Automotive Innovation and Green Vehicle (AiGEV)Malaysia Automot Inst, Cyberjaya, MALAYSIA, 2016.

[7] G. Parker, J. Griffin, A. Popov, The effect on power consumption & handling of

efficiency-driven active torque distribution in a four wheeled vehicle, 24th Symposium of the International-Association-for-Vehicle-System-Dynamics (IAVSD)Graz, AUSTRIA, 2015, pp. 97-106.

[8] Y.W. Wu, Z.Q. Chen, R. Liu, F. Li, Lane Departure Avoidance Control for Electric Vehicle Using Torque Allocation, Mathematical Problems in Engineering, 2018 (2018).

[9] E. Borawska, A. Borawski, INFLUENCE OF THE INITIAL SPEED OF THE AGRICULTURAL TRACTOR ON THE BRAKES HEATING PROCESS DURING EMERGENCY BRAKING, Heat Transfer Research, 51 (2020) 967-974.

[10] S.C. Wu, S.Q. Zhang, Z.W. Xu, Thermal crack growth-based fatigue life prediction due to braking for a high-speed railway brake disc, International Journal of Fatigue, 87 (2016) 359-369.

[11] H. Zhou, X. Tong, Z. Zhang, X. Li, L. Ren, The thermal fatigue resistance of cast iron with biomimetic non-smooth surface processed by laser with different parameters, Materials Science and Engineering a-Structural Materials Properties Microstructure and Processing, 428 (2006) 141-147.

[12] Y.C. Zhou, T. Hashida, Thermal fatigue failure induced by delamination in thermal barrier coating, International Journal of Fatigue, 24 (2002) 407-417.

[13] A. Borawski, Conventional and unconventional materials used in the production of brake pads - review, Science and Engineering of Composite Materials, 27 (2020) 374-396.

[14] S. Huang, J.S. Bao, Y. Yin, S.R. Ge, T.G. Liu, A Review of Brake Friction

Materials: Development, Tribological Performance and Failure Prediction, Science of Advanced Materials, 11 (2019) 613-628.

[15] E. Jeong, C. Oh, Evaluating the effectiveness of active vehicle safety systems, Accident Analysis and Prevention, 100 (2017) 85-96.

[16] R.L. Rabin, Pathways to Auto Safety Assessing the Role of the National Highway Traffic Safety Administration, Conference on Administrative Law from the Inside Out - Themes in the Work of Jerry MashawYale Law Sch, New Haven, CT, 2015, pp. 297-321.

[17] M. Yan, J. Xu, Prediction Model for Brake-Drum Temperature of Large Trucks on Consecutive Mountain Downgrade Routes Based on Energy Conservation Law, Mathematical Problems in Engineering, 2018 (2018).

[18] C. Bai, H. Zhang, Research on the Sales Volume of Heavy Trucks in Various Usage Scenarios Based on the Analysis of the Static Market Big Data Model, 2nd International Conference on Forthcoming Networks and Sustainability in the IoT Era (FoNeS-IoT)Electr Network, 2022, pp. 107-115.

[19] L. Ren, Y. Liang, Biological couplings: Function, characteristics and implementation mode, Science China-Technological Sciences, 53 (2010) 379-387.

[20] X. Tong, H. Zhou, W. Zhang, Z.H. Zhang, L.Q. Ren, Thermal fatigue behavior of gray cast iron with striated biomimetic non-smooth surface, Journal of Materials Processing Technology, 206 (2008) 473-480.

[21] D.H. Yu, T. Zhou, H. Zhou, Y. Xu, P. Zhang, Y.Y. Yan, Effects of angle formation between melted zone and friction direction on thermal fatigue and wear resistance of

truck drum brake, Proceedings of the Institution of Mechanical Engineers Part D-Journal of Automobile Engineering, 235 (2021) 1297-1307.

[22] R. Lora, A. Dioszegi, L. Elmquist, Solidification Study of Gray Cast Iron in a Resistance Furnace, 9th International Symposium on Science and Processing of Cast IronLuxor, EGYPT, 2010, pp. 108-113.

[23] G.L. Rivera, R.E. Boeri, J.A. Sikora, Solidification of gray cast iron, Scripta Materialia, 50 (2004) 331-335.

[24] C.P. Tabrett, I.R. Sare, M.R. Ghomashchi, Microstructure-property relationships in high chromium white iron alloys, International Materials Reviews, 41 (1996) 59-82.

[25] D.M. Stefanescu, THERMAL ANALYSIS-THEORY AND APPLICATIONS IN METALCASTING, International Journal of Metalcasting, 9 (2015) 7-22.

[26] S. Recknagel, S. Noack, T. Steiger, H. Kipphardt, R. Matschat, International comparability of determination of mass fractions of chromium, copper, iron, manganese and zinc in aluminium alloy: Comit, Consultatif pour la Quantit, de MatiSre key comparison K42, Accreditation and Quality Assurance, 15 (2010) 401-407.

[27] M. Selin, D. Holmgren, I.L. Svensson, Influence of alloying additions on microstructure and thermal properties in compact graphite irons, International Journal of Cast Metals Research, 22 (2009) 283-285.

[28] L.J. Wu, W.G. Zhou, H. Cheng, Y.L. Su, X.J. Li, The study of structure optimization of blast furnace cast steel cooling stave based on heat transfer analysis,

Applied Mathematical Modelling, 31 (2007) 1249-1262.

[29] L.J. Wu, W.G. Zhou, H. Cheng, Y.L. Su, X.J. Li, C.Y. Song, The study of cooling channel optimization in blast furnace cast steel stave based on heat transfer analysis, International Journal of Advanced Manufacturing Technology, 29 (2006) 64-69.

[30] X.F. Ding, H. Huang, X.Z. Li, W. Matthias, S.Y. Huang, Q. Feng, Microstructures and Properties of High Performance Cast Irons Applied in Automobile Flywheels, Chinese Materials Conference (CMC)Yinchuan City, PEOPLES R CHINA, 2017, pp. 905-916.

[31] Q.G. Li, Y.N. Zhang, Y.N. Zhang, H.B. Liu, H.N. Ren, Y.M. Zhong, X.F. Huang, W.G. Huang, Influence of Sn and Nb additions on the microstructure and wear characteristics of a gray cast iron, Applied Physics a-Materials Science & Processing, 126 (2020).

[32] H. Lu, M. Liu, D. Yu, T. Zhou, H. Zhou, P. Zhang, H. Bo, W. Su, Z. Zhang, H. Bao, Effects of Different Graphite Types on the Thermal Fatigue Behavior of Bionic Laser-Processed Gray Cast Iron, Metallurgical and Materials Transactions a-Physical Metallurgy and Materials Science, 49A (2018) 5848-5857.

[33] Y.X. Zhou, J. Zhang, Z.G. Xing, H.D. Wang, Z.L. Lv, Microstructure and properties of NiCrBSi coating by plasma cladding on gray cast iron, Surface & Coatings Technology, 361 (2019) 270-279.

[34] S.C. Lin, T.S. Lui, L.H. Chen, J.M. Song, Effect of pearlite on the vibration-fracture behavior of spheroidal graphite cast irons under resonant conditions, Metallurgical and Materials Transactions a-Physical Metallurgy and Materials Science,

33 (2002) 2623-2634.

[35] S. Niwa, I. Yamada, A. Hagisaka, S. Shiota, Y. Gao, Y. Gotoh, Proposal of Inspection Method for Shrinkage Cavities in Spheroidal Graphite Cast Iron by Electromagnetic Force Vibration Using Differential Vibration Measurement, Ieee Transactions on Magnetics, 58 (2022).

[36] A.I. Karlina, A.E. Balanovsky, V.V. Kondratiev, A.D. Kolosov, N.N. Ivanchik, RESULTS OF MODIFICATION OF CAST IRON BY CARBON NANOSTRUCTURES OF GAS CLEANING DUST OF SILICON PRODUCTION, International Conference on Aviamechanical Engineering and Transport (AVENT)Irkutsk Natl Res Tech Univ, Irkutsk, RUSSIA, 2018, pp. 169-173.

[37] C. Khuntrakool, S. Janudom, P. Muangjunburee, T. Chotikarn, N. Mahathaninwong, T. Chucheep, A. Yodjan, Effects of Chemical Composition on Microstructure and Properties of High Phosphorus Grey Cast Iron Brake Shoe, International Journal of Metalcasting, 16 (2022) 1221-1234.

[38] L.Q. Jian, L.P. Ning, S.R. Yang, J.M. Wang, M.Q. Hua, Triboelectrification Electrostatic Potential of Graphite/Monomer Casting Nylon Composites Under Dry Sliding: Correlation With Electrical Resistivity and Wear Mechanisms, Polymer Composites, 31 (2010) 1369-1377.

[39] C.P. Samal, J.S. Parihar, D. Chaira, The effect of milling and sintering techniques on mechanical properties of Cu-graphite metal matrix composite prepared by powder metallurgy route, Journal of Alloys and Compounds, 569 (2013) 95-101.

[40] Q. Sui, P. Zhang, H. Zhou, Y. Liu, L.Q. Ren, Influence of Cycle Temperature on

the Wear Resistance of Vermicular Iron Derivatized with Bionic Surfaces, Metallurgical and Materials Transactions a-Physical Metallurgy and Materials Science, 47A (2016) 5534-5547.

[41] C. Blawert, N. Hort, K.U. Kainer, Automotive applications of magnesium and its alloys, Transactions of the Indian Institute of Metals, 57 (2004) 397-408.

[42] M.K. Kulekci, Magnesium and its alloys applications in automotive industry, International Journal of Advanced Manufacturing Technology, 39 (2008) 851-865.

[43] A. Troiani, M. Rosi, S. Garzoli, C. Salvitti, G. de Petris, Iron-Promoted C-C Bond Formation in the Gas Phase, Angewandte Chemie-International Edition, 54 (2015) 14359-14362.

[44] Y.P. Wu, Q. Shi, B.N. Sun, Y.H. Wang, Experimental Investigation on Drop in Tensile Performance Index of Carbon Fiber Composite in Use, International Conference on Manufacturing Science and Engineering (ICMSE 2009)Zhuhai, PEOPLES R CHINA, 2009, pp. 1645-+.

[45] H. Yang, Q. Wang, T. Zhou, H. Zhou, The Relationship between the Model of the Laser Biomimetic Strengthening of Gray Cast Iron and Matching between Different Brake Pads, Metals, 10 (2020).

[46] D. Yu, T. Zhou, H. Zhou, H. Bo, H. Lu, Non-single bionic coupling model for thermal fatigue and wear resistance of gray cast iron drum brake, Optics and Laser Technology, 111 (2019) 781-788.

[47] D.H. Yu, T. Zhou, H. Zhou, P. Zhang, Y.Y. Yan, Effects of Pearlite on Thermal Fatigue and Wear Resistance of Gray Cast Iron Treated by Laser, Journal of Materials

Engineering and Performance, 31 (2022) 3962-3974.

[48] Y. Zhao, L.Q. Ren, X. Tong, H. Zhou, L. Chen, Frictional Wear and Thermal Fatigue Behaviours of Biomimetic Coupling Materials for Brake Drums, Journal of Bionic Engineering, 5 (2008) 20-27.

[49] M. Tirovic, Energy thrift and improved performance achieved through novel railway brake discs, Applied Energy, 86 (2009) 317-324.

[50] H.J.P.o.t.R.S.o.L. Tomlinson, The influence of stress and strain on the physical properties of matter. Part I. Moduli of elasticity—continued. Relations between moduli of elasticity, thermal capacity, and other physical constants, 38 (1885) 488-500.

[51] D.L. Duquesnay, H. Abdelraouf, T.H. Topper, A. Plumtree, A MODIFIED FRACTURE-MECHANICS APPROACH TO METAL FATIGUE, Fatigue & Fracture of Engineering Materials & Structures, 15 (1992) 979-993.

[52] T. Makino, M. Yamamoto, K. Hirakawa, Fracture mechanics approach to the fretting fatigue strength of axle assemblies, Symposium on Fretting Fatigue - Current Technology and PracticesUniv Utah, Salt Lake City, Ut, 1998, pp. 509-522.

[53] G. Zambelis, T.D. Botelho, O. Klinkova, I. Tawfiq, C. Lanouette, A new approach in testing fatigue fracture mechanics properties in asymmetrical bonded composite/metal assemblies, Composites Part B-Engineering, 158 (2019) 390-399.

[54] S. Suresh, Fatigue of materials, Cambridge university press1998.

[55] V. Firouzdor, M. Rajabi, E. Nejati, F. Khomamizadeh, Effect of microstructural constituents on the thermal fatigue life of A319 aluminum alloy, Materials Science

and Engineering a-Structural Materials Properties Microstructure and Processing, 454 (2007) 528-535.

[56] Z.W. Li, X.T. Feng, Y.J. Zhang, Y.H. Gong, G.Q. Zhu, Effect of Mechanical Damage on the Thermal Conductivity of Granite, Rock Mechanics and Rock Engineering, 53 (2020) 1039-1051.

[57] C. Zweben, Advances in LED packaging and thermal management materials, 12th Conference on Light-Emitting Diodes - Research, Manufacturing, and Applications XISan Jose, CA, 2008.

[58] M. Frichtl, Y. Anwar, A. Strifas, S. Ankem, Improving the Low-Temperature Toughness of a High-Strength, Low-Alloy Steel with a Lamellarization Heat Treatment, Metals and Materials International.

[59] Y.W. Shi, Z.X. Han, Effect of weld thermal cycle on microstructure and fracture toughness of simulated heat-affected zone for a 800 MPa grade high strength low alloy steel, Journal of Materials Processing Technology, 207 (2008) 30-39.

[60] Y. You, X.M. Wang, C.J. Shang, INFLUENCE OF AUSTENITIZING TEMPERATURE ON THE MICROSTRUCTURE AND IMPACT TOUGHNESS OF A HIGH STRENGTH LOW ALLOY HSLA100 STEEL, Acta Metallurgica Sinica, 48 (2012) 1290-1298.

[61] Y. Qiu, R.S. Xin, J.B. Luo, Q.X. Ma, Effect of deformation modes and heat treatment on microstructure and impact property restoration of internal crack healing in SA 508 steel, Materials Science and Engineering a-Structural Materials Properties Microstructure and Processing, 778 (2020).

[62] J.X. Zhang, J.F. Huang, H.B. Wang, L. Lu, H. Cui, J.S. Zhang, MICROSTRUCTURES AND MECHANICAL PROPERTIES OF SPRAY FORMED H13 TOOL STEEL, Acta Metallurgica Sinica, 50 (2014) 787-794.

[63] H.G. Fu, Z.Q. Jiang, J.D. Xing, Y.X. Li, The effects of RE-Mg on thermal fatigue resistance of cast high speed steel(HSS) rolls, in: Z.Y. Zhong, H. Saka, T.H. Kim, E.A. Holm, Y.F. Han, X.S. Xie (Eds.) Pricm 5: The Fifth Pacific Rim International Conference on Advanced Materials and Processing, Pts 1-52005, pp. 217-220.

[64] N.K. Fukumasu, P.L. Pelegrino, G. Cueva, R.M. Souza, A. Sinatora, Numerical analysis of the stresses developed during the sliding of a cylinder over compact graphite iron, Wear, 259 (2005) 1400-1407.

[65] Y.L. Yang, Z.Y. Cao, Z.S. Lian, H.X. Yu, Thermal Fatigue Behavior and Cracking Characteristics of High Si-Mo Nodular Cast Iron for Exhaust Manifolds, Journal of Iron and Steel Research International, 20 (2013) 52-57.

[66] D. Mellouli, N. Haddar, A. Koster, H.F. Ayedi, Thermal fatigue failure of brass die-casting dies, Engineering Failure Analysis, 20 (2012) 137-146.

[67] D. Tribula, A microstructural study of creep and thermal fatigue deformation in 60tin-40lead solder joints, University of California, Berkeley1990.

[68] E.J.P.o.t.P.S.S.B. Hall, The deformation and ageing of mild steel: III discussion of results, 64 (1951) 747.

[69] C.P. Petch, ELECTROCARDIOGRAPHIC CHANGES AFTER NEPHRECTOMY, Lancet, 264 (1953) 627-628.

[70] B.N. Du, L.Y. Sheng, C.Y. Cui, Z.Y. Hu, X.F. Sun, Effects of Grain Refinement

on the Low-Cycle Fatigue Behavior of IN792 Superalloys, Crystals, 11 (2021).

[71] H.Q. Lina, Y.G. Zhao, B. Zhao, L.G. Han, J. Ma, Q.C. Jiang, Formation and Thermal Fatigue Properties of Fine-grained Heat Affected Zone on Cast-hot-working-die Steel after Electropulsing Stimulation with High Current Density, Isij International, 48 (2008) 1647-1653.

[72] Y. Sun, Y. Wang, Y. Li, K.C. Zhou, L. Zhang, Tribological behaviors of Ag-graphite composites reinforced with spherical graphite, Transactions of Nonferrous Metals Society of China, 30 (2020) 2177-2187.

[73] W.B. Zhou, F. Hao, D.N. Fang, THE EFFECTS OF ELASTIC STIFFENING ON THE EVOLUTION OF THE STRESS FIELD WITHIN A SPHERICAL ELECTRODE PARTICLE OF LITHIUM-ION BATTERIES, International Journal of Applied Mechanics, 5 (2013).

[74] E.A. Lopez-Covaleda, S. Ghodrat, L.A.I. Kestens, C.H. Sacre, T. Pardoen, Proposal of Characterization Procedure of Metal-Graphite Interface Strength in Compacted Graphite Iron, Materials, 11 (2018).

[75] Y. Wu, Y. Liu, H. Chen, Y. Chen, H.Y. Li, X.Y. Cao, Developing the ductility and thermal fatigue cracking property of laser-deposited Stellite 6 coatings by adding titanium and nickel, Materials & Design, 162 (2019) 271-284.

[76] Y.X. Zhang, R. Buntain, J. Edwards, B. Alexandrov, J.A. Penso, Asme, EVALUATION OF SUSCEPTIBILITY TO THERMAL FATIGUE CRACKING IN HIGH TEMPERATURE ALLOYS FOR REFINERY OLEFIN APPLICATIONS, ASME Pressure Vessels and Piping Conference (PVP)Electr Network, 2020.

[77] X. Tong, H. Zhou, L.Q. Ren, Z.H. Zhang, W. Zhang, R.D. Cui, Effects of graphite shape on thermal fatigue resistance of cast iron with biomimetic non-smooth surface, International Journal of Fatigue, 31 (2009) 668-677.

[78] X. Tong, H. Zhou, L. Chen, Z.H. Zhang, L.Q. Ren, Effects of C content on the thermal fatigue resistance of cast iron with biomimetic non-smooth surface, International Journal of Fatigue, 30 (2008) 1125-1133.

[79] M.C. Rukadikar, G.P. Reddy, THERMAL-EXPANSION BEHAVIOR OF ALLOYED PEARLITIC FLAKE GRAPHITE CAST IRONS, Journal of Engineering Materials and Technology-Transactions of the Asme, 108 (1986) 358-364.

[80] D.A. Cendon, A.R. Torabi, M. Elices, Fracture assessment of graphite V-notched and U-notched specimens by using the cohesive crack model, Fatigue & Fracture of Engineering Materials & Structures, 38 (2015) 563-573.

[81] Q.B. Wang, Z.X. Li, Y.W. Shi, Effect of Alloy Addition Method on Thermal Fatigue of Cr5-Deposited Metal, Journal of Materials Engineering and Performance, 23 (2014) 1329-1339.

[82] M.A. Gebril, M. Aldlemey, F.I. Haider, The effect of heat treatment of gray and nodular cast iron with ferrite matrix on mechanical properties and corrosion rate compared with medium carbon steel, Advanced Materials Research, Trans Tech Publ, 2014, pp. 1158-1162.

[83] M.R. Chavez, A. Amaro, C. Flores, A. Juarez, C. Gonzalez-Rivera, Newton Thermal Analysis of gray and nodular eutectic cast iron, in: H. BalmoriRamirez, M. Brito, J.G. CabanasMoreno, H.A. CalderonBenavides, K. Ishizaki, A.

SalinasRodriguez (Eds.) Advanced Structural Materials Ii2006, pp. 153-158.

[84] S.N. Pan, R. Chen, Fatigue crack and evolution prediction of compacted graphite iron under thermal loading with variable amplitude, Engineering Failure Analysis, 102 (2019) 284-292.

[85] B. Drapkin, A. Zhukov, Y.V.J.M.S. Piguzov, H. Treatment, The initial stage in thermal fatigue failure of cast iron, 15 (1973) 964-966.

[86] S. Wu, X.C. Li, J. Zhang, C.J. Shang, R.D.K. Misra, Microstructural Refinement and Mechanical Properties of High-Speed Niobium-Microalloyed Railway Wheel Steel, Steel Research International, 86 (2015) 775-784.

[87] A. Jakubus, M.S. Soinski, Contribution to the Assessment of Thermal Shock Resistance of Metals, Archives of Foundry Engineering, 20 (2020) 97-100.

[88] J.L. Fan, H.C. Cheng, M.Y. Lu, B.Y. Huang, J.M. Tian, Effect of alloyed elements Ti, Zr on the property and microstructure of Mo alloy, Rare Metal Materials and Engineering, 37 (2008) 1471-1474.

[89] J.S. Yu, Y.Q. Zhao, Q.Y. Zhao, W. Zhang, W.T. Huo, Y.S. Zhang, Microstructure and Properties of Titanium Matrix Composites Synergistically Reinforced by Graphene Oxide and Alloying Elements, Advanced Engineering Materials.

[90] M. Dojka, M. Kondracki, A. Studnicki, R. Dojka, Crystallization Process of High Chromium Cast Iron with the Addition of Ti and Sr, Archives of Foundry Engineering, 18 (2018) 57-64.

[91] K. Weber, D. Regener, Microstructure and magnetic properties of white cast irons for grinding balls, Materialwissenschaft Und Werkstofftechnik, 33 (2002) 599-605.

[92] Y.H. Liu, W.C. Qu, Y. Su, TiC Reinforcement Composite Coating Produced Using Graphite of the Cast Iron by Laser Cladding, Materials, 9 (2016).

[93] P.L. Zhang, H. Yan, C.W. Yao, Z.G. Li, Z.S. Yu, P.Q. Xu, Synthesis of Fe-Ni-B-Si-Nb amorphous and crystalline composite coatings by laser cladding and remelting, Surface & Coatings Technology, 206 (2011) 1229-1236.

[94] A. Srivastava, V. Joshi, R. Shivpuri, R. Bhattacharya, S. Dixit, A multilayer coating architecture to reduce heat checking of die surfaces, Surface & Coatings Technology, 163 (2003) 631-636.

[95] A. Srivastava, V. Joshi, R. Shivpuri, Computer modeling and prediction of thermal fatigue cracking in die-casting tooling, Wear, 256 (2004) 38-43.

[96] M. Pellizzari, A. Molinari, G. Straffelini, Thermal fatigue resistance of gas and plasma nitrided 41CrAlMo7 steel, Materials Science and Engineering a-Structural Materials Properties Microstructure and Processing, 352 (2003) 186-194.

[97] A. Persson, S. Hogmark, J. Bergstrom, Temperature profiles and conditions for thermal fatigue cracking in brass die casting dies, Journal of Materials Processing Technology, 152 (2004) 228-236.

[98] J. Xu, Z.Y. Li, W.H. Zhu, Z.L. Liu, W.J. Liu, The comparative study of thermal fatigue behavior of laser deep penetration spot cladding coating and brush plating Ni-W-Co coating, Applied Surface Science, 253 (2006) 2618-2624.

[99] A. Persson, S. Hogmark, J. Bergstrom, Simulation and evaluation of thermal fatigue cracking of hot work tool steels, International Journal of Fatigue, 26 (2004) 1095-1107.

[100] G. Balachandran, A. Vadiraj, M. Kamaraj, E. Kazuya, Mechanical and wear behavior of alloyed gray cast iron in the quenched and tempered and austempered conditions, Materials & Design, 32 (2011) 4042-4049.

[101] J.N. Aoh, J.C. Chen, On the wear characteristics of cobalt-based hardfacing layer after thermal fatigue and oxidation, Wear, 250 (2001) 611-620.

[102] C. Meng, H. Zhou, Y. Zhou, M. Gao, X. Tong, D. Cong, C. Wang, F. Chang, L. Ren, Influence of different temperatures on the thermal fatigue behavior and thermal stability of hot-work tool steel processed by a biomimetic couple laser technique, Optics and Laser Technology, 57 (2014) 57-65.

[103] D.L. Cong, H. Zhou, Z.A. Ren, L.Q. Ren, G.Y. Liu, B.S. Lu, C. Meng, C.W. Wang, Thermal fatigue resistance of H13 die steel repaired by partial laser surface remelting process, Materials Science and Technology, 30 (2014) 355-362.

[104] H. Sakamoto, K. Hirakawa, Fracture analysis and material improvement of brake discs, Jsme International Journal Series a-Solid Mechanics and Material Engineering, 48 (2005) 458-464.

[105] M. Kurzyp, C.A. Mills, R. Rhodes, T.R. Pozegic, C.T.G. Smith, M.J. Beliatis, L.J. Rozanski, A. Werbowy, S.R.P. Silva, Filtration properties of hierarchical carbon nanostructures deposited on carbon fibre fabrics, Journal of Physics D-Applied Physics, 48 (2015).

[106] V. Lutz, J. Duchet-Rumeau, N. Godin, F. Smail, F. Lortie, J.F. Gerard, Ex-PAN carbon fibers vs carbon nanotubes fibers: From conventional epoxy based composites to multiscale composites, European Polymer Journal, 106 (2018) 9-18.

[107] T. Mader, M. Trautmann, D. Nestler, B. Wielage, Continuous splitting of carbon fibre rovings, Journal of Industrial Textiles, 45 (2016) 930-943.

[108] L. Gea, T. Zafar, D. Wong, S.S. Parka, Manufacturing of Pitch Based Carbon Fibers through Microwave Treatments, Manufacturing Letters, 33 (2022) 95-102.

[109] T. Kajita, L.C. Pardini, F.C.L. de Melo, Chemical vapor densification process of carbon fiber substrates, in: L. Salgado, F.A. Filho (Eds.) Advanced Powder Technology Iv2005, pp. 413-418.

[110] X.F. Liu, P. Li, Z.X. Liu, Modification Process of Carbon Fiber Reinforcement for Aluminum Matrix Composite, Spring International Conference on Material Sciences and Technology (MST-S)Xian, PEOPLES R CHINA, 2012, pp. 899-905.

[111] V. Stanciu, T. Dobre, A. Stoica, F. Tache, A.C. Toma, T.G. Chiciudean, Carbon fiber aluminum matrix composite for advanced aerospace structures, 17th International Symposium of the Danube-Adria-Association-for-Automation-and-ManufacturingVienna, AUSTRIA, 2006, pp. 391-392.

[112] M.A. Bily, Y.W. Kwon, R.D. Pollak, Study of Composite Interface Fracture and Crack Growth Monitoring Using Carbon Nanotubes, Applied Composite Materials, 17 (2010) 347-362.

[113] K. Oguri, T. Toriyama, M. Yabe, A. Tonegawa, Y. Nishi, High resistance to fracture of carbon fiber irradiated by sheet electron beam irradiation, 45th International SAMPE Symposium and Exhibition on Bridging the Centuries with SAMPEs Materials and Processes TechnologyLong Beach, Ca, 2000, pp. 539-542.

[114] M. Safiuddin, G. Abdel-Sayed, N. Hearn, Flexural and Impact Behaviors of Mortar Composite Including Carbon Fibers, Materials, 15 (2022).

[115] W. Chen, Y.L. Qin, X.Y. He, Y. Su, J. Wang, Light-weight carbon fiber/silver-coated hollow glass spheres/epoxy composites as highly effective electromagnetic interference shielding material, Journal of Reinforced Plastics and Composites, 41 (2022) 497-508.

[116] J.H. Kim, J.M. Bang, J.H. Kim, ANALYSIS OF LIGHT-WEIGHT STRUCTURE FOR VEHICLE USING METAL AND CARBON FIBER, 10th Asia-Pacific Conference on Engineering Plasticity and its Applications (AEPA)wuha, PEOPLES R CHINA, 2010, pp. 265-269.

[117] T. Hasegawa, T. Miura, T. Takahashi, T. Yakou, STRENGTHENING MECHANISMS IN ALUMINUM CERAMIC PARTICLE COMPOSITE ALLOYS PRODUCED BY MECHANICAL ALLOYING, Isij International, 32 (1992) 902-908.

[118] D. Weiss, Developments in Aluminum-Scandium-Ceramic and Aluminum-Scandium-Cerium Alloys, Light Metals Symposium at the 148th TMS Annual MeetingSan Antonio, TX, 2019, pp. 1439-1443.

[119] H.P. Konka, M.A. Wahab, K. Lian, Asme, SANDWICH STRUCTURES WITH SMART COMPOSITE FACE SKIN, ASME International Mechanical Engineering Congress and Exposition (IMECE)Denver, CO, 2011, pp. 157-166.

[120] R. Kipscholl, R. Stocek, Degradation of Tires During Intended Usage, in: G. Heinrich, R. Kipscholl, R. Stocek (Eds.) Degradation of Elastomers in Practice,

Experiments and Modeling2023, pp. 185-207.

[121] L.Q. Ren, Progress in the bionic study on anti-adhesion and resistance reduction of terrain machines, Science in China Series E-Technological Sciences, 52 (2009) 273-284.

[122] J.E. Steele, How do we get there?, Bionics Symposium 1960, Living Prototypes. The Key To New Technology, 1961, pp. 487-490.

[123] J. Li, F. Du, X.L. Liu, Z.H. Jiang, L.Q. Ren, Superhydrophobicity of Bionic Alumina Surfaces Fabricated by Hard Anodizing, Journal of Bionic Engineering, 8 (2011) 369-374.

[124] L.Q. Ren, Y.H. Liang, Preliminary studies on the basic factors of bionics, Science China-Technological Sciences, 57 (2014) 520-530.

[125] Q. Zhao, Y.H. Liang, L. Ren, Z.L. Yu, Z.H. Zhang, L.Q. Ren, Bionic intelligent hydrogel actuators with multimodal deformation and locomotion, Nano Energy, 51 (2018) 621-631.

[126] X.J.J.o.c. Jia, i. science, Unsmooth cuticles of soil animals and theoretical analysis of their hydrophobicity and anti-soil-adhesion mechanism, 295 (2006) 490-494.

[127] Z. Wang, D.N. Shi, X.W. Wang, Y.B. Chen, Z. Yuan, Y. Li, Z.X. Ge, W.G. Yang, A Multifunctional Light-Driven Swimming Soft Robot for Various Application Scenarios, International Journal of Molecular Sciences, 23 (2022).

[128] H. Zhou, H.Y. Shan, X. Tong, Z.H. Zhang, L.Q. Ren, The adhesion of bionic non-smooth characteristics on sample surfaces against parts, Materials Science and

Engineering a-Structural Materials Properties Microstructure and Processing, 417 (2006) 190-196.

[129] L.Z. Cao, Y. Zhang, N.N. Zhao, X.X. Chen, Optimization Design of Mathematical Modeling for Leakage Noise Reduction of Bionic Fan Blade, 5th International Conference on Machinery, Materials and Computing Technology (ICMMCT)Beijing, PEOPLES R CHINA, 2017, pp. 1034-1037.

[130] Y.Q. Gu, D.S. Dai, J.G. Mou, S.H. Zheng, D.H. Wu, W. Evan, Overview of the Technology of Bionic Surface Drag Reduction, Journal of Biomimetics Biomaterials and Biomedical Engineering, 23 (2015) 59-66.

[131] J.Y. Wang, Q. Cong, Experimental study of the concave bionic drag reduction needles, 4th International Conference of Bionic Engineering (ICBE 2013)Nanjing, PEOPLES R CHINA, 2013, pp. 702-706.

[132] Q.D. Li, H. Lu, D.Y. Li, Effect of recovery treatment on the wear resistance of surface hammered AZ31 Mg alloy, Wear, 426 (2019) 981-988.

[133] L.M. Tian, X.M. Tian, Y.C. Wang, G.L. Hu, L.Q. Ren, Anti-wear properties of the molluscan shell Scapharca subcrenata: Influence of surface morphology, structure and organic material on the elementary wear process, Materials Science & Engineering C-Materials for Biological Applications, 42 (2014) 7-14.

[134] C. Wang, H. Zhou, P.Y. Lin, N. Sun, Q. Guo, P. Zhang, J. Yu, Y. Liu, M. Wang, L.J.M. Ren, Design, The thermal fatigue resistance of vermicular cast iron coupling with H13 steel units by cast-in process, 31 (2010) 3442-3448.

[135] H.Q. Lin, Y.G. Zhao, Z.M. Gao, L.G. Han, Effects of pulse current stimulation

on the thermal fatigue crack propagation behavior of CHWD steel, Materials Science and Engineering a-Structural Materials Properties Microstructure and Processing, 478 (2008) 93-100.

[136] H.Q. Lin, Y. Zhao, Y.G. Zhao, L.G. Han, J. Ma, Q.C. Jiang, Numerical simulation of temperature and thermal stress fields in cast-hot-working-die steel under high density electropulsing, Isij International, 48 (2008) 971-975.

[137] D.L. Cong, Z.S. Li, Q.B. He, D.J. Chen, H.B. Chen, J.Z. Yang, P. Zhang, H. Zhou, Effect of unit size on thermal fatigue behavior of hot work steel repaired by a biomimetic laser remelting process, Optics and Laser Technology, 98 (2018) 205-213.

[138] L. Ribeiro, A. Barbosa, F. Viana, A.M. Baptista, C. Dias, C.A. Ribeiro, Abrasion wear behaviour of alloyed and chilled cast irons, Wear, 270 (2011) 535-540.

[139] V. Sergio, S. Ishikawa, K. Yamamoto, H. Miyahara, K. Ogi, K. Kamimiyada, Control of graphite formation in solidification of white cast iron, International Journal of Cast Metals Research, 21 (2008) 27-30.

[140] Z.K. Chen, T. Zhou, R.Y. Zhao, H.F. Zhang, S.C. Lu, W.S. Yang, H. Zhou, Improved fatigue wear resistance of gray cast iron by localized laser carburizing, Materials Science and Engineering a-Structural Materials Properties Microstructure and Processing, 644 (2015) 1-9.

[141] Y.H. Yuan, P. Zhang, G.P. Zhao, Y. Gao, L.X. Tao, H. Chen, J.L. Zhang, H. Zhou, Effects of Laser Energies on Wear and Tensile Properties of Biomimetic 7075 Aluminum Alloy, Journal of Materials Engineering and Performance, 27 (2018) 1361-1368.

[142] H.F. Zhang, P. Zhang, Q. Sui, K. Zhao, H. Zhou, L.Q. Ren, Influence of Multiple Bionic Unit Coupling on Sliding Wear of Laser-Processed Gray Cast Iron, Journal of Materials Engineering and Performance, 26 (2017) 1614-1625.

[143] H.F. Zhang, T. Zhou, H. Zhou, Z.K. Chen, W.S. Yang, L.Q. Ren, Effects of different bionic units coupling on the sliding wear of gray cast iron, Surface & Coatings Technology, 309 (2017) 96-105.

[144] N. Sun, H.Y. Shan, H. Zhou, D.R. Chen, X.Y. Li, W. Xia, L.Q. Ren, Friction and wear behaviors of compacted graphite iron with different biomimetic units fabricated by laser cladding, Applied Surface Science, 258 (2012) 7699-7706.

[145] N. Sun, H.Y. Shan, H. Zhou, D.R. Chen, L.Q. Ren, Adhesion resistance surfaces against clay resulting from biomimetic adaptation, Surface & Coatings Technology, 206 (2012) 3559-3565.

[146] Z.B. Pang, H. Zhou, P. Zhang, D.L. Cong, C. Meng, C.W. Wang, L.Q. Ren, Study on quantitative relation between characteristics of striature bionic coupling unit and wear resistance of gray cast iron, Applied Surface Science, 331 (2015) 179-184.

[147] Z.B. Pang, H. Zhou, G.F. Xie, D.L. Cong, C. Meng, L.Q. Ren, Effect of bionic coupling units' forms on wear resistance of gray cast iron under dry linear reciprocating sliding condition, Optics and Laser Technology, 70 (2015) 89-93.

[148] Z.K. Chen, S.C. Lu, X.B. Song, H.F. Zhang, W.S. Yang, H. Zhou, Effects of bionic units on the fatigue wear of gray cast iron surface with different shapes and distributions, Optics and Laser Technology, 66 (2015) 166-174.

[149] W.S. Yang, H. Zhou, L. Sun, C.W. Wang, Z.K. Chen, Effect of biomimetic

coupling units' morphologies on rolling contact fatigue wear resistance of steel from machine tool rolling tracks, Optics and Laser Technology, 57 (2014) 175-180.

[150] C. Meng, H. Zhou, D.L. Cong, C.W. Wang, P. Zhang, Z.H. Zhang, L.Q. Ren, Effect of biomimetic non-smooth unit morphology on thermal fatigue behavior of H13 hot-work tool steel, Optics and Laser Technology, 44 (2012) 850-859.

[151] H. Zhou, P. Zhang, N. Sun, C.T. Wang, P.Y. Lin, L.Q. Ren, Wear properties of compact graphite cast iron with bionic units processed by deep laser cladding WC, Applied Surface Science, 256 (2010) 6413-6419.

[152] Z.J. Jing, H. Zhou, P. Zhang, C.W. Wang, C. Meng, D.L. Cong, Effect of thermal fatigue on the wear resistance of graphite cast iron with bionic units processed by laser cladding WC, Applied Surface Science, 271 (2013) 329-336.

[153] Q. Sui, H. Zhou, H. Bao, P. Zhang, Y.H. Yuan, C. Meng, Wear behavior of quenched iron with various shapes and unit processed through two-step laser alloying of C powder, Optics and Laser Technology, 104 (2018) 103-111.

[154] X. Tong, H. Zhou, L.Q. Ren, Z.H. Zhang, R.D. Cui, W. Zhang, Thermal fatigue characteristics of gray cast iron with non-smooth surface treated by laser alloying of Cr powder, Surface & Coatings Technology, 202 (2008) 2527-2534.

[155] W. Su, T. Zhou, P. Zhang, H. Zhou, H. Li, Effect of distribution of striated laser hardening tracks on dry sliding wear resistance of biomimetic surface, Optics and Laser Technology, 98 (2018) 281-290.

[156] W. Su, T. Zhou, Q. Sui, P. Zhang, H. Zhou, H. Li, Z.H. Zhang, Study on the relationship between intervals among laser stripes and the abrasion resistance of

biomimetic laser textured surfaces, Optics and Laser Technology, 104 (2018) 216-224.

[157] J.S. Cruz, SIMILARITY BETWEEN ACTION AND PASSION IN THE FOUNDATIONS OF COGNITIVE SCIENCE, Psicothema, 6 (1994) 95-104.

[158] F. Song, Y.L. Bai, Nanostructure of nacre and its mechanical effects, International Journal of Nonlinear Sciences and Numerical Simulation, 3 (2002) 257-260.

[159] Z. Bouhlel, B. Genard, N. Ibrahim, E. Carrington, J.M.F. Babarro, A. Lok, A.A.V. Flores, C. Pellerin, R. Tremblay, I. Marcotte, Interspecies comparison of the mechanical properties and biochemical composition of byssal threads, Journal of Experimental Biology, 220 (2017) 984-994.

[160] S.W. Wise, MICROARCHITECTURE AND DEPOSITION OF GASTROPOD NACRE, Science, 167 (1970) 1486-&.

[161] A.P. Jackson, J.F.V. Vincent, D. Briggs, R.A. Crick, S.F. Davies, M.J. Hearn, R.M. Turner, APPLICATION OF SURFACE ANALYTICAL TECHNIQUES TO THE STUDY OF FRACTURE SURFACES OF MOTHER-OF-PEARL, Journal of Materials Science Letters, 5 (1986) 975-978.

[162] X. Tong, H. Zhou, M. Liu, M.-j. Dai, Effects of striated laser tracks on thermal fatigue resistance of cast iron samples with biomimetic non-smooth surface, Materials & Design, 32 (2011) 796-802.

[163] S. Kamat, X. Su, R. Ballarini, A.H. Heuer, Structural basis for the fracture toughness of the shell of the conch Strombus gigas, Nature, 405 (2000) 1036-1040.

[164] Z. Zhang, J. Zhu, Y.J. Chu, Z.N.A. Chen, S. Guo, J.Q. Xu, Correlation between Microstructure and Failure Mechanism of Hyriopsis cumingii Shell Structure, Journal of Bionic Engineering, 16 (2019) 869-881.

[165] F.D. Liu, X.N. Xu, J.M. Liu, H.Q. Fan, G.Z. Huang, H. Zhang, The influence of laser etching biomimicking configuration on the strength of metal-plastic connection, Materials Research Express, 9 (2022).

[166] Q.X. Lu, M. Li, A.L. Tian, S.H. Fu, Green Plant Leaf-inspired Smart Camouflage Fabrics for Visible Light and Near-infrared Stealth, Journal of Bionic Engineering, 19 (2022) 788-798.

[167] S.J. Wang, L.Q. Ren, Y. Liu, Z.W. Han, Y. Yang, Mechanical Characteristics of Typical Plant Leaves, Journal of Bionic Engineering, 7 (2010) 294-300.

[168] Z.H. Zhang, L.Q. Ren, H. Zhou, Z.W. Han, X. Tong, Y. Zhao, L. Chen, Effect of Thermal Fatigue Loading on Tensile Behavior of H13 Die Steel with Biomimetic Surface, Journal of Bionic Engineering, 7 (2010) 390-396.

[169] D.L. Cong, H. Zhou, Z.N. Ren, H.F. Zhang, L.Q. Ren, C. Meng, C.W. Wang, Thermal fatigue resistance of hot work die steel repaired by partial laser surface remelting and alloying process, Optics and Lasers in Engineering, 54 (2014) 55-61.

[170] D.L. Cong, H. Zhou, M.Q. Yang, Z.H. Zhang, P. Zhang, C. Meng, C.W. Wang, The mechanical properties of H13 die steel repaired by a biomimetic laser technique, Optics and Laser Technology, 53 (2013) 1-8.

[171] K.L. Johnson, K. Kendall, a.J.P.o.t.r.s.o.L.A.m. Roberts, p. sciences, Surface energy and the contact of elastic solids, 324 (1971) 301-313.

[172] E. Kannatey-Asibu Jr, Principles of laser materials processing, John Wiley & Sons2009.

[173] A. Roy, I. Manna, Laser surface engineering to improve wear resistance of austempered ductile iron, Materials Science and Engineering a-Structural Materials Properties Microstructure and Processing, 297 (2001) 85-93.

[174] Q.L. Zhang, J. Lin, Z.J. Chen, Z.H. Tang, H. Huang, Y.A. Gao, J.H. Yao, Phase Transformation Process of Electromagnetic Induction Assisted Laser Quenching Based on MSC. Marc Software, Chinese Journal of Lasers-Zhongguo Jiguang, 48 (2021).

[175] Z.Y. Chen, G.J. Zhou, Z.H. Chen, Microstructure and hardness investigation of 17-4PH stainless steel by laser quenching, Materials Science and Engineering a-Structural Materials Properties Microstructure and Processing, 534 (2012) 536-541.

[176] Z. Wang, C.W. Wang, M. Wang, Q.Z. Zhao, Manipulation of tribological properties of stainless steel by picosecond laser texturing and quenching, Tribology International, 99 (2016) 14-22.

[177] X.L. Wu, Y.S. Hong, Surface amorphous and crystalline microstructure by alloying zirconium using Nd : YAG pulsed laser, Metallurgical and Materials Transactions a-Physical Metallurgy and Materials Science, 31 (2000) 3123-3127.

[178] H.C. Man, S. Zhang, F.T. Cheng, Improving the wear resistance of AA 6061 by laser surface alloying with NiTi, Materials Letters, 61 (2007) 4058-4061.

[179] A. Almeida, F. Carvalho, P. Carvalho, R.J.S. Vilar, C. Technology, Laser developed Al–Mo surface alloys: Microstructure, mechanical and wear behaviour, 200

(2006) 4782-4790.

[180] X. Han, C. Li, X.X. Chen, S.L. Jia, Numerical simulation and experimental study on the composite process of submerged arc cladding and laser cladding, Surface & Coatings Technology, 439 (2022).

[181] K.K. Zheng, Y.X. Lin, J.G. Cai, C.Q. Lei, Corrosion Resistance and Tribological Properties of Laser Cladding Layer of H13 Die Steel Strengthened by Ultrasonic Rolling, Chinese Journal of Mechanical Engineering, 35 (2022).

[182] J.H. Qian, X.K. Li, G.M. Qiu, T. Qiu, H.T. Zhao, H.H. Yu, Development on laser cladding ceramic coating, Journal of Rare Earths, 24 (2006) 172-178.

[183] S. Rodriguez-Lopez, R. Comesana, J. del Val, A. Duran, V.M. Justo, F.C. Serbena, M.J. Pascual, Laser cladding of glass-ceramic sealants for SOFC, Journal of the European Ceramic Society, 35 (2015) 4475-4484.

[184] D. Triantafyllidis, L. Li, F.H. Stott, Laser cladding of high performance ceramic sheets on a low quality ceramic substrate, Thin Solid Films, 453 (2004) 80-83.

[185] A. Hussain, I. Ahmad, A. Hamdani, A. Nussair, S.J.A.s.s. Shahdin, Laser surface alloying of Ni-plated steel with CO2 laser, 253 (2007) 4947-4950.

[186] Q.C. Guo, H. Zhou, C.T. Wang, W. Zhang, P.Y. Lin, N. Sun, L.Q. Ren, Effect of medium on friction and wear properties of compacted graphite cast iron processed by biomimetic coupling laser remelting process, Applied Surface Science, 255 (2009) 6266-6273.

[187] S. Nowotny, S. Scharek, E. Beyer, K.H. Richter, Laser beam build-up welding: Precision in repair, surface cladding, and direct 3D metal deposition, Journal of

Thermal Spray Technology, 16 (2007) 344-348.

[188] X.H. Wang, M. Zhang, B.S. Du, Fabrication of Multiple Ceramic Particle Reinforced Iron Matrix Coating by Laser Cladding, Materials and Manufacturing Processes, 28 (2013) 509-513.

[189] H.G. Kim, W.R. Kim, O. Kwon, G.B. Bang, M.J. Ham, H.K. Park, K.H. Jung, K.M. Kim, C.W. Lee, G.H. Kim, Laser beam melting process based on complete-melting energy density for commercially pure titanium, Journal of Manufacturing Processes, 45 (2019) 455-459.

[190] J. Onoro, R. Bermejo, A. Portoles, R. Gamboa, Modelling the energy absorbed during a laser beam metal melting process, Revista De Metalurgia, 34 (1998) 421-427.

[191] Y.Q. Yang, J. Chen, C.H. Song, D. Wang, Y.C. Bai, Current Status and Progress on Technology of Selective Laser Melting of Metal Parts, Laser & Optoelectronics Progress, 55 (2018).

[192] O. Rehme, C. Emmelmann, Rapid manufacturing of lattice structures with Selective Laser Melting, Conference on Laser-Based MicropackagingSan Jose, CA, 2006.

[193] F.D. Wang, Mechanical property study on rapid additive layer manufacture Hastelloy (R) X alloy by selective laser melting technology, International Journal of Advanced Manufacturing Technology, 58 (2012) 545-551.

[194] L.L. Sartinska, S. Barchikovski, N. Wagenda, B.M. Rud, Timofeeva, II, Laser induced modification of surface structures, Applied Surface Science, 253 (2007)

4295-4299.

[195] Y. Arshad, R. Linggamm, M.M. Quazi, M.H. Aiman, M. Ishak, A.Q. Zaifuddin, A. Qaban, Laser Surface Modification of Duplex Stainless Steel 2205 to Modify the Surface Roughness, International Journal of Automotive and Mechanical Engineering, 18 (2021) 8695-8703.

[196] Q.H. Wang, H.X. Wang, Laser surface functionalization to achieve extreme surface wetting conditions and resultant surface functionalities, Journal of Central South University, 29 (2022) 3217-3247.

[197] A.Q. Zaifuddin, F. Zulhilmi, M.H. Aiman, M.M. Quazi, M. Ishak, Enhancement of laser heating process by laser surface modification on Titanium alloy, Journal of Mechanical Engineering and Sciences, 15 (2021) 8310-8318.

[198] G.P. Zhao, Y.H. Yuan, P. Zhang, T. Zhou, H.W. Wang, X.F. Li, H. Zhou, Effect of hardness gradient of laser bionic coupling unit on wear resistance of 6082 aluminum alloy, Optics and Laser Technology, 153 (2022).

[199] N. Anand, K.C. Chang, P.C. Huang, A.C. Yeh, C.W. Tsai, C.C. Lee, M.T. Lee, Y.B. Chen, An effective and efficient model for temperature and molding appearance analyses for selective laser melting process, Journal of Materials Processing Technology, 294 (2021).

[200] B. Sagbas, G. Gencelli, A. Sever, Effect of Process Parameters on Tribological Properties of Ti6Al4V Surfaces Manufactured by Selective Laser Melting, Journal of Materials Engineering and Performance, 30 (2021) 4966-4973.

[201] E.M. Sefene, State-of-the-art of selective laser melting process: A

comprehensive review, Journal of Manufacturing Systems, 63 (2022) 250-274.

[202] S.Q. Qin, Z. Peng, X.L. Shi, Y.W. Xue, K.P. Zhang, Q.P. Huang, Optimization of Textured Parameters to Improve the Tribological Behavior of TC4-Based Bionic Coating Using RSM, Tribology Transactions, 65 (2022) 441-456.

[203] G.J. Xiao, Z.Y. Liu, O.C. Lin, Y. He, S. Liu, J.C. Huang, A Novel Approach for the Fabrication of Sharkskin Structured Bionic Surfaces with Hydrophobic Wettability: Laser Processing and Ordered Abrasive Belt Grinding, Journal of Bionic Engineering.

[204] Y.Q. Xing, C. Luo, Y.Z. Wan, P. Huang, Z. Wu, K.D. Zhang, Formation of bionic surface textures composed by micro-channels using nanosecond laser on Si3N4-based ceramics, Ceramics International, 47 (2021) 12768-12779.

[205] B.Z. Yin, J.E. Liu, B.C. Liu, P. Bo, W. Peng, T. Yun, Y.F. Zheng, C.M. Wang, X.L. Ma, H.T. Pei, Process Optimization on Laser Powder Bed Fusion of WE43 Magnesium Alloy, Chinese Journal of Lasers-Zhongguo Jiguang, 49 (2022).

[206] T.W. Tsai, Y.M. Lee, Analysis of microscale heat transfer and ultrafast thermoelasticity in a multi-layered metal film with nonlinear thermal boundary resistance, International Journal of Heat and Mass Transfer, 62 (2013) 87-98.

[207] W.B. Yuan, N.T. Yu, L.Y. Li, Y. Fang, Heat transfer analysis in multi-layered materials with interfacial thermal resistance, Composite Structures, 293 (2022).

[208] E.J.B. Thompson, RA Fisher's contributions to genetical statistics, (1990) 905-914.

[209] X.B. Liu, G. Yu, J. Guo, Q.Y. Shang, Z.G. Zhang, Y.J. Gu, Analysis of laser surface hardened layers of automobile engine cylinder liner, Journal of Iron and Steel

Research International, 14 (2007) 42-46.

[210] Z.H. Zhang, P.Y. Lin, H. Zhou, L.Q. Ren, Microstructure, hardness, and thermal fatigue behavior of H21 steel processed by laser surface remelting, Applied Surface Science, 276 (2013) 62-67.

[211] H. Zhou, P. Zhang, Z. Zhang, W. Qiu, Y. Liu, L. Ren, Thermal Cycling Effect on the Wear Resistance of Bionic Laser Processed Gray Iron, Journal of Bionic Engineering, 11 (2014) 288-295.

[212] A. Shojaei, M. Arjmand, A.J.J.o.m.s. Saffar, Studies on the friction and wear characteristics of rubber-based friction materials containing carbon and cellulose fibers, 46 (2011) 1890-1901.

[213] N. López Perrusquia, M. Doñu, V. Cortez, D. Sánchez, F.J.M.O.P.L. Vázquez, Characterization of the Fracture of an Automobile Drum Brake, 1372 (2011) 145-150.

[214] J. Schijve, FATIGUE OF AIRCRAFT MATERIALS AND STRUCTURES, International Journal of Fatigue, 16 (1994) 21-32.

[215] H. Zhou, Q.C. Guo, P.Y. Lin, Z. Wei, X.L. Zhang, L.Q. Ren, Influence of H13 steel unit on wear behavior of vermicular cast iron, Applied Surface Science, 255 (2008) 3394-3399.

[216] L.S. Zhong, Y.H. Xu, M. Hojamberdiev, J.B. Wang, J. Wang, In situ fabrication of titanium carbide particulates-reinforced iron matrix composites, Materials & Design, 32 (2011) 3790-3795.

[217] M. Riebisch, K. Böllert, D. Streitferdt, I. Philippow, Extending feature diagrams with UML multiplicities, 6th World Conference on Integrated Design & Process

Technology (IDPT2002), 2002, pp. 1-7.

[218] A. Kazakov, D. Kiselev, E. Kazakova, G.F. Vander Voort, L. Chigintsev, Quantitative Description of Microstructural Banding in Steels, Materials Performance and Characterization, 6 (2017) 224-236.

[219] X.L. Zhou, R. Zhou, P.X. Zhang, Y.H. Jiang, Z. Li, H. Zhao, Magnetic field induced pearlite transformation in Fe-0.47C-2.31Si-3.15Mn steel above the eutectoid temperature, Materials Science and Engineering a-Structural Materials Properties Microstructure and Processing, 525 (2009) 42-47.

[220] E. Vuorinen, R.N. Kumar, M. Linz, A. Kankanala, F. Back, Standing contact fatigue analyse of steels with different microstructures, 7th International Conference on Materials Structure and Micromechanics of Fracture (MSMF 7)Brno, CZECH REPUBLIC, 2013, pp. 622-+.

[221] C. Meng, L.F. Wang, K. Xu, J.N. Hao, H.B. Zhou, X.L. Shu, S. Jin, L.Y. Liang, G.H. Lu, C.S. Becquart, Object Kinetic Monte Carlo simulation of hydrogen clustering behaviour with vacancies in tungsten, Journal of Nuclear Materials, 526 (2019).

[222] S. Ghodrat, A.C. Riemslag, M. Janssen, J. Sietsma, L.A.I. Kestens, Measurement and characterization of Thermo-Mechanical Fatigue in Compacted Graphite Iron, International Journal of Fatigue, 48 (2013) 319-329.

[223] T. Andriollo, Y. Zhang, S. Faester, V. Kouznetsova, Analysis of the correlation between micro-mechanical fields and fatigue crack propagation path in nodular cast iron, Acta Materialia, 188 (2020) 302-314.

[224] I.M. Dmytrakh, R.L. Leshchak, A.M. Syrotyuk, Influence of sodium nitrite concentration in aqueous corrosion solution on fatigue crack growth in carbon pipeline steel, International Journal of Fatigue, 128 (2019).

[225] G.P. Zhao, Y.H. Yuan, P. Zhang, T. Zhou, H. Zhou, Influence of orientations biomimetic units processed by laser on wear resistance of 6082 aluminium alloy, Optics and Laser Technology, 127 (2020).

[226] F.N. Alayunt, B. Cakmak, H.Z. Can, Friction and rolling resistance coefficients of fig, 1st International Symposium on FigIzmir, Turkey, 1997, pp. 301-304.

[227] P. Fino, T.E. Lockhart, Required coefficient of friction during turning at self-selected slow, normal, and fast walking speeds, Journal of Biomechanics, 47 (2014) 1395-1400.

[228] Q. Song, H. Zhou, Y. Li, L. Wang, H. Shan, Z. Zhang, L.J.T.-B.-. Ren, Friction and wear properties of cast-iron material with bionic non-smooth surface under normal temperature, 26 (2006) 27.